UNIVERSITÀ DEGLI STUDI DI TRIESTE

XXXVI CICLO DEL DOTTORATO DI RICERCA IN

NANOTECNOLOGIE

Borsa MUR/Ateneo confinanziata dal Dipartimento di Fisica su fondi CERIC-ERIC Progetto INTEGRA

IMAGING AND CHARACTERIZATION OF FIBROTIC TISSUES

Settore scientifico-disciplinare: **FIS/07**

DOTTORANDO
Lorenzo-D'Amico

COORDINATORE
PROF. Alberto-Morgante

SUPERVISORE DI TESI
Dr. Giuliana-Tromba

CO-SUPERVISORE DI TESI
Dr. Christian-Dullin

ANNO ACCADEMICO 2022/2023

UNIVERSITÀ DEGLI STUDI DI TRIESTE

XXXVI CICLO DEL DOTTORATO DI RICERCA IN

NANOTECNOLOGIE

Borsa MUR/Ateneo confinanziata dal Dipartimento di Fisica su fondi CERIC-ERIC Progetto INTEGRA

IMAGING AND CHARACTERIZATION OF FIBROTIC TISSUES

Settore scientifico-disciplinare: **FIS/07**

DOTTORANDO
Lorenzo-D'Amico

COORDINATORE
PROF. Alberto-Morgante

SUPERVISORE DI TESI
Dr. Giuliana-Tromba

CO-SUPERVISORE DI TESI
Dr. Christian-Dullin

ANNO ACCADEMICO 2022/2023

"Be the change you wish to see in the world"

-Mahatma Gandhi-

Imaging and characterization of fibrotic tissues

Lorenzo D'Amico
PHD0600102

Università Degli Studi di Trieste
Dipartimento di Fisica
Trieste, Italy
Elettra Sincrotrone
s.s. 14 km 163,500 in Area Science Park
Basovizza(TS),Italy

Abstract: Fibrosis is a general term to describe diseases that lead to an increase of connective tissue. This may lead to tissue remodelling, formation of permanent scar tissue and changes in the mechanical properties of the organ involved. Fibrosis is a result of deregulated wound healing process, which can be caused by injuries or various diseases, as well as chronic or inflammatory processes. Fibrosis can occur in various organs such as kidneys, heart, liver and lungs. The here presented work is focused on lung fibrosis. One specific form of lung fibrosis is the so-called Idiopathic Pulmonary Fibrosis (IPF). The median survival of IPF patients is 25 years and outcomes of IPF patients are often even poorer than those of patients with many types of cancer. The lungs contain complex connective tissue structures whose function is to keep the airways open and elastic, thus enabling oxygen uptake and gas exchange. Several different fibre types such as elastin, fibrin and collagen are present within said connective tissue, and aid the aforementioned processes. However, they exhibit different responses, for instance while elastin degrades during inflammation, collagen deposition increases. This complex interplay of pathomechanisms acting on the composition and structure of the connective tissue within the lungs and the correlation to a specific disease has not yet been studied in detail. Therefore, the aim of the thesis is to establish a multi-modal analysis pipeline to provide a comprehensive analysis of lung fibrosis.

To this end I utilized phase contrast micro-computed tomography to obtain structural information of the lung, histology to map the regions of collagen deposition, Fourier Transformed Infrared Spectroscopy to obtain the chemical fingerprint of a tissue, and atomic force microscopy to perform mechanical characterization of a tissue. The novelty of this approach does not lie in the application of specific single techniques, but in their spatial correlation to study the same tissue area.

To validate the consistency and benefits of the pipeline, I performed studies on two different mouse models for lung fibrosis - one chemically induced, one using genetically modified mice. Based on the differences in the involved pathomechanism in those two models, differences in the composition of the lung fibrosis can also be assumed. Thus, these models were used to show-case the performance of the developed pipeline.

I found that both models showed strong features of lung fibrosis. However, the typically applied histological scoring cannot distinguish between them. By applying the here presented analysis pipeline, I found significant differences between the fibrotic regions of the two models. Thus, I argue that this novel method presents a vital tool for the analysis of tissue specimens of various origin.

Acknowledgments

In writing this thesis, I want to thank all the people who have been a part of my PhD journey. It has been quite a ride, and I could not have done it without the support and help of many. First and foremost, I owe a big thanks to my mentors, Dr. Giuliana Tromba and Dr. Christian Dullin. They have been my guides and teachers, and I am grateful for all the knowledge they have shared with me. I also want to shout out my colleagues at the SYRMEP beamline, like Dr. Elena Longo, Giulia Saccomano, Dr. Marko Kudrna Prašek, Dr. Nicola Sodini, and Diego Dreossi. Their work and support have made this journey a lot more enjoyable and insightful. During my PhD, I got to work with some amazing people from other Elettra beamlines, like Dr. Giovanni Birarda, Dr. Lisa Vaccari, and Professor Heinz Amenitsch. They shared their knowledge about InfraRed Spectroscopy and Small-Angle X-ray Scattering, and it expanded my horizons. Special thanks to Professor Frauke Alves for giving me the chance to spend six months at the Max Planck Institute for Multidisciplinary Sciences in Göettingen. It was an eye-opening experience. I cannot forget to mention Professor Sarah Köster and Ruth Meyer for their help with AFM measurements at the Institute for X-Ray Physics, University of Göttingen. Their expertise was a game-changer. Shoutout to my PhD buddies, too, like Martina Zangari, Carolina Paba, Federica Zingaro, Beatrice Senigagliesi, and Angelika Svetlove. They were always there when I needed support. I would like to extend my heartfelt thanks to Pia Prašek for her invaluable assistance in the correction and proofreading of my thesis. Big thanks to my friends outside of academia, too, like Tommaso Carbone, Niccoló Udina, Alessia Boliandi, and Stefano Boliandi. Your friendship meant the world to me during this journey. And last but certainly not least, a heartfelt thanks to my family my dad, my mum, and my grandparents for always having my back. Your love and support kept me going. These three years have been transformative, both personally and academically. I'm grateful to all of you for being a part of this amazing journey. Lastly, I would like to express my sincere gratitude to CERIC-ERIC (INTEGRA project) for funding my PhD scholarship. Your support has been instrumental in making this journey possible. Thank you.

Nomenclature

Abbreviations

AFM	Atomic Force Microscopy
CN_{ble}	Healthy controls for the bleomycin induced pulmonary fibrosis
CN_{gen}	Controls for the Nedd4-2 KO model of pulmonary fibrosis
CT	Computed Tomography
micro-CT	Micro Computed Tomography
ECM	Extra Cellular Matrix
FFPE	Formalin fixed and paraffin embedded
FTIR	Fourier Transform Infrared Spectroscopy
IPF	Idiopathic Pulmonary Fibrosis
IR	InfraRed
PBI	Propagation-Based Imaging
PF	Pulmonary fibrosis
PF_{ble}	Bleomycin induced pulmonary fibrosis
$PF_{ble+Nin}$	Bleomycin induced pulmonary fibrosis treated with Nintedanib
PF_{gen}	Nedd4-2 KO model of pulmonary fibrosis
ROI	Region Of Interest
ROS	Reactive Oxygen Species
SAXS	Small Angle X-Rays Scattering
SEM	Scanning Electron Microscopy
SPM	Scanning Probe Microscopy
SR-SAXS	Synchrotron Radiation Small Angle X-Rays Scattering
2D	2-dimensional
3D	3-dimensional

Contents

List of Figures

List of Tables

Chapter 1

Introduction

1.1 Lung Diseases

Lung disease is a general term to describe a pathological condition in the lung that impairs its function. It can affect the airways as well as other structures of the lungs and can be therefore divided in three main categories:

- Airway diseases
- Lung Tissue diseases
- Lung Circulation diseases

The first category affects the airways in charge of gas transport, the second concerns morphological changes of the lung tissue, and the third involves narrowing and scarring of the blood vessels. Respiratory diseases are among the leading causes of mortality worldwide [1]. The main risk factors include air pollution, occupational chemicals and dusts. In 2017 Soriano et al. [2] reported that 544.9 million individuals worldwide had a chronic respiratory disease. This is an increment of $\simeq$ 39.8 % compared to the number of individuals affected in 1990. Figure 1.1 shows the growth of chronical respiratory diseases on the worldwide scale from 1990 to 2017. Furthermore, after the COVID-19 pandemic, the number of cases of lung diseases is expected to increase. Indeed, the damages caused by COVID-19 lead to lesions that might develop into lung fibrosis in the future [3]. *Lung fibrosis* is one of the most common pulmonary disease. Fibrosis describes a deregulated wound healing process which replace the parenchymal tissue with connective tissue. In case of lungs, the air sacs, known as alveoli, become damaged, thickened, and scarred, resulting in changes of the mechanical properties of the organ (i.e. compliance), that over time can cause the organ failure. Lung fibrosis can present several symptoms such as dry cough, fatigue, and shortness of breath. There are several reasons for the development of lung fibrosis, such as environmental pollution [4], as well as connective tissue diseases [5]. As reported above, also infectious lung diseases, such as COVID-19 pneumonia, can cause fibrosis [6]. One additional type of fibrosis is the so-called Idiopathic Pulmonary Fibrosis (IPF), which is a very severe condition with bad prognosis for the survival of the patient. As reported by Nathan et al. [7], after the diagnosis, patients can survive between two and five years. Unfortunately, IPF

is typically diagnosed only at late stages and the causes of the development of IPF are widely unknown.

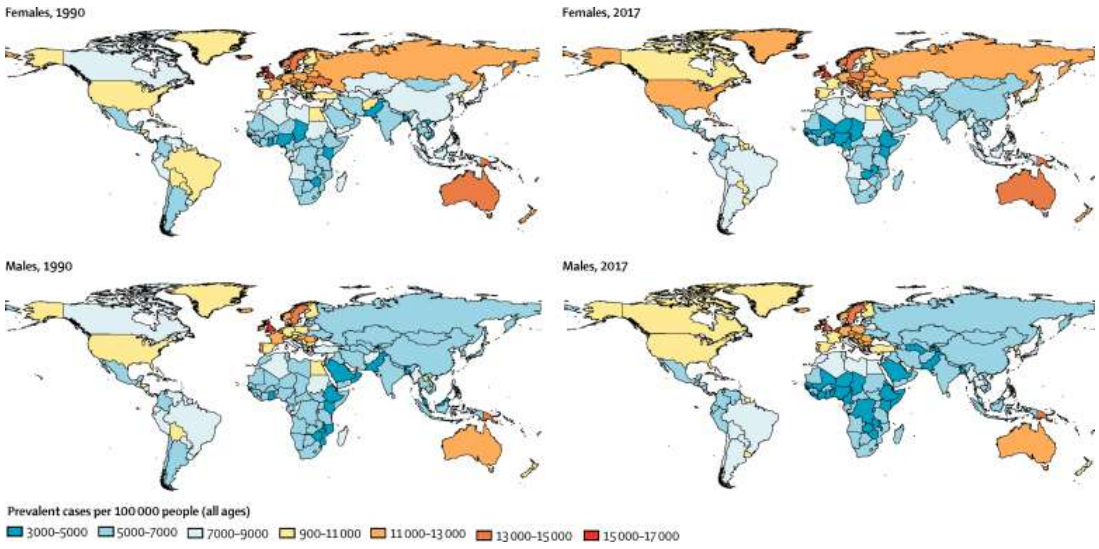

Figure 1.1: Worldwide chronic respiratory diseases prevalence by country in 1990 and 2017. Reported from Soriano et al. [2].

Indeed, early diagnosis is difficult because initial symptoms, most commonly dyspnea and cough, are mild, non-specific, and overlap with many other common conditions. Therefore, the presence of symptoms is insufficient, but for a full diagnosis medical imaging and lung functional test must be performed. Fibrosis is considered to be a permanent condition, since so far there are no treatment options to cure it. There are only few therapeutic approaches, such as Nintedanib [8] and Pirfenidone [9]. As reported by Pitre et al. [10] both treatments reduce mortality, but Nintindanib improved lung function more than Pirfenidone. Nevertheless, both medicines help to slow down the IPF progression, but neither of them is a definitive cure. The development of novel treatments is hindered by the lack of knowledge of the underlying mechanisms.

1.2 Lung Anatomy

Lungs are the primary organs of the respiratory system. Humans and mammals have a pair of lungs. They are located one on each side of the thoracic cavity. The function of these organs is to extract oxygen from the air and pass it into the bloodstream, and to remove the carbon dioxide from the bloodstream and release it in the atmosphere. The pair of lungs have different sizes. The right one is subdivided into three lobes: the superior, the middle and the inferior, whereas the left one is smaller, due to the presence of the heart, and are divided into two lobes: the superior and inferior (Figure 1.3).

Both of them are covered with a protective covering called the pleural tissue, which is thin, moist, and smooth and serves to reduce the friction between the chest wall and the lung tissue during the breathing motion. The respiratory system can be subdivided into an upper tract and a lower one. Lungs belong to the latter. This begins with the trachea, which then branches into the left and right bronchus, which supplies the left and right lung, respectively.Following these two bronchi into the lungs, they split in smaller and smaller tubes until they branch in the

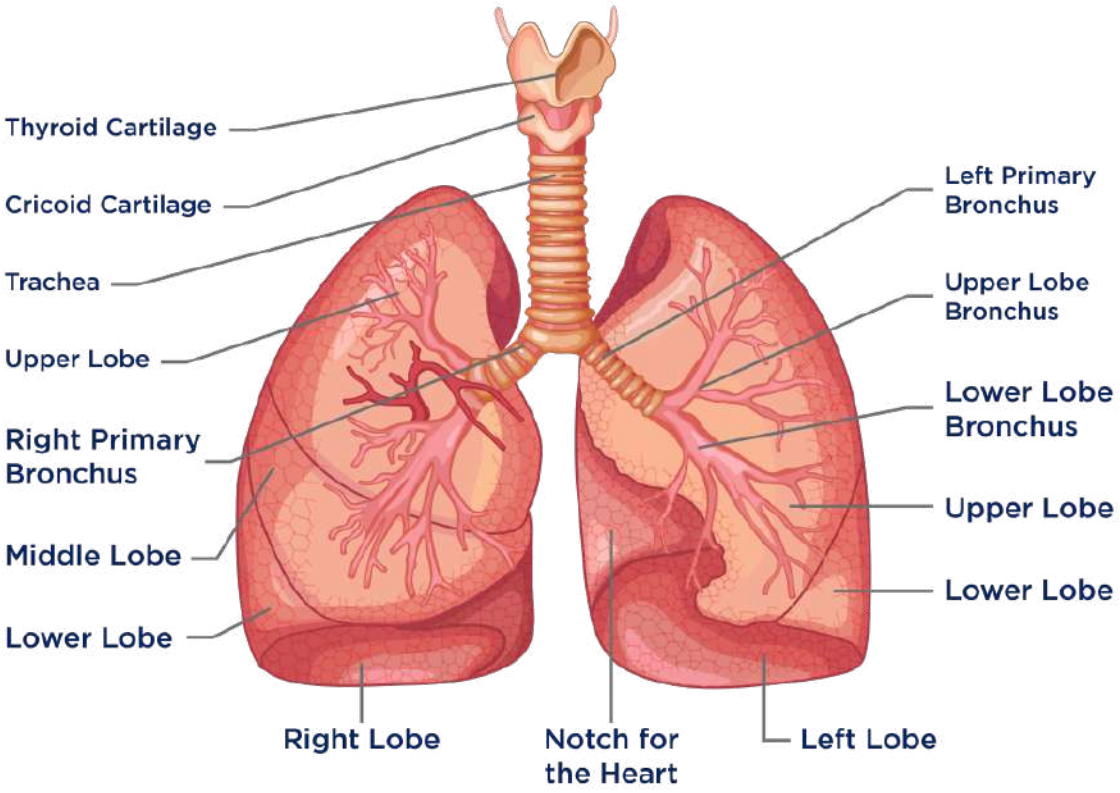

Figure 1.2: Anatomical representation of human lungs. Reported from [11]

bronchioles. These are the smaller ramification of the bronchial airways. They are comprised of the terminal bronchioles and the respiratory bronchioles. These mark the beginning of the respiratory zone, where small sacks called alveoli are present. Here, the gas exchange takes place. Particularly, there is an exchange of oxygen for the carbon dioxide. Oxygen diffuses in the bloodstream through the capillaries surrounding the pulmonary alveolus, whereas the carbon dioxide is released from the capillaries into the alveoli to be expelled during the breath out.

There are two phases during breathing: inspiration and expiration. The first allows influx of air into the lungs. Here the intercostal muscles and the diaphragm contract whereas in the second phase inspiration muscles relax letting gases leave the lungs. This alternation of contraction and relaxation happens between 12 and 18 times per minute in a healthy adult. The lung has certain properties which allow it to working in this manner: elasticity to expand and contract during the breathing process and a certanin degree of stiffness to keep its shape and the alveoli open. These peculiar biomechanical properties are provided by the lung complex connective tissue comprised by several different fibres such as elastin, fibrin, and collagen.

1.3 Therapy

Until 2014, the immunosuppressant therapy was the standard practice for treating lung fibrosis. It was based on the combination of Prednisone, Aza- thioprine and N-acetylcysteine. Unfortunately, as reported by Raghu et al. [12] this form of treatment increased the likelihood of hospitalization. Nowadays, two antifibrotic therapies have been approved for the treatment of IPF: Pirfenidone and Nintedanib. The former decreases the production of collagen and slows the fibrotic process by suppressing the cytokine TGF-β [13]. Nintedanib, on the other hand, decreases the fibroblast activity, which is responsible for the synthesis of ECM components [14]. Nowadays, both of these drugs are good choices as primary treatment for lung fibrosis [15]. However, there are no significant changes in the overall progression of the disease and the high mortality within 3 to 5 years after the diagnosis [16].

1.4 Animal Model

The precise factors that initiate the fibrotic process are still unknown. Thus, further research is required. Animal models have been used to gain better understanding of human biology and health. They are exploited to study complex biological mechanisms, diseases, and medical treatments. The usage of animal models for pre-clinical studies has several advantages over studying patients, such as an easier control of the environment, an easier way of delivering pharmacological agents, and the potential to study genetic alterations. In this work, two different mouse models of pulmunoray fibrosis (PF) were used. In one, fibrosis was induced by means of the injection of bleomycin through the trachea. This is one of the most common rodent models used for pulmonary fibrosis [17]. The second model is a transgenic one, and fibrosis is not chemically induced but develops more naturally [18]. Bleomycin is an antibiotic used to cure cancer. In the lungs, it induces the generation of reactive oxygen species (ROS) by forming a complex with Fe^{3+}. During this chemical process, oxidants are created, and they can cause inflammatory reactions within the lungs. The alveolar macrophages release cytokinesis, starting the fibrotic process [19]. In the transgenic model, the conditional deletion of Nedd4-2, an ubiquitin ligase, in lung epithelial cells produces chronic lung disease sharing the key features with lung fibrosis. However, there are some limitations in the usage of animal models: the organs are usually smaller, rendering, for instance, the imaging more challenging and, in some cases, the architecture of the organs is different from human ones. In the specific case of lungs, they have multiple lobes, in both humans and mice, but they vary in number and organization between the two species. The mice lungs have 1 lobe on the right side and 4 on the left one, whereas in human the lungs have 2 lobes on the left and 3 on the right. Furthermore, since the breathing rate of a mouse is higher than for humans, the ratio between the diameter of the bronchi and the size of the lung is higher than in humans; another difference between the two species is that in humans the segmental bronchi exhibits an irregular pattern of dichotomous (repeated bifurcations) whereas in mice there is a single central airway that runs the whole length of each lobe with multiple later branches. However, despite the known limitations (e.g. the differences in the architecture of the organs), mouse models have been helpful in finding new treatments and cures for many human diseases [20], [21].

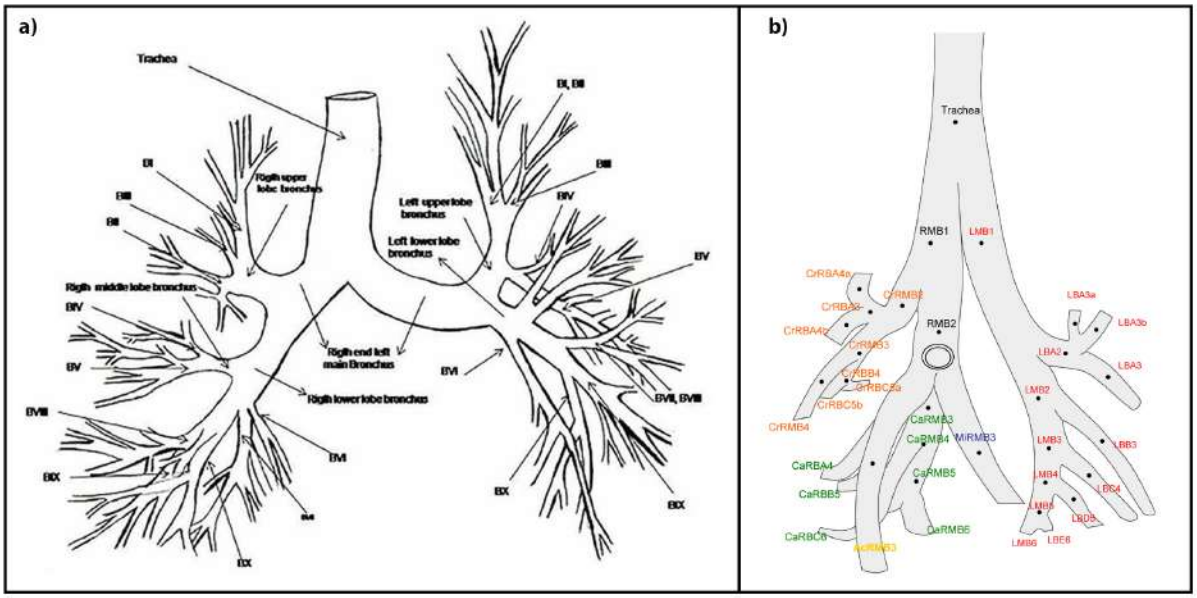

Figure 1.3: Examples of lungs architectures. a) Segmental bronchi in human lungs, exhibiting an irregular pattern of dichotomous (repeated bifurcations), adapted from Monteiro et. all [22]. b) Segmental bronchi in mouse lung, showing a single central airway with multiple lateral bifurcation, adapted from Thiesse et. all [23].

1.5 Aims of the thesis

The widely unknown causes of lung fibrosis, especially IPF, do not allow early diagnosis and the development of treatments to cure it. The key feature of this disease is: the inhomogeneity of deposition of extracellular matrix (ECM) components, mainly collagen. Unfortunately, little is known about the fibre types, their orientation and the pathomechanisms involved. The gold standards for the diagnosis of lung fibrosis are histology and high-resolution computed tomography (CT). Histology consists in the analysis of thin tissue section subsequently coloured using specific staining protocols and the acquisition of images with standard light microscopy. This is a widely used method in both clinical routine and biomedical research. The tissue is extracted, performing a surgical lung biopsy. Usually, it is the latter step of the diagnosis process. Previously, medical imaging and lung functional test were performed to confirm the presence of the lung fibrosis and then perform the invasive operation of biopsy. Unfortunately, very often, the diagnosis is made when the disease is already at the late stages and thus its progression can be only slowed down but not cured. Since little is known about the pathomechanisms occurring during fibrosis, the aim of this work is to better characterize fibrotic tissues, in particular lung tissue, to shed some light on this disease.
The here presented PhD thesis aims to answer the following questions:

- "Does the combination of different techniques allow for the identification of fibrosis in general ?"
- "Is this multi-techniques pipeline capable of clustering fibrosis into subtypes ?"
- "Is it possible to reduce the number of techniques exploited and still obtain good outcomes ?"

Chapter 2

Analysis platform

The aim of this PhD thesis was the development of a multi-techniques pipeline, where modern imaging and analysis methods are coupled together to characterize fibrotic tissue, especially in PF. PF causes an inhomogeneous deposition of connective tissue, such as collagen, fibrin, elastin, which replaces the parenchymal tissue, impairing the respiratory function. Therefore, techniques had been selected to address the following aspects:

- Structural changes in the lung tissue
- Type and concentration of the deposited fibres
- Changes in the mechanical properties of the tissue

The first technique used in the pipeline was single distance phase contrast micro-CT. This is a *non-destructive* imaging method that allows seeing inside a solid object. Using this technique allows obtaining morphological information of the tissue, e.g. evaluation of structural changes in the tissue induced by fibrosis, as well as the position, inside the lung, of the fibrotic regions. Despite the high resolution (pixel size of $\simeq 2$ µm), fibres, such as collagen, cannot be detected as they show no different contrast from other tissue type. Therefore, a logical approach is to combine this technique with classical histology. The latter is, indeed, the second step of the pipeline. The position of the fibrotic regions of interest (ROIs) were calculated using the 3D reconstructed volume acquired with phase contrast micro-CT, and used to cut histological slices, with a thickness of $\simeq 5$ µm, at these targeted positions, using a microtome. The histological slices were then stained with picrosirius red [24] and imaged using a standard light microscope. This histological staining is a very powerful method because it allows detecting the regions of collagen deposition, and when the standard light microscope is coupled with a polarization filter, it allows distinguishing between two types of collagen, collagen I (yellow) and collagen III (green). Histological slices were used both to score the degree of fibrosis and to provide a reference map for the subsequent techniques of the pipeline. The third technique used was Fourier Transform Infrared Spectroscopy (FTIR). The spectra obtained with this vibrational spectroscopy contain information on the molecular structure and conformation, allowing probing the molecular composition of the tissue. In the presented work, FTIR spectroscopy was exploited to map the collagen I and III content inside both the fibrotic and healthy FFPE lungs. Subsequently, on the same slice of tissue, a biomechanical characterization was performed using

Atomic force microscopy (AFM). The last technique exploited in the pipeline was small angle X-Ray scattering (SAXS) which allows obtaining information about differences in structures at the nanoscale.

2.1 Sample Preparation

All imaging and analysis techniques presented in this thesis were performed on tissue specimens - mouse lungs - prepared in the same way. Directly after dissection, the lungs were filled with formalin to generate a nearly physiological shape and then put in formalin overnight. Formalin leads to cross-linking of proteins and thus changes the consistency of the specimens into rubber-like and prevents the tissue from degradation. Following this step, the tissue is chemically dehydrated using a series of ascending ethanol concentrations. Finally, the dehydrated tissue is washed in Xylol and embedded in paraffin and can then be stored at room temperature nearly indefinitely. This preparation, which is also called FFPE (formalin fixed and paraffin embedded) is the most commonly applied preparation scheme for soft-tissue specimens. Hence, an imaging pipeline that can work with FFPE tissue specimens will automatically be generally applicable for a large variety of studies as well as preserved human tissue.
To my knowledge, such a pipeline has not been realized for a subsequent application of all the imaging and analysis techniques used in this study. The main reason is that FFPE is not an ideal starting point for e.g. AFM. Thus, establishing this pipeline for FFPE was a challenging endeavour and presents one of the main achievements of this study. Nevertheless, this preparation scheme also generates some shortcomings in the study. The very first step of inflating the lung with formalin defines the shape and the expansion of the lung. Thus, structural analysis will always be limited to the variations in this procedure. In addition, the chemical dehydration generates a strong shrinkage of the tissue, which depends on the tissue type. Therefore, loose tissue like a healthy lung will most likely shrink more than dense consolidated tissue of a fibrotic lung, which in turn will also impact structural analysis. Post-mortem tissue autolysis starts, which will degrade the tissue and also its fibre content. Therefore, formalin fixation needs to take place as soon as possible after death. Since some additional post-mortem analysis like ex-vivo micro-CT were applied for some of the mice, this was not always achievable, which will certainly also impact the results. Moreover, most of the presented imaging techniques require thin tissue sections. The cutting however also introduces deformations. At least for this part, a solution was found that will be presented in the thesis.

2.2 Phase Contrast micro-CT

This section introduces the concept of tomography, which is then extended to its high resolution version (micro-CT), the principle of interaction of X-rays with matter, the concept of propagation based imaging (PBI), and a brief description of synchrotron facilities where this technique can be used.

2.2.1 Tomography

Tomography is an imaging method which derives cross-sections. The word originates from the Greek word *tomos*, which means "slice". A device used to perform tomography is called a tomograph, and a tomographic image represents "a slice", "a section", or "a cutting". This method is used in radiology, biology, archaeology etc. The expression *volume imaging* as well as 3D *imaging* can be used when referring to this kind of imaging method. In general, tomography presents an inverse problem aiming to reconstruct a 3D source distribution out of a set of 2D observations - so essentially to overcome the loss in dimension in the data.
Projection data from multiple directions are gathered and then fed into a tomographic reconstruction algorithm to retrieve the "slices". Tomography is a general term to describe this type of imaging. In more detail, depending on the physical source and phenomena exploited, there are different techniques, such as Computed Tomography (CT), Positron Emission Tomography (PET), etc. In this work only X-ray CT, in particular X-ray micro-CT, is used. X-ray CT uses the principle of reconstructing images from measurements of X-ray transmission through the imaged object. When referring to X-ray micro-CT, the same principle mentioned above is exploited, but on the microscale.

2.2.2 Introduction to X-Ray Computed Tomography

X-rays and visible light are different energies range of the electromagnetic spectrum. The difference between them is the wavelength of the individual photons. X-rays describe the wavelength range between 10 picometres to 10 nanometres, whereas visible light describes the range between 380 and 700 nanometres. The higher energy of X-rays, compared to visible light, allows them to pass through most objects, such as the human body. A very well known example, where this electromagnetic radiation is exploited, is radiography. In this imaging technique, the sample is illuminated with an X-ray beam. A certain amount of X-rays is absorbed by the object, depending on its local electron density and thickness. A digital radiographic image is generated by a detector, which converts the intensity of transmitted X-rays into an electric current (photoelectric effect). However, the efficiency of this effect is low at high photon energies. Therefore, in most micro-CT, a crystal called scintillator is used. This converts X-rays into visible light, which then gets detected. Then the scintillator is imaged by an optical microscope. Nowadays, also direct conversion detectors exist. However, they are limited in spatial resolution.
2D radiography is the basis of micro-CT, where a set of angular distributed planar images is acquired. The amount of these, called projections, depends on the resolution and the beam/object size, but is usually in the range of 1000 images. The following step is called reconstruction, where the combined information of all the projections are exploited to calculate the cross-section of the scanned object. There are several available algorithms to perform reconstructions. The most common one, which was also used in this work, is filtered back projection.
There are several possible set-ups when performing computed tomography. Clinically gantry based systems are used, in which the patient lies still, while the X-ray tube and the detector perform a combined rotation around it. There is also a different approach, used in this work, in which the X-ray beam and the detector are fixed and the sample/object rotates. This configuration is preferred in micro-CT since in most of the cases the object to scan is lighter than the

X-ray source and detector, allowing a more precisely rotation.

2.2.3 Absorption and Propagation-based imaging

Absorption is the source of contrast in conventional micro-CT imaging. This mode is based on mapping the linear attenuation coefficient of X-rays passing through the investigated sample. X-rays are attenuated, depending on the types, densities and thicknesses of the penetrated materials on their path. If different regions i=1,2,...,n , figure 2.1, occur along their path, the transmission through the imaged sample is calculated by the equation 2.1:

$$I = I_0 e^{-\sum_{i=1}^{n} \mu_i d_i} \tag{2.1}$$

Equation 2.1 takes into account the most general case, where an object is made with different materials, with different thicknesses and absorption coefficients. I represents the intensity of the X-rays seen by the detector, I_0 represents the intensity of the X-rays that impinge on the sample, μ_i are the absorption coefficients of different materials, and d_i are the thicknesses of the different materials. Usually, for imaging the inner parts of an object, X-rays in the energy range between 10 and 100 keV, are used, due to their penetrating ability. Unfortunately, in this energetic range, elements with low atomic number (Z), such as most biological tissues, show poor contrast, since the differences in the attenuation are very small. Therefore, absorption based imaging is not well suited for the soft tissues, such as kidneys, liver, lungs etc.

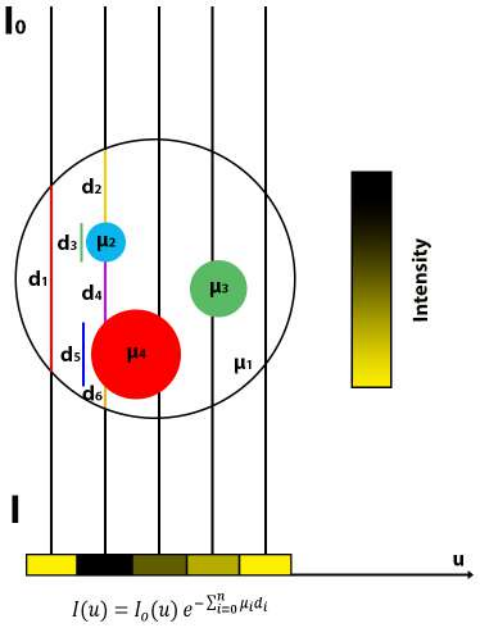

Figure 2.1: Sketch of the attenuation of X-rays impinging on an object. The sample is made by different materials, characterized by different attenuation coefficients (μ). The intensity seen by each pixel of the detector depends on the attenuation coefficients, as well as the thickness of the objects passed by the X-rays. For the colour bar, the darker the colour and the higher the attenuation.

There are several phase-based x-ray imaging techniques, such as analyser-based imaging (ABI), edge illuminations (EI), Propagation-based phase contrast X-ray imaging (PBI). Only

the latter will be described, as it was used for the scope of the present PhD thesis. PBI can be performed when the X-ray beam is coherent and the distance between the sample and the detector is appropriately increased compared to the absorption modality, figure 2.2b. The contrast is generated by interference between parts of the wave, that have suffered different phase retardation. This contrast is superimposed to the conventional absorption contrast. Both the absorption and the phase-shift of X-rays can be described introducing the complex refractive index, equation 2.2:

$$n = 1 - \delta + i\beta \tag{2.2}$$

δ represents the decrement of the real part of the refractive index, which is related to the phase shifts of the electromagnetic wave in matter, whereas β is the imaginary part, which characterizes the absorption properties of the material.

In the diagnostic X-ray energy range, in case of soft tissues, the real part of the refractive index is roughly three order of magnitude larger than the imaginary part, rendering the phase effect more important than the attenuation. This means that in this kind of tissue, the contrast is mostly coming from the phase effects rather than absorption. The values of δ and β change as a function of the energy, equation 2.3.

$$\delta \propto \frac{1}{E^2} \qquad \beta \propto \frac{1}{E^3} \tag{2.3}$$

Equation 2.3 shows that the phase-effects decrease less dramatically with the energy compared to absorption. This is an advantage over the absorption based approach because in phase-contrast modalities good-quality images can be obtained at higher energies (thus low dose[1]). To summarize, PBI allows the imaging of soft tissues, which with the conventional absorption technique would not be possible, and owing to the above-mentioned relationship, it can be done using a low dose radiation.

One of the characteristics that has to be fulfilled, to exploit this imaging technique, is the coherence. There are two types of coherence, the temporal (or longitudinal) and the spatial (or lateral). The former concerns the energy spectrum of the X-ray beam (the narrower the spectral bandwidth and the higher the coherence), whereas the latter regards the source size and the geometry of the system (the smaller the source, and the larger the source-to-sample distance, the higher the coherence). For this purpose, synchrotron facilities are exploited, since they provide X-rays with a high level of spatial coherence and high flux of photons. Despite this, one of the greatest advantages of this imaging modality is the simplicity of the set-up, since it does not require any optical elements between the sample and the detector. The image contrast is, as a first approximation, proportional to the Laplacian of the phase-shift in a plane perpendicular to the optical axis.

Furthermore, there is a crucial dependency of the phase-contrast signal on the effective propagation distance. This relationship is represented in equation 2.4.

Figure 2.2 shows the configurations for attenuation-based imaging (a), where the sample-to-detector is smaller, and the in-line phase-contrast imaging (b), where the sample-to-detector,

[1]The dose is the energy that remains inside the tissue as a result of an exposure to ionizing radiation (e.g. X-rays)

must be sufficient to allow the interference between the wavefront which impinged and did not imping on the sample, respectively.

$$D = \frac{dl}{d+l} \tag{2.4}$$

Where d and l are the sample-to-detector and the source-to-sample distances, respectively. When $l \gg d$, a usual condition fulfilled in synchrotron setup, the effective propagation distance is approximately the sample-to-detector distance ($D \simeq d$).

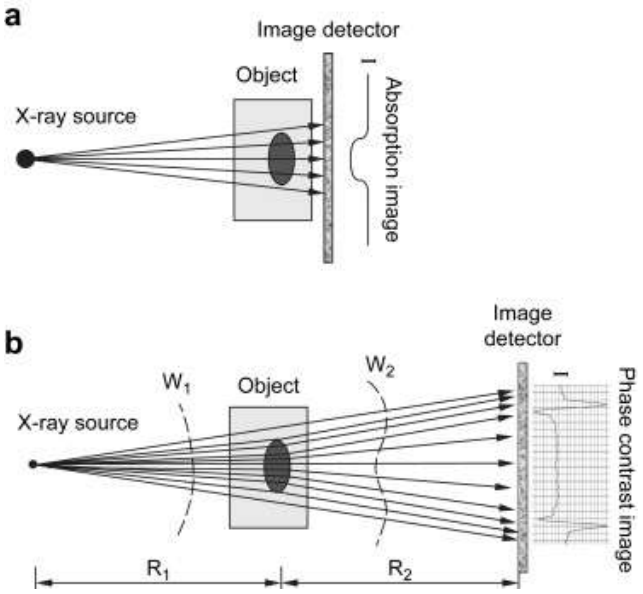

Figure 2.2: Schemes a) attentuation-based imaging configuration and b) in-line phase-contrast imaging configuration. Reported from [25].

2.2.4 Synchrotron facilities

The synchrotron is one type of particle accelerator, where electrons travel around a fixed closed-loop. These facilities are composed of a storage ring with a diameter of hundreds of meters. Inside this ring, an electron beam circulates with an energy of few giga-electron volts (GeV). From a filament, which can be either a metal wire or a large piece of metal, electrons are ejected. Afterwards, a pre-acceleration is performed using disc-loaded wave guides in a linear accelerator (LINAC). Subsequently, the electrons are injected in a first synchrotron accelerator (booster), where their energy increases until they reach the final energy. Synchrotron facilities can be grouped into first, second, third generation machine and fourth generation (DLSR - Diffraction-Limited Storage Ring). In the first two, the booster was made to operate simultaneously as a synchrotron and as a storage ring, whereas in the third and fourth generation, the storage ring is separated from the booster, and the electron energy is kept constant. To accelerate electrons to their final energy, radio frequency cavities are used in the booster. Figure 2.3 shows a schematic representation of a third generation synchrotron architecture. Electrons travel in ultra-high vacuum (less than 10^{-8} mbar) to minimize the probability of collision with residual gas. Figure 2.3 shows that straight sections are present to inject electrons from one accelerator to another (LINAC-to-booster and booster-to-storage ring). The ring is actually a polygon where its sides are linked by bending magnets (BM) deviating the beam towards the next straight line.

As a consequence of this deviation from a straight trajectory, electrons emit electromagnetic radiation, known as synchrotron radiation (SR), which is then carried by transportation lines called beamlines. Each beamline is designed for a specific scientific purpose, which depends on the photon flux, beam dimension, bandwidth etc. Experimental hutches can be located from tens to some hundreds of meters away from the source. In addition to straight sections of synchrotron contains other devices such as wigglers and ondulators, which also generate radiation , but were not used in the presented PhD thesis.

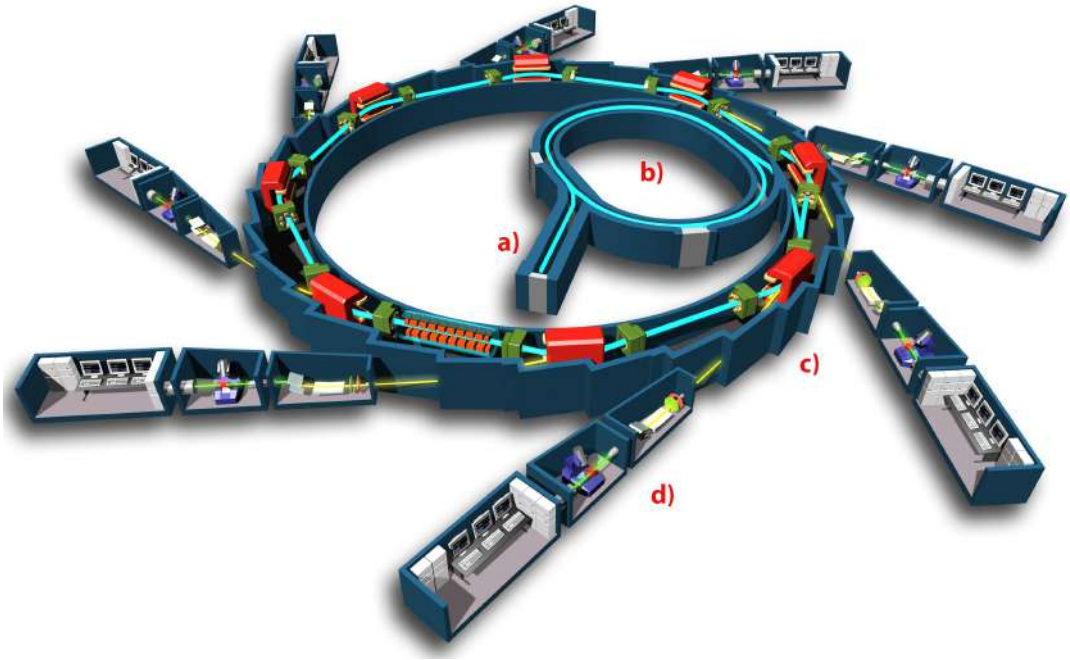

Figure 2.3: Schematic representation of a third generation synchrotron. a) Linear accelerator (LINAC), b) accelerating ring (booster), c) storage ring, d)beamline. Copyright EPSIM 3D/JF Santarelli, Synchrotron Soleil, reproduced with permission.

2.3 Histology

Histology is a branch of biology that studies the anatomy of biological tissue. This technique analyses thin tissue sections subsequently coloured using specific staining protocols. The acquisition of histological images is performed using a standard light microscope. This method is widely used in medical diagnosis as well as in both clinical and biomedical research. There are countless staining protocols that allow targeting different tissue and cell type. However, histology has several disadvantages:

- The tissue has to be embedded in a stiff matrix, such as paraffin, to be cut
- The cutting is performed in an almost blind manner which does not allow targeting certain sites of interest
- The cutting can introduce deformation
- It is a destructive technique

- Information are intrinsically 2D and just for few microns of tissue

2.4 Fourier Transform Infrared spectroscopy (FTIR)

This section provides a brief introduction to the principles of infrared spectroscopy, to the Fourier transform infrared spectroscopy (FTIR), and the application of this technique in the biological field.

2.4.1 Infrared spectroscopy

InfraRed (IR) region is an interval of the electromagnetic spectrum that extends from visible light to microwaves. Conventionally, this spectral region is divided into three intervals (figure 2.4), named accordingly to their distance from visible light:

- near-infrared (NIR): 14000-4000 cm^{-1}
- mid-infrared (MIR):4000-400 cm^{-1}
- far-infrared (FIR): 400-10 cm^{-1}

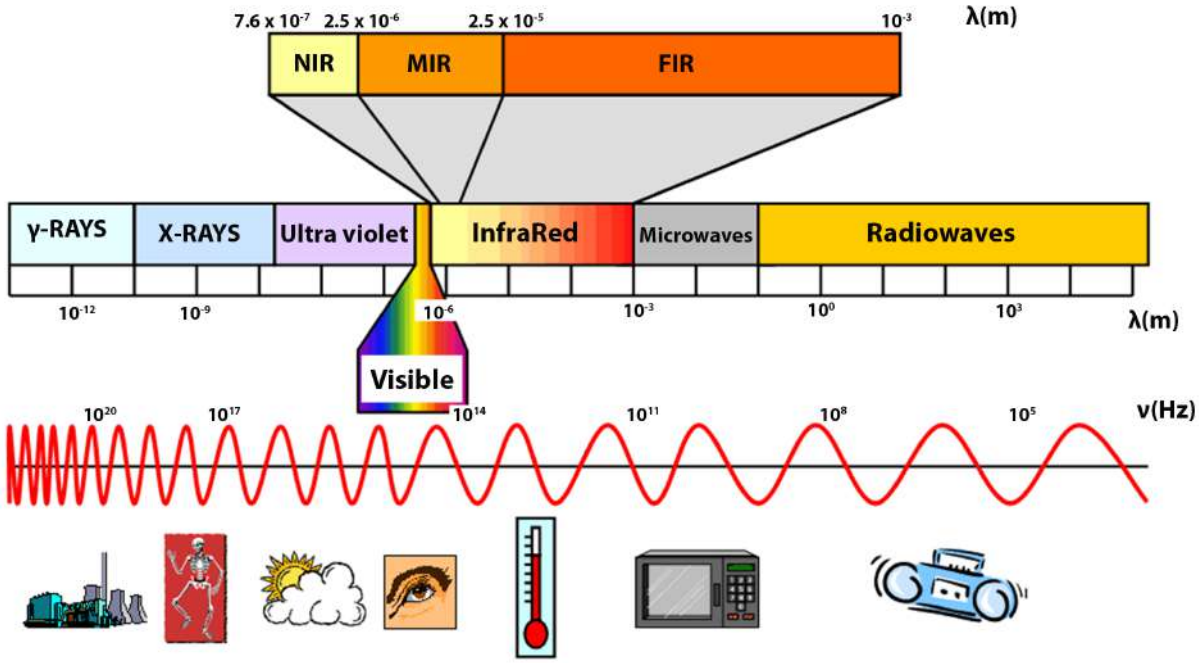

Figure 2.4: Sketch of the electromagnetic spectrum of light. The IR range and its subregions (NIR, MIR, FIR) are highlighted, adapted from [26].

The energies of photons in the IR spectra range from 1.25 meV to 1.7 eV. To induce vibrational motion of covalent bounded atoms and functional groups of molecules requires energy. For organic molecules, which are the leading actors of the biochemistry of life, the transition energies are in the range of $\simeq$ 44 meV to 440 meV. This energy interval falls into the MIR region, which is the only one that will be considered in the here presented PhD thesis.
From the molecular model kits, we are used to thinking that covalent bonds are rigid stick

or rods. The bonds however resemble more stiff springs that can be both bent and stretched. Above 0 K there are several vibration modes for these bonds, such as symmetric and asymmetric stretch, and bending. The absorption of IR radiation, having photons of appropriate energy, may induce transition between energy states. The frequency required to induce this transition depends mainly on three factors:

- Type of vibration
- The bond dissociation energy
- The atoms involved

The frequencies required for the stretching of a given bond are usually higher than those to bend it. To better understand this working principle, we start with the simplest model of a diatomic molecule. Its stretching frequency can be approximated with the Hooke's law. A simple harmonic oscillator, with two masses joined by a spring, is used to represent two atoms bounded together.

$$\nu = \frac{1}{2\pi}\sqrt{\frac{k}{\mu}} \tag{2.5}$$

where ν is the frequency, k is the spring constant, and μ is the reduced mass of the system, that for the particular case of a diatomic molecule can be calculated as follows:

$$\mu = \frac{m_1 m_2}{m_1 + m_2} \tag{2.6}$$

Equation 2.9 shows that the higher the strength of the bond and the higher the frequency, whereas increasing the atom's mass leads to a decrease in frequency.

$$E = \frac{1}{2}kx^2 = h\nu \tag{2.7}$$

Equation 2.7 represents the potential energy (E) of a simple harmonic oscillator, where k is the spring constant and x is the displacement of the spring from its equilibrium position, and h is the Plank's constant. The energy of vibration depends also on how much the spring stretches or compresses. Equation 2.7 assumes that the energy profile is continuous. At the atomic level, the molecular systems are discrete and therefore equation 2.7 cannot be used. As previously mentioned, a diatomic molecule can only have discrete levels of energy that can be described by quantum mechanics.

$$E_n = (n + \frac{1}{2})h\nu \tag{2.8}$$

where ν is the frequency, n is the quantum number (0,1,2,3,...) and h is the Plank's constant. Unfortunately, the simple model here introduced holds only for the transition between the ground state (n=0) and the first vibrational quantum level. Indeed, for a more accurate modelling, the repulsion of the electron clouds at the extremes of the vibration needs to be taken into account, as well as the extension and compression limits of the bond. All the deviations from the simple harmonic oscillator model (figure 2.5a) lead to a more appropriate anharmonic model (figure 2.5b).

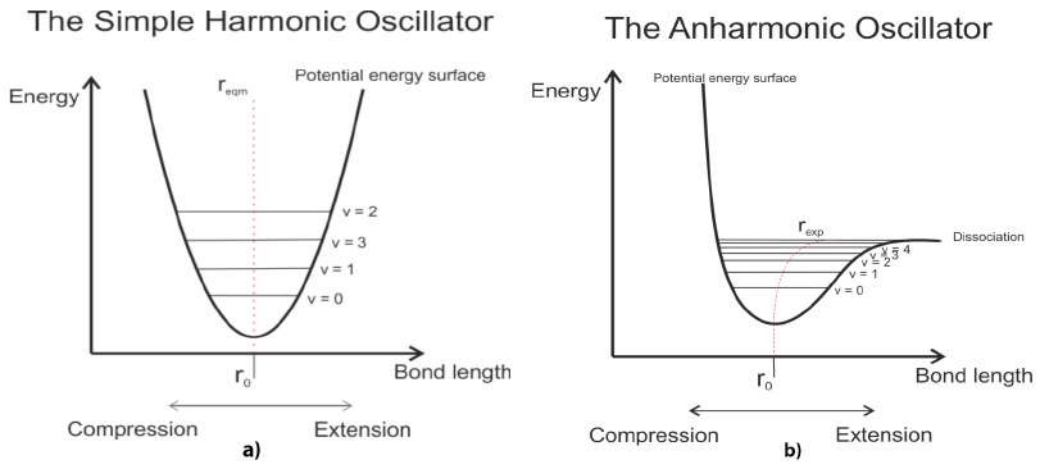

Figure 2.5: Schematic representation of harmonic a) and anharmonic b) models for the potential energy of a diatomic molecule. r_0 is the equilibrium distance that minimize the potential energy U. Adapted from [27].

After the definition of the basis for the vibration of a simple diatomic molecule, it is necessary to extend the model for polyatomic molecules. In the case of a molecule constituted by a number of atoms N, higher than two, it is intuitive to imagine that there are a wide number of vibrations. All of them can be described as the motion along a threefold set of coordinate axis. A single atom in a molecule has 3 degrees of freedom, corresponding to the motion along the three Cartesian axes (x, y, and z). Therefore, for a polyatomic molecule made up of N atoms, there are 3N degrees of freedom. 3 degrees of freedom are used to describe the motion and other 3 are used to describe the whole molecule rotation. Therefore, the 3N-6 degrees remaining are the fundamental vibration for nonlinear molecules. Among these fundamental vibrations, also known as normal modes of vibration, only those that produce a net change in the dipole moment[2] of the molecule are IR active. It has to be noted that the amount of IR absorption bands is generally different from the total number of active fundamental vibrations. Indeed, it might be that a single frequency can induce more than one vibration mode. When IR light illuminates a sample, absorption occurs if the frequency of the IR photon matches the one of the vibrational mode. Therefore, there is a direct correlation between the frequency of absorbed IR radiation and the types of bond in the sample under investigation. The superimposition of all the bands creates a unique IR spectrum for each compound, and information about the molecular architecture of the sample is retrieved.

2.4.2 Fourier Transform InfraRed (FTIR) spectroscopy

Nowadays, modern instrumentation to perform IR experiments is based on an interferometric system. The most widely used tool in interferometry is the Michelson interferometer, figure 2.6a. This is used to split a single incoming beam of coherent light source into two identical beams. Each of them travels a different path, and then they are recombined before reaching the detector. The differences in the distance travelled generate phase differences, between the two

[2]The dipole moment measures the separation of positive and negative electrical charges within a system, that is, a measure of the system's overall polarity.

beams, which is then identified by the detector. These phase differences provide information about anything that changes the phase along the path (either physical changes in the path length or changes in the refractive index through which the beam travels). The Fourier Transform InfraRed (FTIR) exploits an interferometer to perform the spectral splitting.

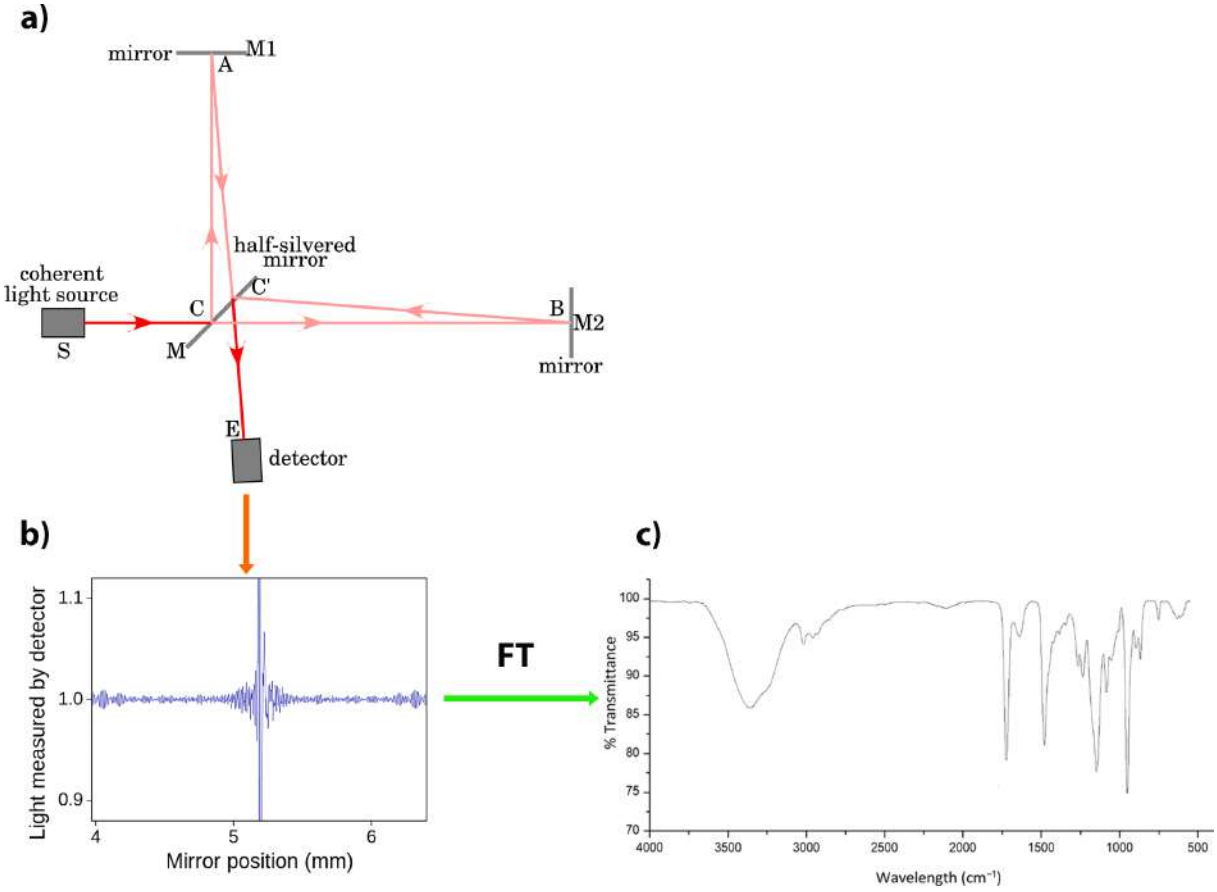

Figure 2.6: Scheme of the FTIR spectroscopy. a) Scheme of the Michelson interferometer, adapted from [28]. b) Interferogram generated by the constructive/destructive interference condition created over time, adapted from [29]. c) IR spectrum obtained by applying the Fourier transformation on the interferogram, adapted from [30].

Whether a sample is placed between the beam splitter and the detector, the interferogram of the sample is collected, figure 2.6b. The transmission spectrum of the sample (% T), figure 2.6c, can be retrieved by computing the ratio between its spectrum and the spectrum of the background or reference.

2.4.3 FTIR spectromicroscopy

FTIR interferometers can be coupled to special microscopes capable of focusing both IR and visible light into the same spot. In this case, it is possible to obtain chemical information on the inspected sample at the micrometric scale. Visible/IR microscopes use mainly reflective optics (gold or aluminium coated mirrors) and objectives, in order to have a minimal loss due to absorption from the materials constituting the optics, allow the higher possible bandwidth and reduce the chromatic aberration of the objectives. These type of objectives are called Schwarzschild or Pastegrain and are composed of two mirrors, one focusing and one collecting

the light. This geometry is quite common, and it is not only used for IR optics, but also in telescopes (i.e. James Webb telescope). In order to obtain chemical information at the microscale, two approaches can be employed: FTIR mapping (figure 2.7a) and imaging (figure 2.7b). FTIR mapping is carried out by tightly focusing the IR light of a very bright source (ideally Synchrotron source or laser sources) to a spot size limited by the diffraction of the light (for Mid-IR 310 µm) and then raster scan the sample point by point. Using Synchrotron Radiation (SR) as the source, only few tenths of seconds are necessary to obtain a spectrum with high signal-to-noise ratio[3] over the whole detector sensitivity range, but mapping large areas (mm^2) can be time-consuming. For this type of experiments, FTIR imaging is a better approach. This acquisition modality exploits large sources, like the conventional benchtop ones, and array detectors, that allow for a parallel collection of thousands of pixels in one shot, usually 64x64 or 128x128 pixels over areas from 170 to 350 $micron^2$.

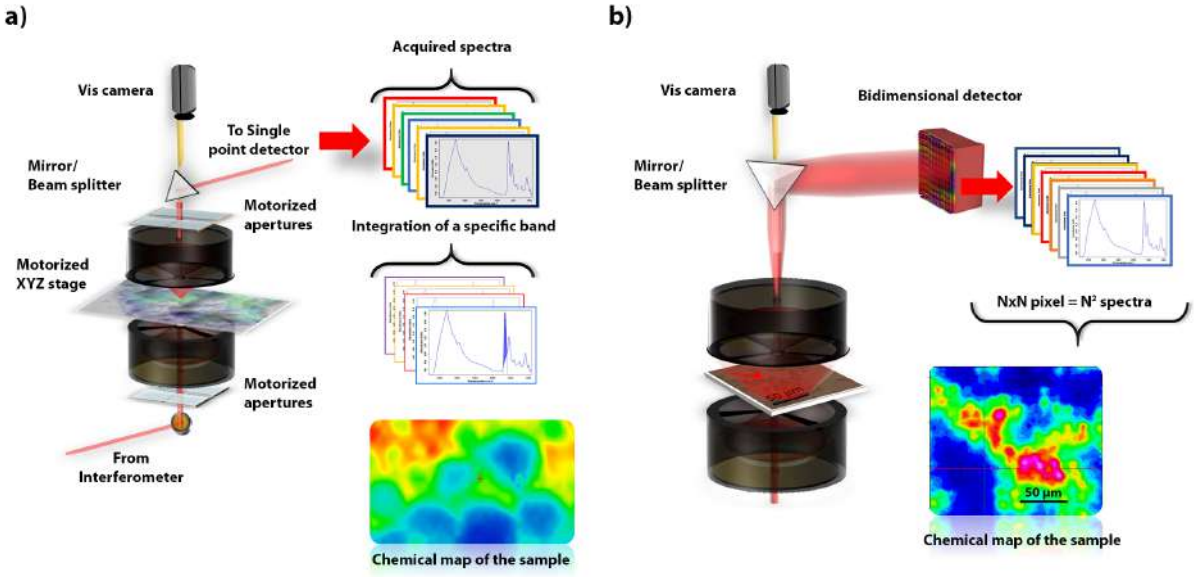

Figure 2.7: Schematic representation of the two modalities exploited to gain chemical information by means of IR spectromicroscopy. a) IR mapping procedure: at first, a visible image is acquired and divided into a matrix of points. Subsequently, the motorized apertures of the microscope are closed to get the desired pixel resolution. Then the sample is rastered-scanned to collect an infrared spectrum for each point. By means of the integration of a specific absorption band of the acquired spectra, an image displaying the chemical distribution of the molecules can be obtained. b) IR imaging. The bi-dimensional detector can be seen as a matrix of points (usually either 64x64 or 128x128 pixels). Therefore, at once N^2, with NxN the number of detector pixels, spectra can be obtained. The chemical image can be obtained as explained for the IR mapping.

2.4.4 FTIR spectroscopy of proteins

In the last decades, the application of IR light for spectromicroscopy and imaging has increased, especially in the study of biological tissues. Indeed, this is a label-free and not destructive approach that requires a small amount of material as well as a minimum sample preparation.

[3]Signal-to-noise ratio can be defined as the ratio between the desired information or the power of a signal and the undesired signal or the power of the background noise.

Furthermore, since the spectra obtained with vibrational spectroscopy, such as FTIR, are sensitive to the molecular structure and conformation, this allows probing the molecular composition and structure of biological tissue [31], [32], [33].
Proteins are defined as repetition of amino acid subunits bounded to each-other by the amide bonds. The series of amide groups composes the backbone which folds, giving the polypeptide structure characterizing each protein. The polypeptide chain give rise to characteristic normal modes of proteins, the *amide-bands*. There are nine amide bands, Amide A, Amide B, and Amides I-VII, that are originated by the stretching and bending modes of the following amide groups: C=O, C-N, N-H, and O-C-N [34].

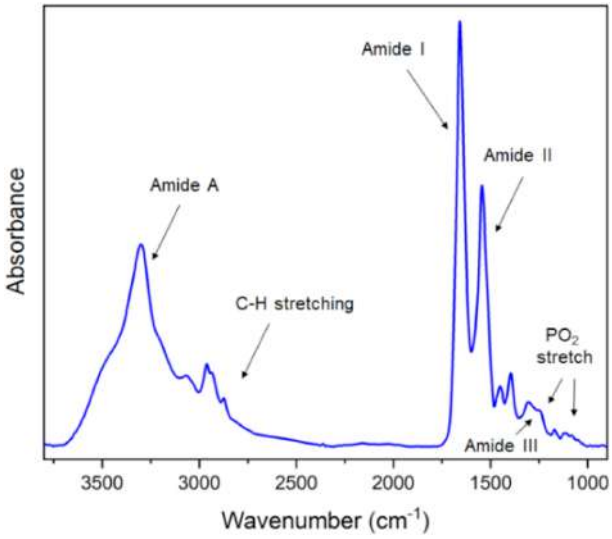

Figure 2.8: Example of absorbance spectrum of Bovine Serum Albumin (BSA).

Figure 2.8 depicts the absorbance spectrum of Bovine Serum Albumin (BSA). This spectrum is used to show the position of the above-mentioned Amide bans. The Amide I (1700-1610 cm^{-1}) vibrations arise from different contributions: $\sim$ 80% from the stretching of C=O, $\sim$ 10% from the out-of-phase CN stretching, and $\sim$ 10% from the in-plane N-H bend. This band is the most intense, among the amide bands sensitive to the protein secondary structure, therefore it is the most commonly used one for secondary structure analysis. The Amide II (1595-1480 cm^{-1}) is generated by the out-of-phase-combination of the N-H in plane bending ($\sim$ 60%) and the C-N stretching ($\sim$ 40%). The Amide II is less sensitive to the protein secondary structure than the Amide I. The Amide III mode (1400-1200 cm^{-1}) is the in-phase combination of the N-H bending and C-N stretching.

2.4.4.1 Collagen

Collagen is a structural protein, and it is part of the ECM components. There are fourteen types of collagen and they form a wide range of structures, e.g. fibrils, sheets, and network. The most notable ones are the *fibrils*, which are a composed of different fibrillar collagens (types I, II, III, IV, and XI), and can be found in most connective tissue. Abnormal formation of collagen deposition is commonly observed in several pathologies such as fibrosis [35]. In the lung, the most abundant types of collagen are I and III, and a difference in their ratio is connected

with respiratory diseases [36]. It has been demonstrated that specific types of collagen can be identified by FTIR spectroscopy in the spectral interval ranging from the Amide I to the Amide III band, by means of the FTIR spectroscopy [37].

2.5 Atomic Force Microscopy (AFM)

Atomic Force Microscopy (AFM) is a type of scanning probe microscopy[4] (SPM). It is a very versatile and powerful tool that allows performing force measurements [38], and topographic imaging [39]. The AFM set-up comprises an optical microscope coupled with a "head" . Inside this last part of the set-up, are housed a piezoelectric transducer, a laser, a mirror, and a photodiode. Furthermore, a cantilever is inserted inside the head, and the sharp AFM probe tip is attached at the end of the cantilever.

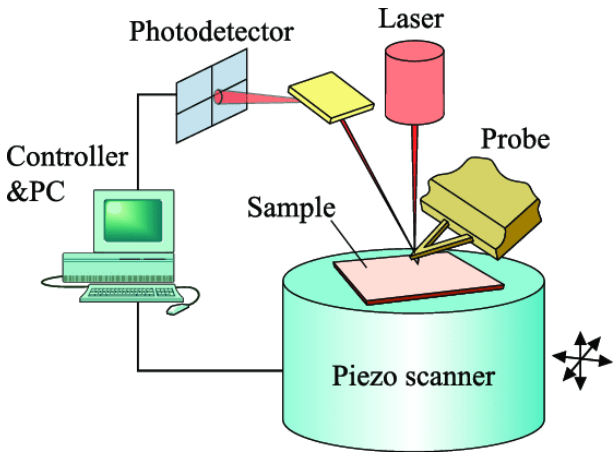

Figure 2.9: Schematic representation of the AFM set up, Adapted from Ishida and Craig [40].

Figure 2.9 shows a schematic representation of the AFM set-up. The laser diode beam is directed on the back of the cantilever in correspondence to the tip, and it is reflected to a four quadrant photodiode (detector). When the tip is closed to the surface, small forces are generated between the probe and the surface, leading to a deflection of the cantilever. The cantilever deflection is then converted into a shift of the laser spot. The signal is transformed into a current, that represents the tip-surface interaction forces. When the probe is far from the surface, the tip-surface interactions are dominated by attracting forces, such as van der Walls and capillary forces, while when the cantilever-surface distance is shorter, by repulsive force, figure 2.10.

[4]Scanning probe microscopy is a branch of microscopy that forms images of a surface using a physical probe to scan the sample

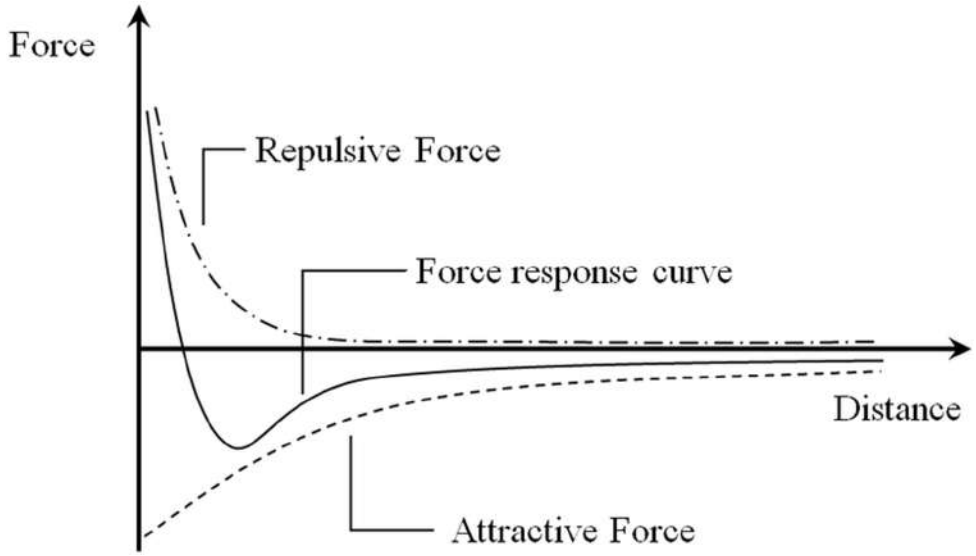

Figure 2.10: Example of a force-displacement plot, in which the contributions of the different forces (attracting and repulsive) are displayed, adapted from [41].

In the presented PhD thesis, the AFM was used to performed force measurements. In the following subsection, the working principles of AFM-based force spectroscopy are presented.

2.5.1 Force Spectroscopy Atomic Force Microscopy

In this measurement mode, the tip does not raster scan the surface under investigation, but moves only along the z direction (vertical direction) towards the sample, and then, after it reaches a certain indentation depth, it moves away from it. During this procedure, the cantilever deflection is recorded as a function of the sample-tip distance. Usually, this is displayed as an 2D plot, where the abscissa represents the probe-surface distance (nm), while the ordinate the changes in the cantilever deflection (V) figure 2.11.

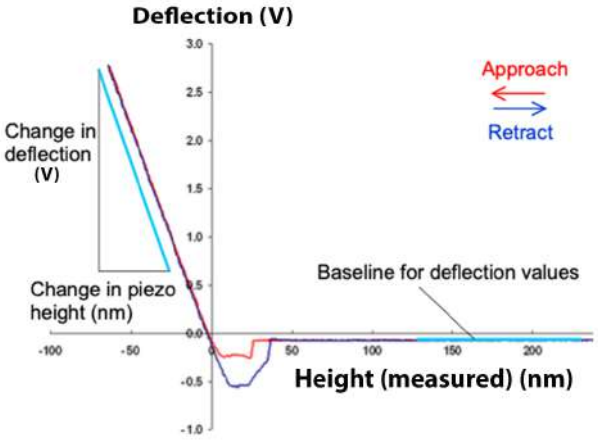

Figure 2.11: Example of a deflection-distance plot. In red, it is represented the approach of the cantilever towards the surface, whereas in blue the retraction, adapted from [42].

The cantilever can be thought of as a spring, and its deflection is proportional to the tip-surface interactions. However, two measurements are required to convert the photodetector

signal into a quantitative value of force (known as SetPoint): the *sensitivity* and the *spring constant*. The sensitivity is measured performing a force curve on a hard substrate. This parameter provides the deflection of the tip in nanometres for a given movement of the detection laser on the photodetector. Once the deflection of the cantilever is known as a distance (Δ), the Hooke's law, equation 2.9, can be used to convert this value into a force (F). However, to exploit equation 2.9, the spring constant k of the cantilever needs to be calculated. All the cantilevers, exploited in the here presented work, were already provided with the spring constant.

$$F = -k\Delta x \tag{2.9}$$

The deflection-distance curve can be converted, exploiting the sensitivity and the spring constant, into the force-curve curve, figure 2.12.

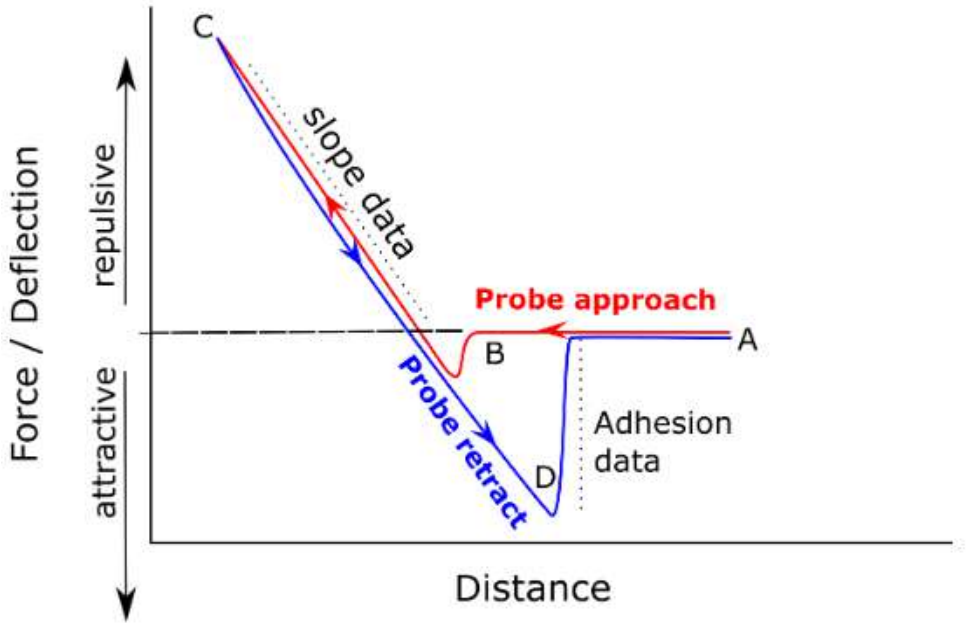

Figure 2.12: Example of a force curve. The x-axis represent the position of the cantilever in respect to the sample, y-axis represents the deflection of the cantilever, in red is represented a typical approach curve, whereas in blue it is represented a typical retraction curve. Adapted from [43].

2.5.2 Force Spectroscopy Atomic Force Microscopy to measure lung tissue

Force spectroscopy AFM can be used, in biomedical applications, to evaluate changes in stiffness (described as the Young's modulus) for different tissue types, such as liver [44], lungs [45], and brain [46].

Several contact mechanics models are used to model the tip-sample interaction and extract biomechanical information of the measured sample. In this work, the **Hertz model** was chosen. It assumes that the sample is elastic, homogeneous, and requires the usage of a spherical and not deformable tip. In this presented work, cantilever with spherical bids were used and the ROI of the lung tissue measured can be considered elastic and homogenous, fulfilling all the above-

mentioned boundary conditions. The Hertz model correlates the force with the indentation, allowing the calculation of the Young's modulus with the following equation:

$$F = \frac{4E_{tissue}r^{0.5}}{3(1-\nu^2)}\delta^{\frac{3}{2}} \qquad E_{tip} \gg E_{tissue} \tag{2.10}$$

Where E is the Young's modulus, F is the force, r is the contact radius (radius of the spherical indenter), ν is the Poisson ratio (in the presented work it was set to 0.5), and δ the indentation depth. Equation 2.10 holds only true if the Young's modulus of the tip is way greater than the Young's modulus of the sample investigated.

2.6 Small Angle X-Ray Scattering (SAXS)

Small angle X-Ray Scattering (SAXS) is an analytical method used to determine the nanoscale structures approximately in the range between 1 and 100 nm in terms of particle size, shapes and their near range order. When the X-rays irradiate the sample, the atoms inside scatter in all directions. There are two types of scattering processes that can occur: Compton scattering (inelastic scattering) and Rayleigh and Thompson scattering (elastic scattering - being relevant for SAXS). In this second case, when photons hit electrons, they start oscillating at the same frequency of the incident radiation. As a consequence of this acceleration, they start to emit an electromagnetic radiation with the same frequency. Since all the neighbouring atoms oscillate synchronously with each others, they produce "coherent waves" which can create interference patterns caused by the phase difference of the emitted radiation detectable with a detector. The internal structure of a material generates a characteristic interference pattern, that can be described by the Fourier transformation of the electron density difference in the sample. SAXS is an accurate and non-destructive technique that requires only a minimum of sample preparation. The basic set-up is made of an X-ray source, a collimator resulting in minimal beam divergence and small beam size, a sample holder, and a detection system, which measures the radiation scattered by the sample in a certain angles range. A beam stopper is used to block the intense incident beam in front of the detector for two reasons: the high intensity might destroy the detector, and it overshadows the weak scatterings signals of the sample.
Table 2.1 is meant to provide some helpful definition and equations for a better understanding of the analysis of the SAXS data presented in chapter 8.

Symbol	Equation	Information
k	$k = \frac{2\pi}{\lambda}$	For a travelling wave the wave number gives the change in phase per length.
$\mathbf{q}$	$\mathbf{q} = - \frac{2\pi}{\lambda} (\mathbf{s} - \boldsymbol{s_0})$	The scattering vector is given by the product between the wave number and difference between the unit vector of the incident beam and unit vector of the scattered beam.
$\gamma(\mathbf{r}) \equiv \Delta\tilde{\rho}^2$	$\gamma(\mathbf{r}) = \int_V \Delta\rho(\boldsymbol{r_1})\Delta\rho(\boldsymbol{r_1} - \boldsymbol{r})d\boldsymbol{r}$	The *convolution square* of the electron density fluctuation. It is also called *spatial autocorrelation function* (ACF).
$\gamma(0)$	$\gamma(0) = (\Delta\rho)^2 \int_V d\boldsymbol{r} = (\Delta\rho)^2 \cdot V$	For a homogenous particle, the ACF is equal to the square of the scattering contrast ($\Delta\rho$) times the volume fraction (V).
$\lvert F(\mathbf{q})\rvert^2$	$\lvert F(\mathbf{q})\rvert^2 = \int_V \Delta\tilde{\rho}^2 e^{-i\boldsymbol{qr}} d\boldsymbol{r}$	The scattered intensity is the Fourier transformation of the spatial ACF of the density fluctuation of the particle
$I(q)=\langle\lvert F(\mathbf{q})\rvert^2\rangle$	$I(q) = 4\pi \int_0^\infty \gamma(r) r^2 \frac{sin(qr)}{qr} dr$	The spatially averaged scattering intensity I(q) is the Fourier transform of the correlation function $\gamma(\mathbf{r})$ averaged over all the directions in space. I(q) is proportional to the volume fraction (V), the square of the scattering contrast ($\Delta\rho$), and dimension (r) of the scatterers in the media.
l_c	$l_c = \frac{1}{2\pi\overline{\Delta\rho^2}} \int_0^\infty I(q)dq$	The correlation length is related to the shape and dimension of the scatterer media only.

Table 2.1: Summary of equations and definitions helpful to better understand the SAXS measurements and analysis presented in chapter 8. I(q) and l_c were the parameters calculated during the scattering measurements. The equations are reported from [47].

2.7 Image registration

Image registration is a process that allows the precise co-localization of two or more images. Thus, successful image registration allows supplementing the information of one image modality with another and therefore aids in a more accurate tissue classification. Therefore, a high accuracy of image registration is crucial for the here presented analysis pipeline. While registering images from the same modality is usually simple, the registration of data from different techniques such as for example micro-CT and histology is more challenging as the data shows differences in image dimension, image content and might even be subject to deformations. Thus, the main problems in image registration are:

- the dimensions of the output of the imaging modalities do not match (e.g. 2D and 3D).
- the image content of one modality seems deformed with respect to the other
- the different image content hinders the quantification when a perfect overlap has been achieved.

To deal with the first problem, the common approach is a dimensionality reduction to the smallest dimension in common. For instance, in the registration of histological (2D) and micro-CT data (3D), the common dimension is 2D, thus a virtual slice (2D) from the micro-CT data is extracted, and then the fusion can be performed. Otherwise, the image with the lowest dimension can be placed in a subspace of the data with the highest dimension (e.g. place the histological data on a plane in the 3D micro-CT data), figure 2.13a. Moreover, to enable the application of different modalities, additional sample preparation steps might be required. For instance, the application of histology requires physical sectioning of the specimen (typically using a microtome) which introduces deformations. Therefore, just overlying the two images would not result in a good registration (figure 2.13b), whereas if the deformations are compensated by elastic registration a better match can be achieved, figure 2.13c.

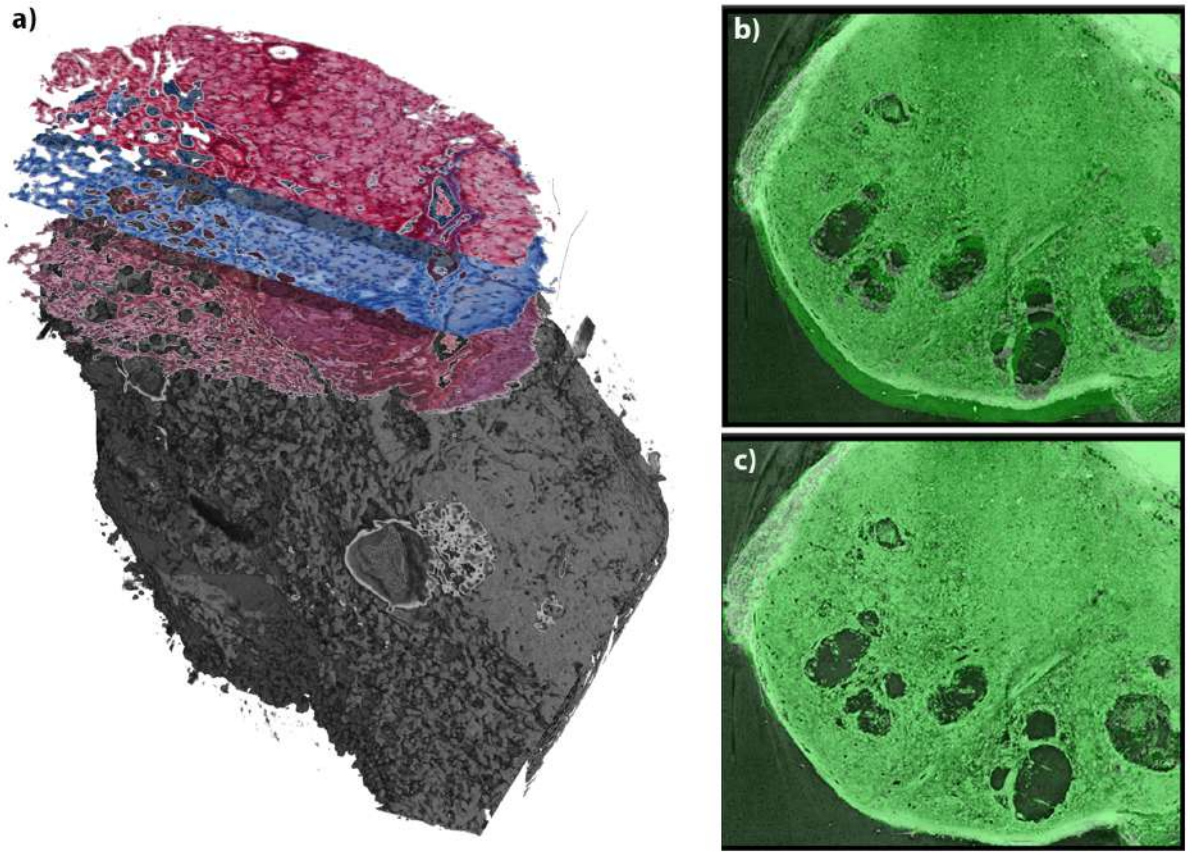

Figure 2.13: Example of image registrations. a) Overlap of 2D histology on 3D micro-CT data set. Here, the image with the lowest dimension (histology) is placed in a subspace of the image with the higher dimension (micro-CT). Overlaying of histology on micro-CT data b) without compensation for the deformation caused by microtome sectioning c) after applying compensation for the deformation. a) Courtesies of Justus Alves, b) and c) adapted from Albers et al. [48].

To achieve such image registration, typically a pipeline as shown in figure 2.14 is applied. One image is treated as ground truth and will not be modified - fixed image. The other image will be deformed to achieve the best possible match with the fixed image - floating image. Different transformation types can be considered: i) rigid body transformation, allowing for translation and rotation, ii) affine transformation adding zooming, shearing, and the iii) elastic transformation allowing stretching the image locally. In the case of histology, the common approach is to deform a 2D image to compensate the modifications introduced during the tissue sectioning. Since this deformation depends on the differences in the stiffness of different tissue types, elastic registration is needed for its compensation. As the floating image is typically a data set on a regular grid, its deformation would yield in a non-regular grid, which is mapped to a new regular grid of the same resolution as the fixed image using image interpolation. Generally, this could be performed using a polynomial with the order equals to N-1, where N is the number of points that need to be interpolated (for an image N is equal to the number of pixels). Unfortunately, this approach can lead to strong deviation from the original data - over-fitting. To solve this problem, the interpolation is done by a combination of polynomials of lower order (usually 3rd order). This is called spline interpolation. The last problem to deal

with, during the registration process, is the evaluation of the performances. Commonly, two metrics are used: cross-correlation and mutual-information. The first requires that structures that are bright in one modality are also bright in the second one, whereas the mutual-information requires that the regions are homogeneous in both imaging approaches. Therefore, it can be summarized that cross-correlation is an intensity based metric whereas mutual-information is a metric based on pairing the intensities at a certain pixel in both the images for the registration. Both metrics have their own limitations: while cross-correlations fails if structures of interest in both modalities do not have high intensities, mutual-information usually bins the intensity levels of the images to only a few different levels and has therefore problems if the structures of interest have a poor contrast. Both approaches fail if the images content is not homogeneous, such as in the combination of PET and CT for instance. In such cases additional marker are needed. In all cases used in this study, all image pairs had homogeneous structures and therefore mutual information was chosen as cost-function.

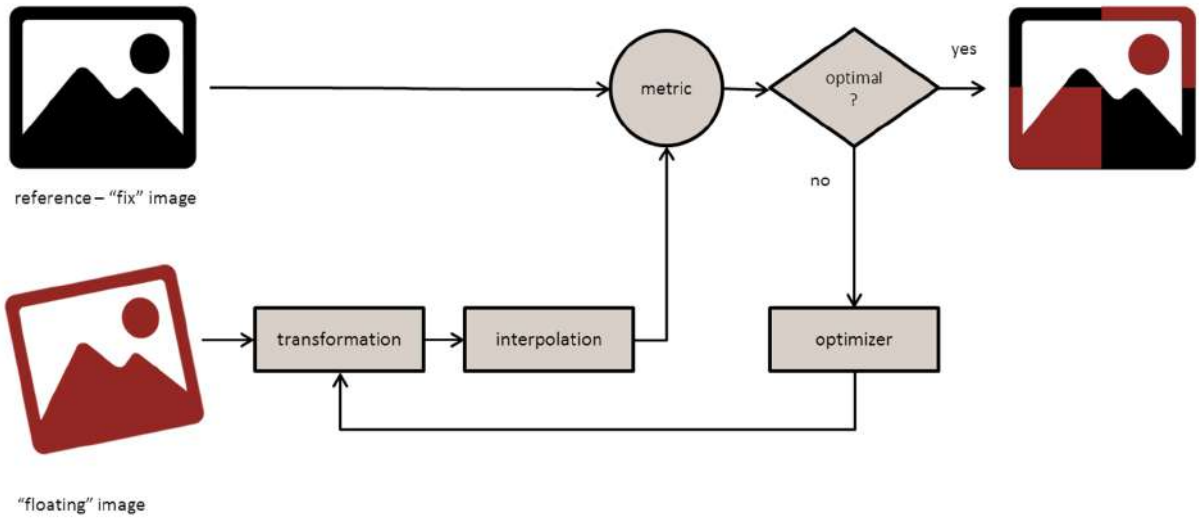

Figure 2.14: Sketch of the image registration pipeline. This example concerns the registration of two images, where one is considered fixed and one "floating". The latter is the one which undergoes both the transformation and interpolation processes. After this, an evaluation of these previous processes is done using a metric (cross-correlation or mutual information).The transformation and interpolation steps are repeated until their output is not optimized.

Chapter 3

Animal models of PF and in-vivo analysis

Both mouse models of pulmonary fibrosis, considered in this thesis, have extensively been studied in-vivo using micro-CT imaging to depict the progression of structural alterations as well as the changes in the inspiration and expiration lung volume. In addition, different types of lung function test were conducted in parallel.

3.1 Introduction to fibrosis mouse models

Due to the complexity of lung diseases and strong interplay with the immune systems, in-vivo animal models are still required, especially if disease progression and therapy response needs to be assessed. Most commonly mouse models are used for this purpose, not only due to economical reasons, but also because the inbred mouse strains show very low inter-subject variability, which allows keeping the animal numbers at a minimum.
However, the smallness of the mouse, its short lifespan as well as the rapid breathing rate pose great challenges for in-vivo imaging and lung function testing. In addition, the translatability of the obtained result to human patients is critically discussed [49]. It is certainly true that due to the rapid breathing rate, the lung architecture (despite being simply smaller) is largely different with respect to humans. Nevertheless, the lung fibrosis mouse models used in this study are commonly applied in research and have proven to mimic human lung fibrosis to a large extent. More importantly, the concerns about their comparability with human lung fibrosis are not relevant for the here presented thesis, aiming to characterize differences in the fibrotic processes without claiming that exactly the same composition of fibres will be found in patients.
All in-vivo animal work was performed either at UMG Göettingen as part of the PhD thesis of Amara Khan (Bleomycin model and Nintedanib treatment) or by Dominik Leitz UKH Heidelberg (Nedd4-2 model). The here shown in-vivo data is presented for completeness of the thesis and to provide the needed background for the origin of the analysed specimen. All analysis presented in the thesis were performed on formalin fixed and paraffin embedded lungs of those mouse models.

3.2 Bleomycin model and Nintedanib treatment

3.2.1 Study design

Pulmonary fibrosis was induced in 8 mice at day 0, 2 mice received a Nintedanib treatment daily from day 7 to day 20. Additional 3 mice were used as healthy controls. All mice were scanned in an in-vivo micro-CT scanner (QuantumFX, Perkin Elmer) using two protocols: A) planar cinematic radiography over 30s and B) tomography scan over 4.5mins. For both sequences a tube voltage of 90kV and a field-of-view of 20 x 20 mm^2. Based on the binned camera matrix of 512 x 512 px this resulted in spatial resolution of approximately 40 µm. The planar acquisitions were done with a frame rate of 30 fps and a tube current of 100 µA resulting in a x-ray dose of approximately 37 mGy, while the CT scans were done with a tube current of 200 µA resulting in a dose of 290 mGy.
All mice were anesthetized with 2% isoflurane in 1 L 50/50 mix of oxygen and air per min. Anesthesia was performed with a face mask to allow for spontaneous breathing. The breathing frequency was adjusted to about 0.7 Hz by adjusting the isoflurane concentration.
Mice were sacrificed at day 21, the lungs were harvested and gently inflated with 1 ml formalin. The specimens were then completely immersed in formalin and processed as described in chapter 2 prior to all follow-up studies. The study design is summarized in figure 3.1. In table 3.1 are reported the number of mice for each group, used in the here presented thesis.

experimental group	# of mice	weight [g]	age [d]
Healthy controls (CN_{ble})	4	25.0 ± 1.0	186.8 ± 44.5
Bleomycin (PF_{ble})	7	14.1 ± 1.7	97.5 ± 4.0
Bleomycin + Nintedanib ($PF_{ble} + Nin$)	2	19.4 ± 3.3	100.0 ± 1.4
Control of genetic model (CN_{gen})	6	29.8 ± 3.6	174.0 ± 13.4
Nedd4-2 KO (PF_{gen})	17	27.8 ± 4.1	183.1 ± 37.7

Table 3.1: Overview of the different animal models used. Values are displayed as mean ± standard deviation.

All studies were approved by the local authorities of the university hospital Göettingen Germany, the county Lower Saxony and were in accordance with national and European law.

3.2.2 Results

A planar cinematic radiography protocol has been established by the group of UMG Göettingen to derive functional parameters in mouse lung disease models [50]. It was first applied to mouse models of allergic airway inflammation mimicking human asthma, but has recently also been used in other mouse models such as *mdx* a model for Duchenne disease [51]. The basis of the approach is as follows. The breathing changes the air volume in the lung and thereby the average x-ray attenuation over the chest. This average attenuation function over time is calculated showing specific disease related alterations, which can be quantified. In case of lung fibrosis especially the time constant of the decay in the expiration phase was found to be significantly different between healthy controls, fibrotic and treated animals. Figure 3.2a shows one example mouse of each of

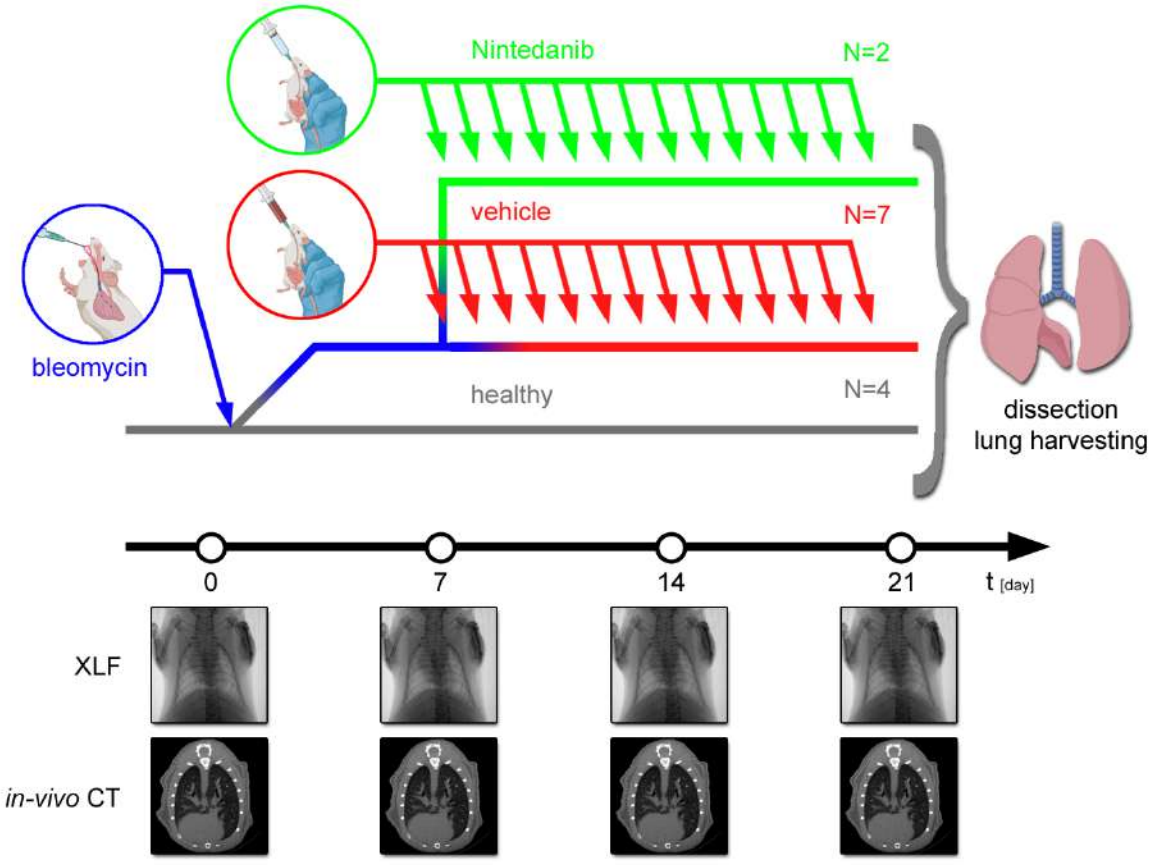

Figure 3.1: Study design: mice were measured four times by planar cinematic radiography to measure lung function (XLF) and in-vivo retrospective gated micro-CT (in-vivo CT) to measure lung volume in inspiration. Directly after a baseline scan at day 0 lung fibrosis was introduced in 9 mice by intra-tracheal instillation of bleomycin. After a scan at day 7, two mice recieved a Nintedanib treatmenent every day until day 20, while the other fibrotic mice received NaCl as a vehicle at the same time points. Mice were measured again at day 14 and day 21. Following the last measurement mice were sacrificed, dissected and the lung was processed for subsequent analysis. Four healthy mice served as controls.

the three groups at maximum expiration. The lung area of the untreated mouse appears darker as a result of the ongoing fibrosis (day 21, prior dissection). Figure 3.2b shows 4 to 5 breathing periods of the recorded attenuation function for a healthy mouse (green), an untreated mouse (red) and a treated mouse (blue). The functions differ in baseline and amplitude as well as in the shape of the peaks. The analysis of the decay rate of the expiration phase at the four different time points (figure 3.2c) shows that while starting at the same value the untreated and treated mice clearly show a strong reduction of the decay rate between day 0 and day 7. At day 7 the Nintedanib treatment started. At day 14 the treated mice had not only regained the decay rate of the healthy mice but also demonstrated slight over-compensation due to the treatment, while the untreated mice showed a slight worsening of the fibrosis. At the end of the experiment at day 21 treated mice showed similar decay rates as the healthy controls. However, the untreated mice also showed an improvement of the decay rate. This “spontaneous” healing of the fibrosis is a known aspect of the Bleomycin model and has led to discussion of the translatability of the

results as in humans a healing of fibrosis cannot be found. New studies suggest that only older mice should be used for the Bleomycin model, as they typically show no or much less recovery [52]. However, in this study, the mice were only 6 weeks old at the beginning of the experiment.

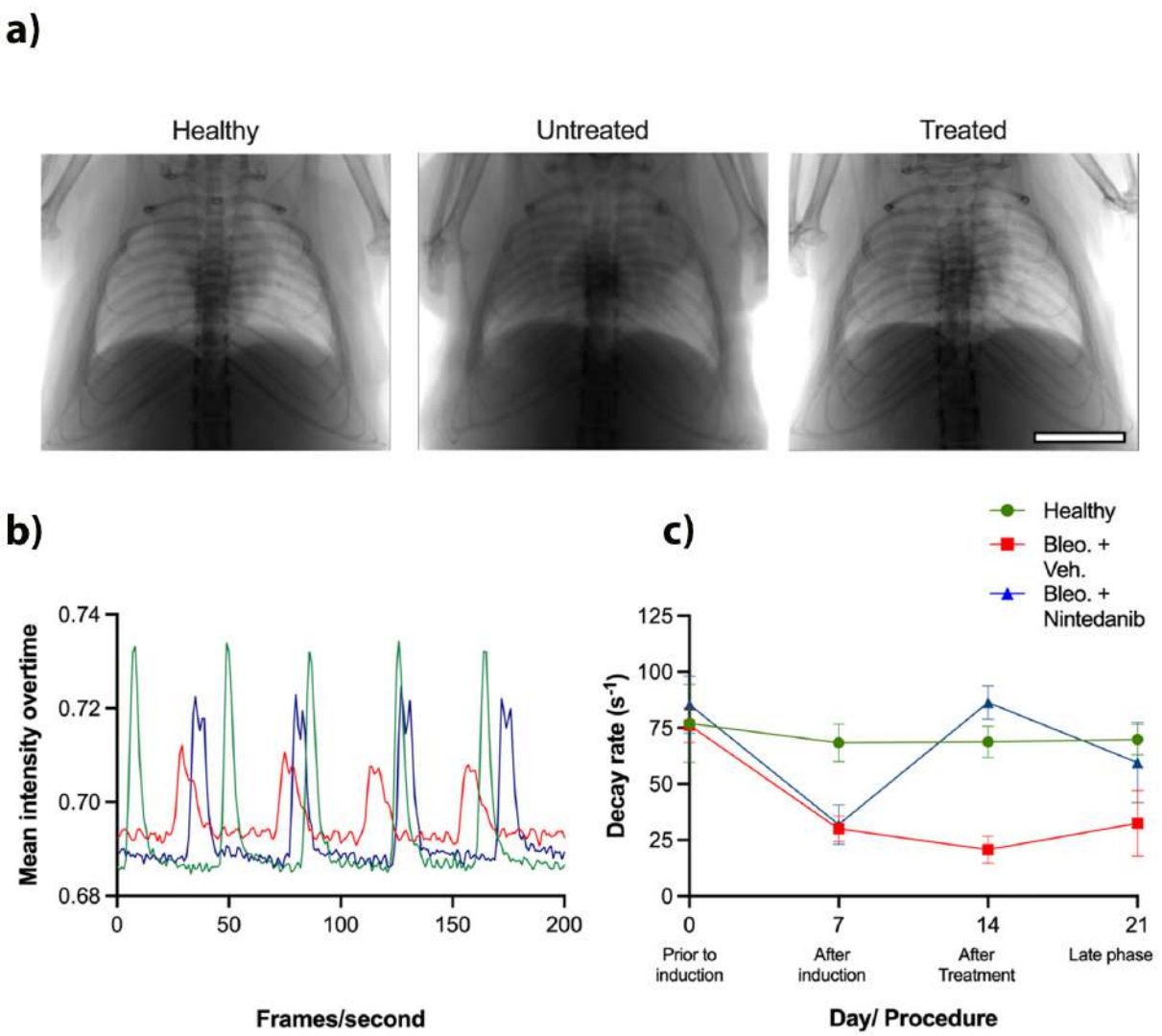

Figure 3.2: Radiographic XLF measurements performed in healthy, vehicle treated (bleo. + vehicle) and Nintedanib treated mice (bleo. + Nintedanib). A) Radiographic Anterior Posterior projection of the chest region presenting the differences in x-ray attenuation at the lungs in all groups on day 21. B) Graph showing representative x-ray transmission curves for four breathing cycles acquired at late phase of LF (day 21) for all groups. C) Graph of decay rates for healthy (green), as well as bleo. + vehicle (red) and bleo. + Nintedanib treated LF mice (blue) at different time points. On day 0, a single dose of bleomycin was instilled i.t. following baseline lung function measurements and decay rates 7 days after LF induction, vehicle (1% Tween 80/PBS) or Nintedanib treatment, both orally administrated daily until day 21. Scale bar: 0.5 cm (A). Khan et. al. [53].

In addition, retrospective gating was performed to sort the acquired in-vivo CT data sets into two bins representing the end inspiration and end expiration time points. The total lung volume was segmented in the inspiration phase (Please note that due to the limited spatial resolution, which worsens if only the few inspiration data frames can be used, only a segmentation of air was possible). Figure 3.3a shows an example slice through data sets of one mouse of each group

including the segmentation of the airated lung regions. Figure 3.3b demonstrates that a similar trend can be seen in the total inspiration volume as found in the decay rate, however that standard deviation of the results as shown by the error bars was larger than for the more simple planar functional analysis.

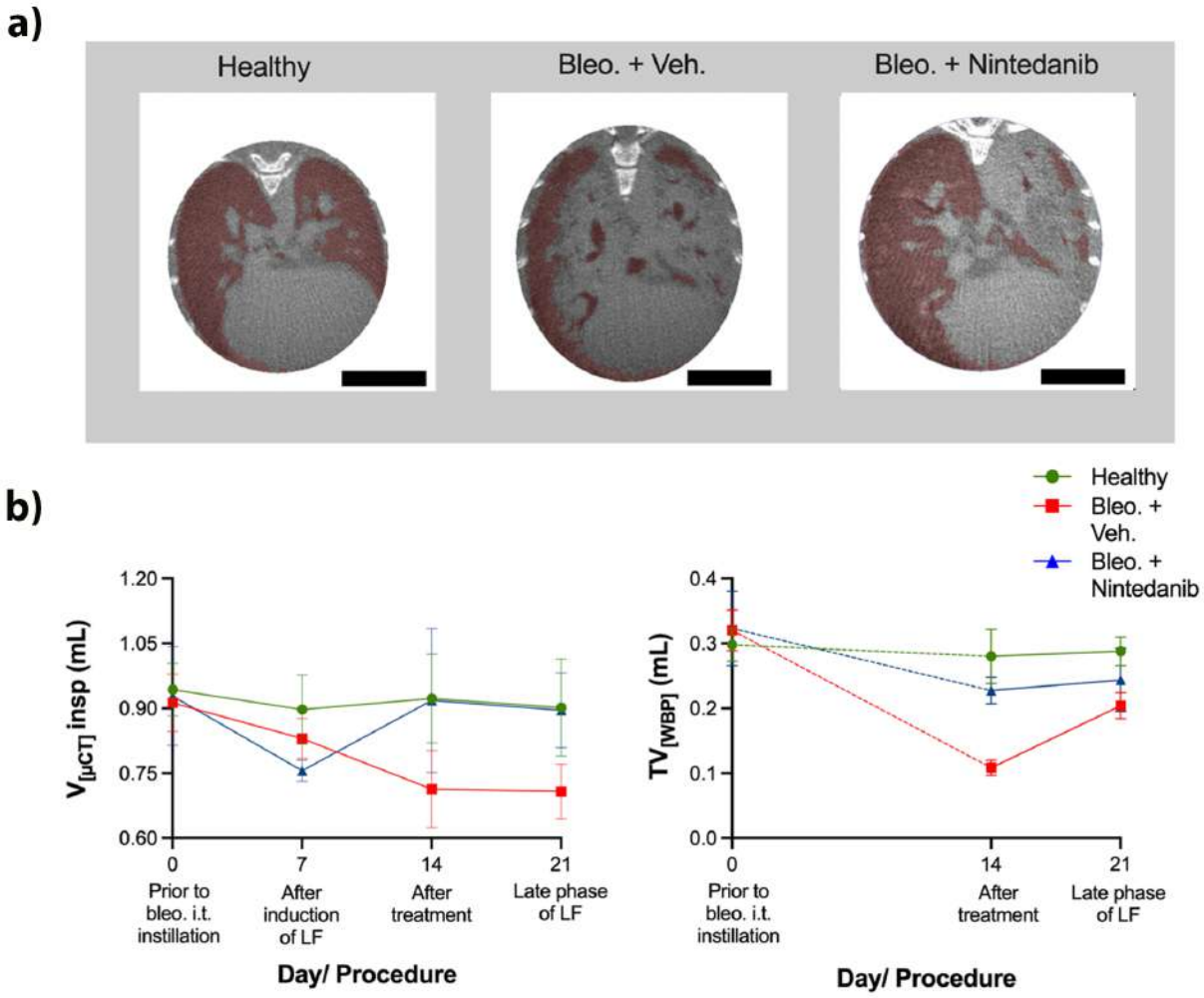

Figure 3.3: Lung volume assessment using micro-CT in healthy, vehicle treated LF (bleo. + vehicle) and Nintedanib treated LF mice (bleo. + Nintedanib). A) The micro-CT measured lung volume at inspiration ($V_{\mu CT}^{insp}$) (red masked regions) derived from the segmented aerated regions of the lung through a region growing method is shown for a healthy, bleo. + vehicle and bleo. + Nintedanib treated LF mouse. B) Graphs showing micro-CT measured $V_{\mu CT}^{insp}$ for healthy (green), bleo. + vehicle (red) and bleo. + Nintedanib treated LF mice (blue) at different time points. Scale bar: 1 cm (A). Modified from Khan et. al. [53].

Overall, the in-vivo measurements in the Bleomycin model show that the severity of lung fibrosis can be addressed on a functional and structural level by in-vivo micro-CT imaging. Moreover, disease progression and therapy response can be monitored. However, those measurements are not able to reveal the localization of fibrotic regions or to address the fibrotic burden in detail, especially the characterization of differences in the formation of pulmonary fibrosis, which is the aim of this thesis, cannot be performed.

3.3 Nedd4-2 mouse model for pulmonary fibrosis

Nedd4-2 is an E3 ubiquitin protein ligase involved in posttranscriptiptional regulation ubiquitination and targeting for proteasomal degradation of proteins implicated in the pathogenesis of lung disease including surfactant protein C (S*ftpc*), the epithelial sodium channel ENaC and Smad2/3, the intracellular mediators of transforming growth factor β (TGFβ) signaling. By conditional deletion of Nedd4-2, a mouse model was generated that develops in contrast to the above explained Bleomycin model spontaneously and progressively lung disease mimicking core features of pulmonary fibrosis [18].
For the purpose of the thesis the conditional Nedd4-2 knock-out model was chosen as the very different pathways - injection of Bleomycin on the one hand and conditional deletion of Nedd4-2 - gave rise to the assumption that the fibre deposition will show differences. Therefore, Nedd4-2 in comparison to Bleomycin should have been an ideal starting point to analyse the diagnostic value of the analytic pipeline to be established within the thesis. It warrants repetition that a difference in composition of the fibrotic regions has never been previously reported.

3.3.1 Study design

For the induction of Nedd4-2 deletion, mice were exposed to 1 mg/ml doxycycline hydrochloride dissolved in a 5% sucrose solution supplied as drinking water. The fresh solution was given at least every three days. Mice without being exposed to doxycycline hydrochloride served as controls.
In-vivo CT imaging was performed using an in-vivo micro-CT (SkyScan 1176, Kontich, Belgium) operated with the following settings: tube voltage 50 kVp, tube current 500 µA, a 0.5 mm aluminium filter, camera exposure time of 55 msec, 720 projections over 360 using a field of view of 30 x 30 mm^2 resulting in a voxel size of 35 µm on 1000 x 1000 x-y-planes. The scanning time was approximately 12 mins per acquisition. Mice were imaged once per month over a duration of 5 months in order to address disease progression.
Pulmonary function testing (PFT) was performed using the FlexiVent system (SCIREQ, Montreal, Canada). Mice were anesthetized using sodium pentabarbital (80 mg/kg), tracheoteomized. After relaxation with pancuronium bromide (0.5 mg/kg) mice were ventilated with a tidal volume of 8 ml/kg at a frequency of 150 breaths/min and positive end expiratory pressure (PEEP) of 3 cmH_2O. The static compliance was derived from pressure volume curves.
After an additional ex-vivo post-mortem CT lungs were harvest, frozen and stored at -20 °C.
The entire schedule is reported in figure 3.4.

3.4 Results

Standard fibrosis scoring was performed in the monthly acquired micro-CT scans. Revealing a significant increase after 3 months compared to control mice and a strong progression in month 4 and 5 (figure 3.5). The PFT showed a good negative correlation of the lung compliance with the in-vivo fibrosis score of the CT data (figure 3.5).
In summary, the Nedd4-2 conditional knock-out model for pulmonary fibrosis showed the ex-

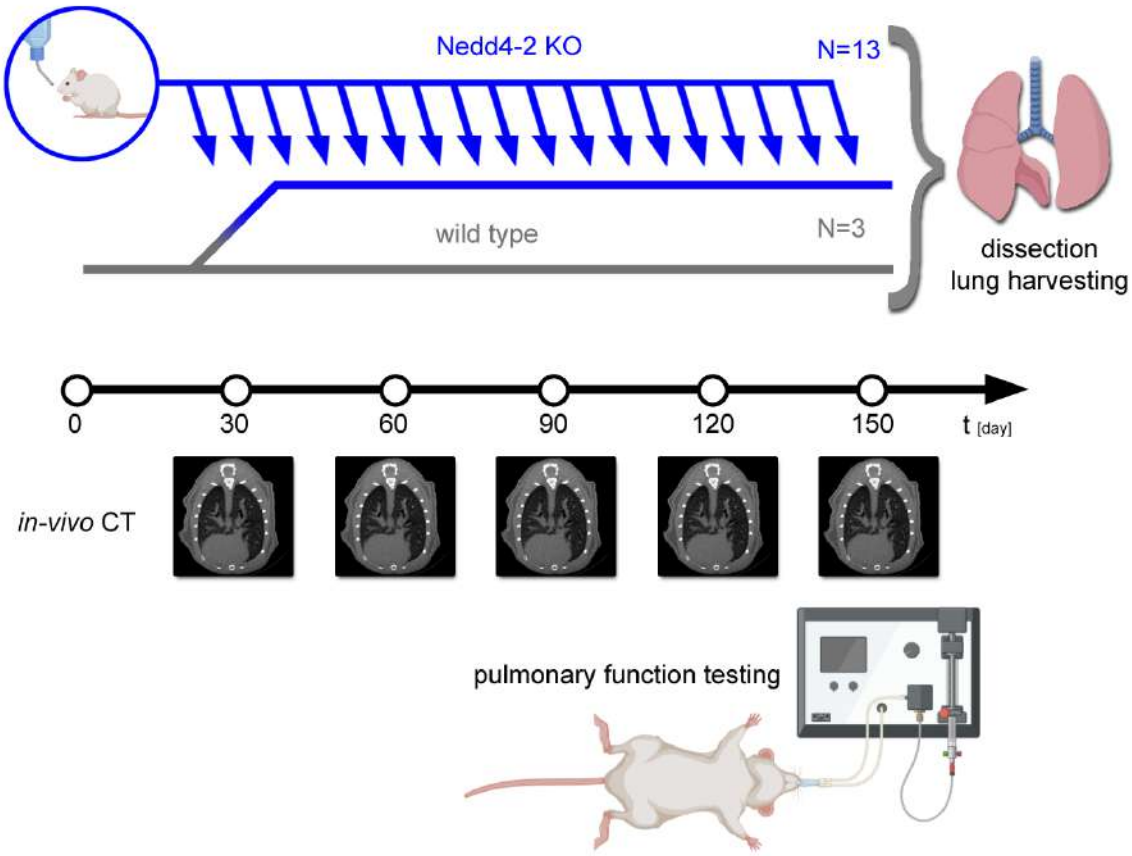

Figure 3.4: Nedd4-2 in-vivo experiment schedule. Mice were analyzed by in-vivo micro-CT in a monthly interval. At day 30 mice received doxycycline hydrochloride via the trinking water to develop lung fibrosis based on the Nedd4-2 conditional knock-out. At day 150 mice pulmonary function testing was performed. Following this invasive procedure mice were sacrificed and the lungs harvested for subsequent analysis. Three wild type mice served as controls.

pected progressive features of lung fibrosis in both structural changes as observed by in-vivo micro-CT as well as in lung compliance as measured by PFT

3.5 Summary of the in-vivo results of both models

Both models developed functional and structural alterations of the lungs mimicking human lung fibrosis. Based on the performed tests, lung function measurement and in-vivo micro-CT, the two models are indistinguishable from each other. Since, especially, the Nedd4-2 model demonstrated strong variations of the magnitude of the fibrotic burden and different techniques were used for assessing disease progression in the two models, I used the Ashcroft score in the histological sections done by the same observers in a blind manner as reference value (ground truth) for all subsequent analysis in the pipeline developed in my thesis.

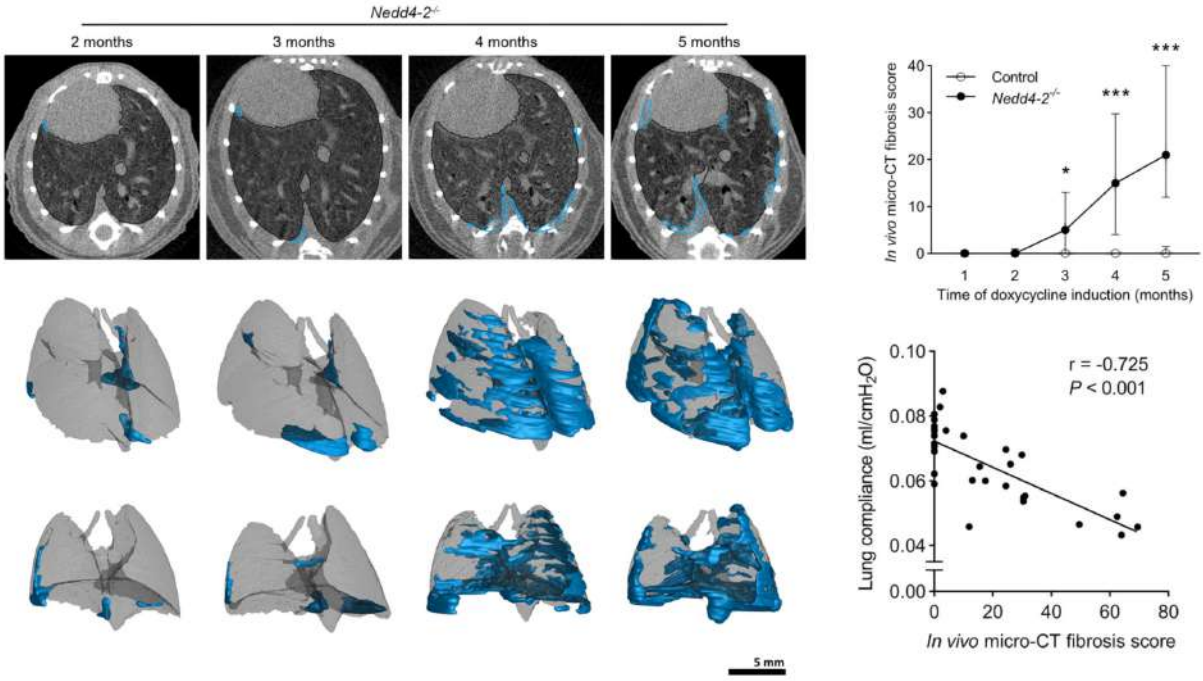

Figure 3.5: Representative in vivo micro-CT images of a spontaneously breathing conditional Nedd4-2 mice scanned at the indicated time points after oxycycline induction. Fibrotic areas are indicated in blue. 3D reconstructions of fibrotic lesions (blue) in the lungs of the same mouse as shown in c after 2, 3, 4 and 5 months of doxycycline induction. n = 4-14 mice/group. *p $<$ 0.05, ***p $<$ 0.001. Summary of in vivo micro-CT fibrosis scores. Modified from Leitz et. al. [54].

Chapter 4

Propagation-based phase-contrast imaging

In this chapter, the set-up for the phase-contrast imaging of paraffin embedded lung, as well as the acquisition and the analysis approach are presented.

4.1 Material and Method:

4.1.1 Micro-CT set up for paraffin embedded lungs tissue imaging

All the specimens were scanned at the SYnchrotron Radiation for Medical Physics (SYRMEP) beamline, figure 4.1. The acquisitions were performed using the white/pink beam configuration in propagation based phase contrast mode, with a sample to detector distance of 150 mm. The beam was filtered with a silica foil with a thickness of 0.5 mm, resulting in a mean energy of 16.7 keV. 360°off-centre scans with 3600 projections, and an exposure time of 50 ms per projection, were performed using a water-cooled Orca Flash 4.0 sCMOS detector (2048x2048 pixels) coupled with 17 µm Gallium Gadolinium Garnet (GGG) scintillator. The pixel size was 2 µm, resulting in a reconstructed FOV of roughly 7x4 mm^2. To capture most of the lung tissue, about 2 and 3 scans were performed with a vertical offset of 3.5 mm. The reconstruction of the slices was performed using SYRMEP Tomo Project (STP) software [55]. Before the use of filtered back-projection, the TIE-Hom phase retrieval algorithm [56] was applied with a δ/β ratio of 100. Subsequently, all the vertical steps, for each lung, were stitched together using a python script, to cover the full lung.

Figure 4.1: Experimental hutch of the SYnchrotron Radiation for Medical Physics (SYRMEP) beamline at the Italian synchrotron Elettra.

4.1.2 Identification of fibrotic regions and evaluation of structural changes in paraffin embedded lung tissue

The full 3D volume of the lung was used to investigate the structural changes and to identify the position of fibrotic regions inside the organ. The latter was a crucial step for the success of the pipeline, as it allowed to precisely cut the paraffin block at the depth of the fibrotic regions and prepare the tissue for the next techniques in the analysis process. All the full 3D lung volumes were converted into 8-bit and loaded in the software VGSTUDIO MAX™to perform the structural analysis as well retrieve the positions of pathological regions. Figure 4.2a shows an example of a full 3D lung volume. The paraffin was virtually removed to demonstrate that the entire structure of the lung can be visualized. During the micro-CT scans, the samples were placed in the holder manually, resulting in not an always 100 % straight vertical alignment. Therefore, before performing any analysis, the edge of the paraffin block was used as reference, and the 3D volumes were realigned until the surface of the embedding medium was straight. After this preliminary step, a manual threshold was applied to extract the surface of the lung. Three regions were selected inside the 3D volume of the organ: fibrotic, mild-fibrotic, and healthy regions, to cover all the possible tissue scenarios. In the case of CN_{bleo} as well as of CN_{gen} only the healthy regions were measured, since no tissue consolidation was present. To cover the whole organ along the vertical direction, between 5 and 6 cubes with the length of 300 µm were extracted from the previously generated lung surface. Figure 4.2b shows the view of the xz plane, where the cubes are shown in light blue.

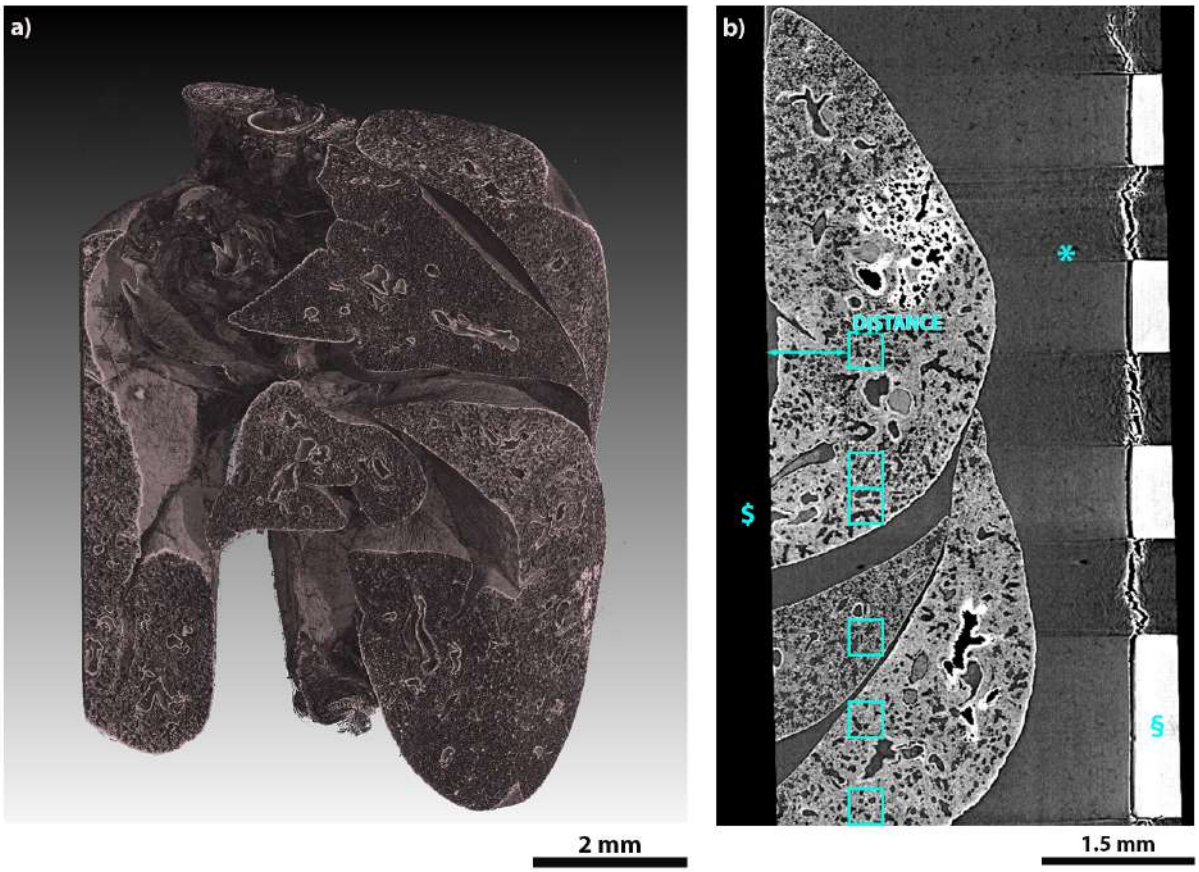

Figure 4.2: Example of a 3D volume and its xz view. a) 3D representation of a full lung. b) xz view of the 3D volume. Note: * indicates paraffin,§ indicates the plastic bars of the cassette used for the inclusion, $ indicates the air.

To calculate the structural changes of the tissue, the following parameters were retrieved: tissue volume, air volume (more precisely the volume of the paraffin filled air spaces), surface area, closed surface area, surface area difference, body volume/total volume (BV/TV), and body surface/body volume (BS/BV). Figure 4.3 is used only for the explanation purposes of the surface parameters calculated during the morphological analysis. The orange cube represents the volume portion extracted from the lung, the blue object the lung tissue and the void the paraffin. In the calculation of the surface area, the portions of the object cut by the cube (yellow regions in figure 4.3) are ignored, whereas in the closed surface area they are taken into account. Moreover, the difference between these two parameters increases if big structures (e.g. fibrotic consolidation regions in the lungs) intersect the surface of the box. In addition, both the tissue volume (BV/TV) and the surface (BS/BV) normalized by the total volume were also calculated. BV/TV provides the amount of lung tissue in percentage respect to the total volume of the cube used for the analysis. Then the positions of the measured regions, that were exploited for the cutting procedures (5.1), had been calculated, as shown in figure 4.2b.

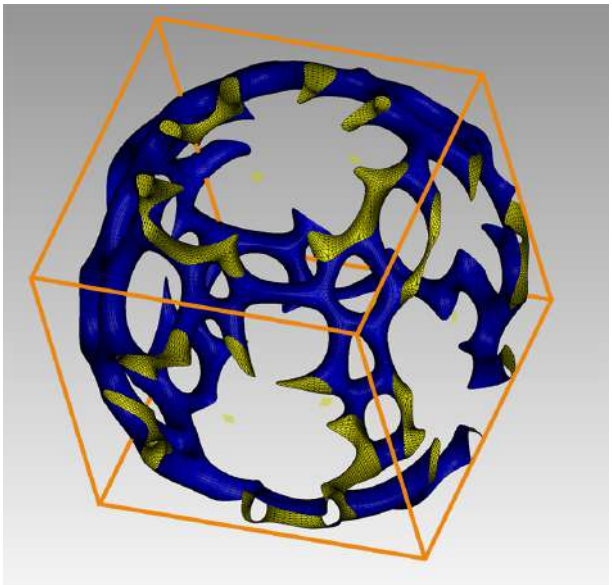

Figure 4.3: Sketch of a 3D object used to explain the morphological parameters calculated from the PBI measurements. The orange cube mimics the cube extracted from the lung volume, the blue object represents the lung tissue, and the yellow regions are exploited to explain the surface parameters calculation.

4.2 Results: Structural changes in fibrosis revealed by morphological analysis using PBI

Figure 4.4a reports an example of the cubes extracted from the lung surface for each experimental group. More precisely, CN_{ble} ,PF_{ble}, CN_{gen}, and PF_{gen} are shown from left to right, respectively. Depending on the dimension of the organs along the vertical direction, between 5 and 6 cubes were extracted from the tissue. In the fibrotic lungs 3 areas were selected to cover all the possible scenarios: fibrotic, mild-fibrotic, and healthy regions; whereas for the control mice only the healthy regions were present and taken into account. Between 15 and 18 measurements of the following parameters were retrieved:tissue volume, air volume, surface area, closed surface area, surface area difference, body volume/ total volume (BV/TV), and body surface/body volume (BS/BV). Figure 4.4b-h display the results for each calculation. The statistical analysis was done using two Python3 packages, statannotation [57] and SciPy [58].
Pairwise none-parametric Mann-Whitney U test with Bonferroni correction for multi-comparison are presented with p>0.05 = ns (none significant), p≤0.05 = *, p≤0.01 = **, p≤0.001 = ***, p≤0.0001 = ****). All presented box plots are generated with the Seaborn python package [59]. The box represents the range between the 25^{th} and 75^{th} quartile, showing the median as an additional line in between. The whiskers extend to 1.5 times the interquartile range. Everything outside that range is considered an outlier and displayed as an individual data point.
Figure 4.4b reveals that the lung tissue volume is enlarged in both the fibrotic models in comparison to their control groups. Since in both PF_{ble} and PF_{gen} also mild-fibrotic and healthy regions were selected for the analysis, figure 4.4f and d depict larger variation for the surface parameters, if compared with CN_{ble} and CN_{gen} respectively. Figure 4.4h reveals that there are statistically significantly differences between the fibrotic models and their controls. Figure 4.4d

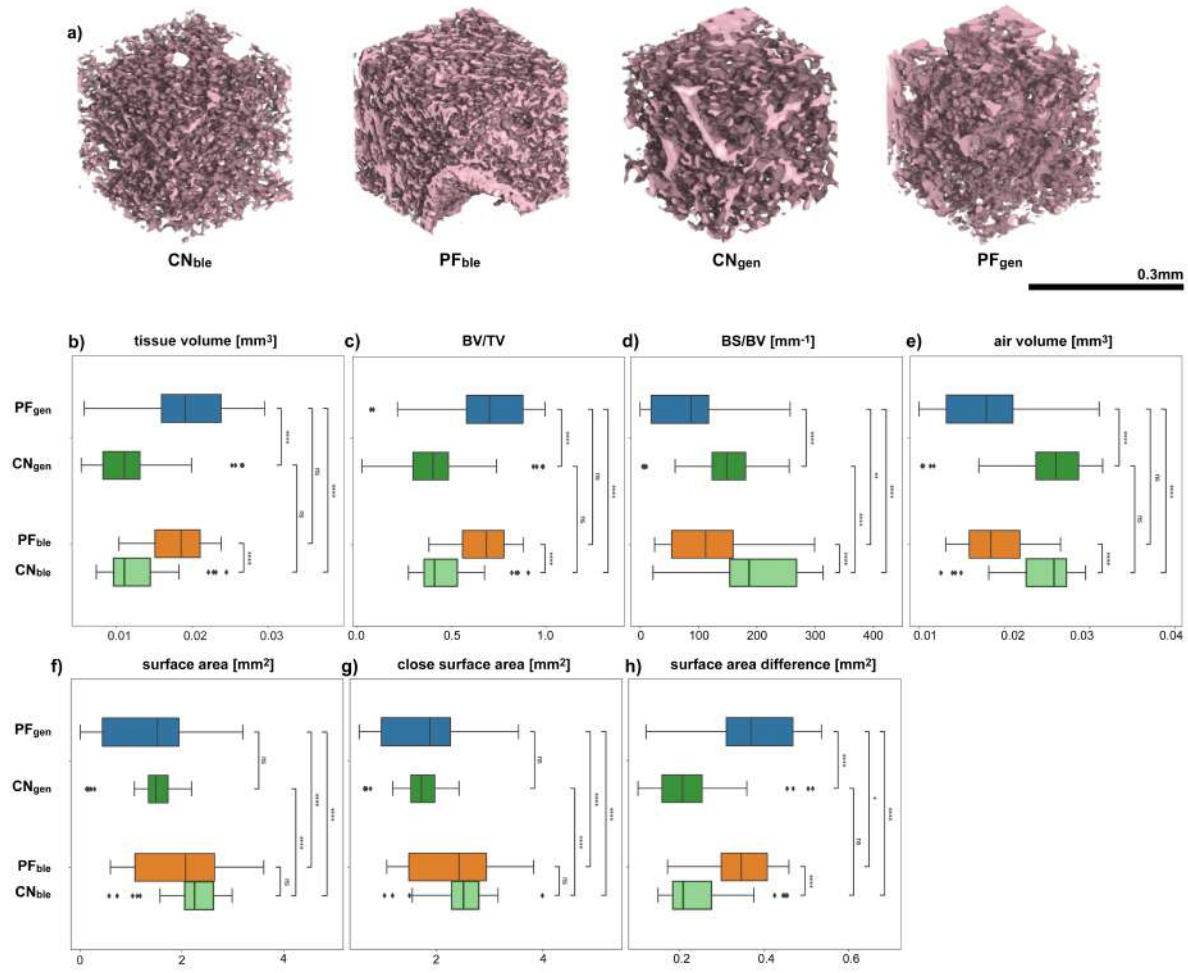

Figure 4.4: Quantification of anatomical alterations in lungs with pulmonary fibrosis. a) Representative images of three examples of the 300 x 300 x 300 µm analysis cubes are shown for a lung of CN_{ble} (n=3) ,PF_{ble} (n=6), CN_{gen} (n=9), and PF_{gen} (n=17), from left to right. Clearly, a reduction of the active surface and an increase in tissue volume is seen in both cases of lung fibrosis, however, much stronger in PF_{ble} lungs. b)-h) shows the quantification results for different parameters. The first two box plots depict the comparison between PF_{gen} mice and CN_{gen}, while the second ones show lungs of PF_{ble} and CN_{ble}. Clearly, both groups of mice with lung fibrosis express a larger lung tissue volume (b) and a reduced air volume. Interestingly, the surface area (as well as the closed surface area) does not show strong deviations from the respective controls (f and g). The body surface to body volume ratio (BS/BV) presenting the normalized surface of the lung tissue shows the expected reduction in both mice models of lung fibrosis, with a stronger tendency in PF_{gen} mice. This points to a reduction in the functional capability of the fibrotic lungs and also to stronger severity of the fibrosis in PF_{gen}. For each mouse 6 cubes were analyses taken from 17, 6, 9, 3 numbers of animals for PF_{gen}, PF_{ble}, CN_{gen} and CN_{ble} respectively. Statistically significant differences were determined using the Mann-Whitney test with Bonferroni correction for multi-comparison: ns p <= 1.00, *p <= 0.05, **p <= 0.01, ***p <= 0.001, ****p <= 0.0001.

shows a reduction of the relative surface area (BS/BV), which means presence of consolidated regions (bigger object) of tissue.

Summarizing, the morphological analysis revealed that a separation between fibrotic and healthy lung can be achieved based on the tissue volume, the BS/BV, and the surface area difference.

However, these parameters cannot take into account differences at the substructures level. Indeed, figure 4.5a reveals that the consolidation tissue for the PF_{ble} appear rather homogeneous, whereas in the case of PF_{gen} the presence of structures (red arrow in figure 4.5b), which are most likely blood vessels, is visible. To understand if a more comprehensive characterization of

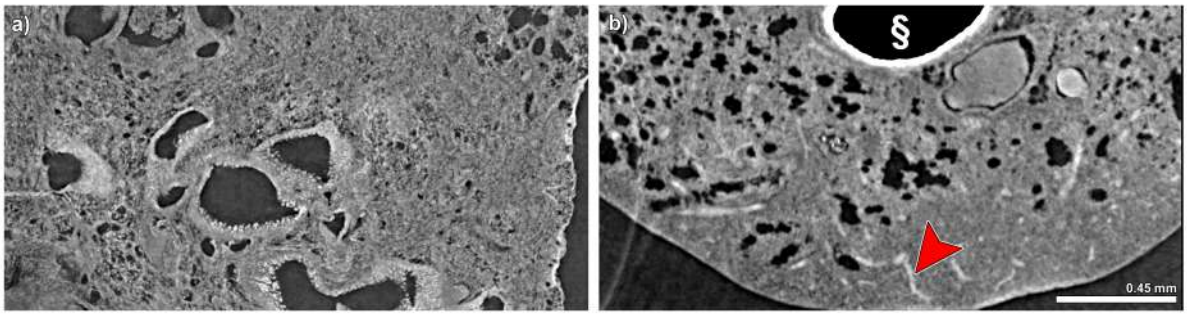

Figure 4.5: Maximum intensity projections of the PBI data for a) a PF_{ble} mouse and b) a PF_{gen} mouse shows morphological differences in the region of consolidation within the lung. While in a) the consolidated regions seem rather homogeneously dense, in b) additional dense structures (most likely vessels) are clearly visible (red arrow head). Note: § indicates an air bubble in the paraffin block.

the different models could be obtained, an agglomerative clustering analysis was performed. In this case, the median value of the morphological parameters was taken, and each mouse was then represented by 6 features. A detailed description of this approach is presented in chapter 10. Figure 4.6 depicts the results of the analysis. On the right side of the plot, along the vertical direction, the values of histological scores used as a ground truth to evaluate the performances of the analysis are displayed. In figure 4.6 in the upper left corner, a blue rectangle was drawn to show that the surface area difference as well as the BV/TV are the parameters that group mice with lower fibrotic scores; whereas air volume, surface area, closed surface area body surface/body volume (BS/BV) allowing to gather mice with higher fibrotic scores. The parameters shown in figure 4.4b-h allow splitting the mice between fibrotic and healthy, but not in fibrotic subtypes such as bleomycin induced and the Nedd4-2 KO. The cluster map is capable to separate the mice groups, showing consistency with the histological scores, but still not able to perform a separation of the data in 3 cluster: controls, Nedd4-2 KO, and bleomycin induced mice.

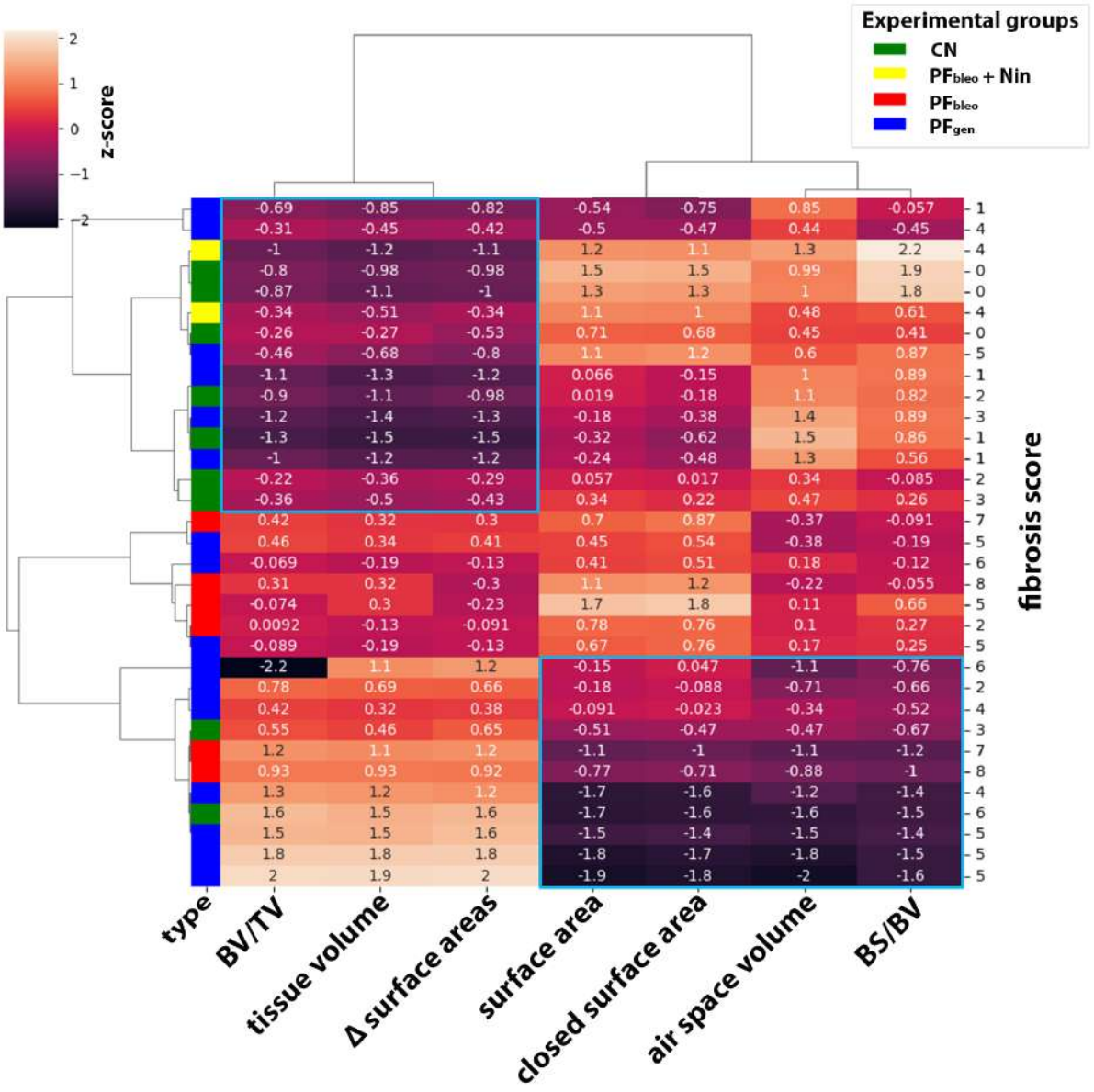

Figure 4.6: Agglomerative clustering of the morphological parameters measured with PBI micro-CT. The Ashcroft score was used as a label for comparison (right column). A clear separation between the mouse models was not possible, based solely on the parameters retrieved by the PBI micro-CT measurements.

Chapter 5

Histology and sample preparation

In this chapter, the sectioning protocol for the sample preparation for FTIR and AFM as well as the histological methods used to stain the lung tissue are presented.

5.1 Sample preparation: Cutting protocol

After the calculation of the depth of fibrotic regions in relation to the surface of the paraffin block by analysing the PBI micro-CT data sets, each paraffin block was cut targeting this position, using a microtome, at the University Medicine Gottingen (UMG). In the new developed tissue analysis pipeline after the cutting process, it was foreseen to perform FTIR, AFM, and SAXS. All the techniques required a spatial reference to identify sites of interest where the analysis had to be performed. Therefore, the cutting protocol was designed to always have a first slice of tissue to be used by classical histology, as reference, and an adjacent section to be measured with FTIR, AFM, and SAXS respectively.
The aim of these approaches was to perform different measurements as close as possible on the same section of the specimen, since fibrosis is not homogeneous and measuring the lung at different locations with the diverse methods would have lowered diagnostic value of their combination. This attempt to carry out this procedure of measuring the same region in the lung with different modalities is very challenging due to the different requirements in terms of sample preparation for each technique, which might be the reason why to my knowledge, such a combination has not been studied so far. Nevertheless, a cutting thickness of 5 m was selected to perform the analysis and kept the sections as close as possible together. It was possible to measure the same lung section with both FTIR and AFM, since a Calcium Fluoride (CaF_2) substrate was used to deposit the tissue. AFM is always coupled with an optical microscope to visualize the sample and where to measure; therefore, since CaF_2 is transparent to infrared (IR) light as well as to visible light, it allowed performing both the chemical and biomechanical characterization on the same portion of tissue. For SAXS the tissue was deposited over Capton. To summarize, two slices were cut for each measurement (FTIR/AFM and SAXS), one histology used as reference and one section to be measured. The cutting thickness was 5 µm for histology as well as for FTIR/AFM, whereas for SAXS it was 100 µm. Figure 5.1 depicts a schematic representation of the cutting protocol.

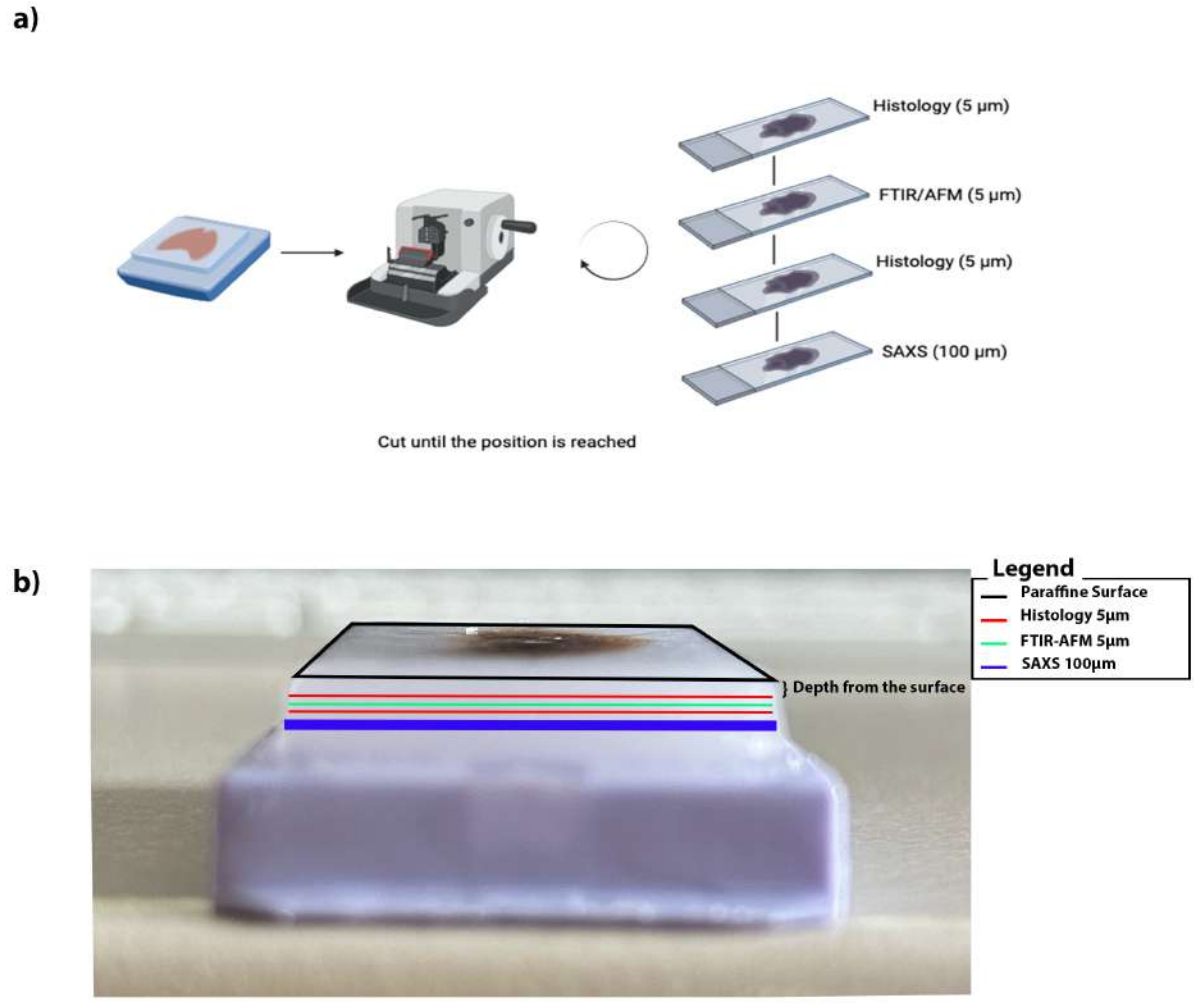

Figure 5.1: Schematic representation of the cutting process used for the sample preparation. The paraffin embedded lungs were cut with a microtome until the position (depth from the surface of the block) measured with the PBI, and then two subsequently slices were cut to get a histology for the spatial reference and the portion of tissue to measure with the multi-techinque pipeline.

In order to reference the depth of the ROI's with the calculations in the PBI-microCT data sets, the block was gently trimmed in the microtome until the first full section could be retrieved from the surface. This position was used as reference and all slices were done at the desired depths without dismounting the block again. Since the block is cooled during the cutting process and the PBI scans were taken at room temperature, an additional shrinkage needed to be considered. Based on previous experiments in the group at UMG Gttingen, 80% of the in PBI-microCT calculated depths were used. Figure 5.2 depicts the overlap between the histological slice and the whole 3D lung volume. This proves that a reduction of the initial position depth of the ROIs needs to be taken into account, as well as that the cutting protocol is consistent.

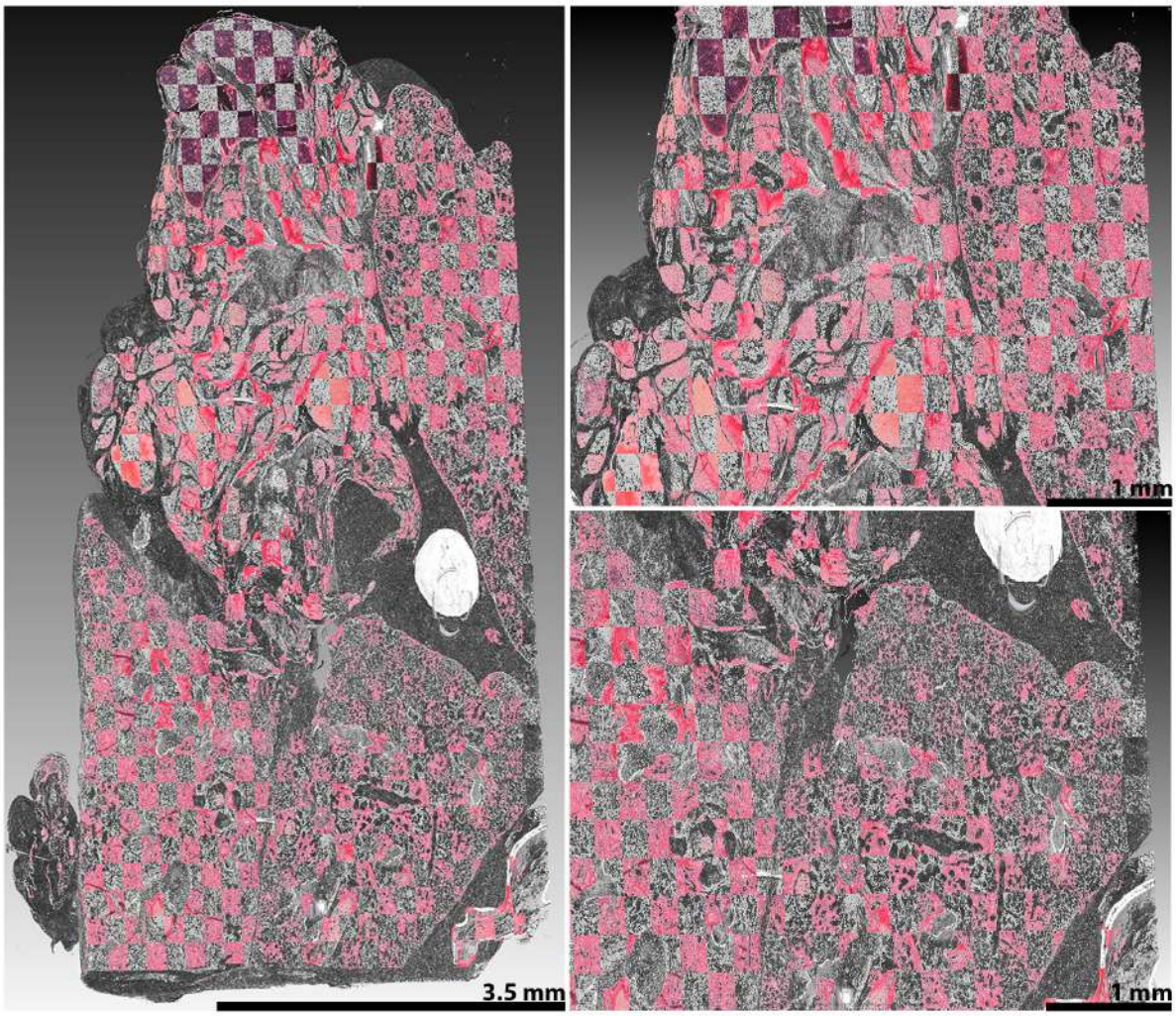

Figure 5.2: Overlap between the micro-CT data and the histology. This latter was taken at roughly 80 % of the depth measured during the PBI morphological analysis to take into account the shrinkage due to the cooling of the paraffin block before the microtome cutting. The check visualization allows showing the perfect match between the micro-CT data and the histology. On the right side, two magnification of the overlap.

As previously mentioned, for each technique two sections of tissue were obtained (one for reference, one for the real measurement), which resulted in a gap of 5 µm, between the data obtained by histology and FTIR/AFM. Figure 5.3 depicts a validation of the overlap between the histology and the slice used for the AFM measurement. The same portion of tissue underwent FTIR and AFM analysis, but since in the latter an additional optical microscope was used to localize the ROI's, it was used as an additional spatial reference of the data. Figure 5.3 demonstrates that despite there is a 5 µm gap between the histology and the slice measured with FTIR and AFM, the structural differences in the tissue morphology are barely detectable and still allowed an almost perfect overlap between them.

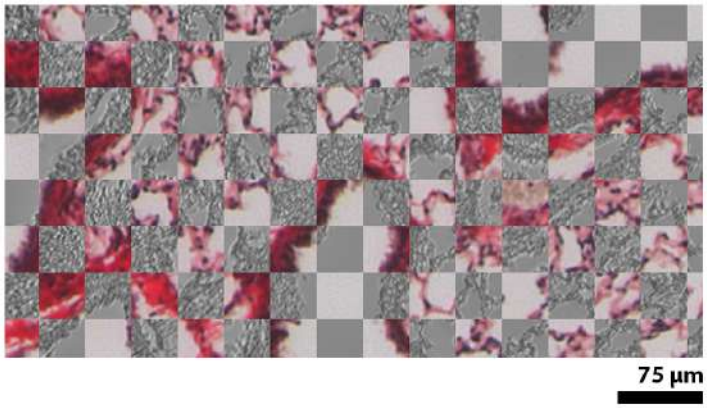

Figure 5.3: Overlap, using a check visualization, between histology and an optical image acquired with the AFM. The two images corresponds to 5 µm thickness slice cut one after the other. The overlap depicts that barely no morphological differences occur in this gap, and therefore the two portion of the tissue can be considered almost equal.

5.2 Result: Validating the severity of pulmonary fibrosis by means of histological analysis

The severity of pulmonary fibrosis (PF) was performed on all the lungs by visual scoring the histological lung section, according to the Ashcroft score [60]. This method is used to label the magnitude of fibrosis, but the scoring process is done on the bases of only the structural changes. The usual range, which was also used in this work, is from 0=healthy, figure 5.4a, up to 8=severe fibrosis, figure 5.4b.

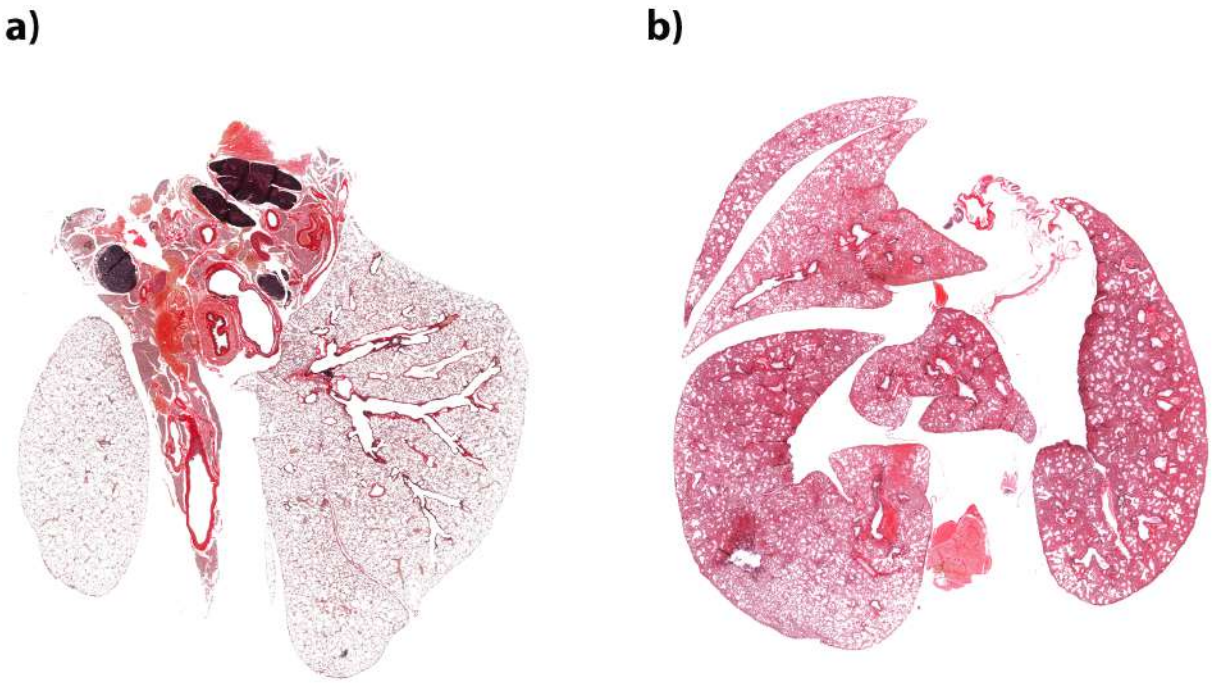

Figure 5.4: Example of two histological sections used in the Ashcroft score. a) Healthy control (Ashcroft score of 0). b) Severe fibrotic lung (Ashcroft score of 8).

The severity of PF was scored, choosing 3 randomly regions and giving them a value between 0 and 8. This was performed in a blinded way, where 3 independent researchers, had to score the lungs. Then the median value of all the regions and investigators was used as the severity score for each single lung. Figure 5.5 shows the result of the process. It can be observed that the bleomycin-induced pulmonary fibrosis (PF_{bleo}) had higher values compared to the Nedd4-2 knock out mode (PF_{gen}). The controls for the bleomycin-induced fibrosis model (CN_{bleo}) were all scored with 0, meaning perfectly healthy, whereas the controls for the KO model, received a higher score but still lower than the (PF_{gen}).

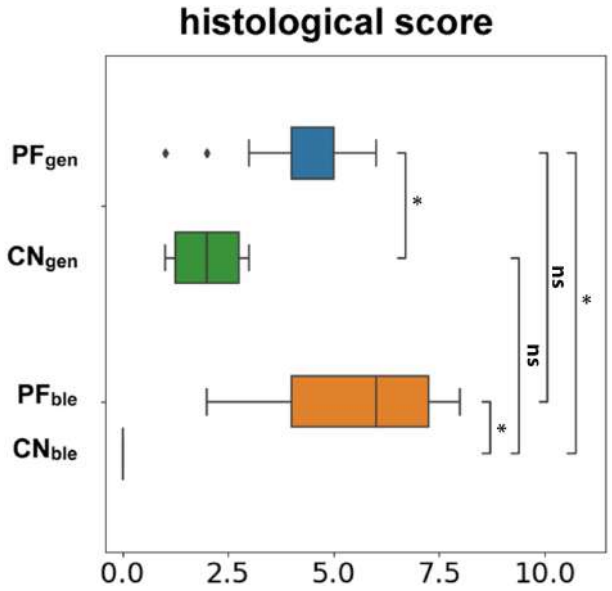

Figure 5.5: Result of the Ashcroft score. All the lung were scored in 3 randomly selected regions over the entire histological slice. The scoring range was between 0=healthy and 8=severe fibrosis. The box plots show that the PF_{bleo} had a higher score compared to the PF_{gen}. All the CN_{bleo} received a score of 0, while the CN_{bleo} had an average score of 2, which, however, was lower than PF_{gen}. Statistically significant differences were determined using the Mann-Whitney test with Bonferroni correction for multi-comparison: ns p $\leq$ 1.00, *p $\leq$ 0.05, **p $\leq$ 0.01, ***p $\leq$ 0.001, ****p $\leq$ 0.0001.

5.3 Histology

Histology concerns the examination of thin tissue's portions, properly stained and imaged with a microscope. Histological assessment of PF was performed on all lung specimens by visual scoring of the histological slices. To this end, three protocols to characterize the fibrotic regions within the lungs were used: Haematoxylin and eosin (H&E), Masson's trichrome, and Picrosirius red.

5.3.1 Material and Methods

5.3.1.1 Fixation and paraffin embedding process

Excised lungs were inflated with approximately 1 ml formalin (4% PFA) and then placed in formalin for 24 hrs. The lungs from the Nedd4-2 model which were stored frozen were defrosted and

then processed in the same way. Following the fixation process, the specimens were chemically dried using the followning protocol:

- 3x 60 min 75% Ethanol
- 2x 90 min 96% Ethanol
- 3x 75 min 100% Ethanol
- 2x 120 min Xylol

After that the specimens were automatically transferred in approximately 60 °C warm paraffin and kept there till the final embedding in paraffin blocks. It needs to be mentioned that the frozen Nedd4-2 lung specimens as well as the corresponding control lungs did show the onset of autolysis, most likely due to the considerable long post-mortem microCT acquisitions (briefly mentioned in chapter 3) which were performed in-situ without fixation of the tissue.

5.3.1.2 Histological sectioning and deparaffinization

Paraffin blocks were cooled on a cooling plate, mounted in a standard rotary microtome and sectioned to thicknesses between 5 and 100 µm (for more details refer to section 5.1). The slices for histological analysis were transferred to glass objective slides in a water bath. The slides were then left to try overnight. Since the paraffin is only used to provide a ridged matrix for the cutting process and hinders the staining to penetrate the tissue, it needs to be removed. To this end, the following protocol was applied.

- heating to 60 °C for 30 mins in an incubator
- 2x 7 min Xylol
- 5 min Isopropanol
- 5 min 98% Ethanol
- 5 min 75% Ethanol
- 5 min 60% Ethanol
- 5 min demineralized water

5.3.1.3 Haematoxylin and eosin (H&E)

Haematoxylin and eosin (H&E) is the most widely used staining protocol in medical diagnosis [61]. The haematoxylin stains the cell nuclei in a purplish blue colour, while eosin stains the extracellular matrix and cytoplasm in pink. All the other structures receive different shades and combinations of these colours [62]. H&E staining was performed using the following protocol.

- 5 min in haematoxylin solution
- rinsed with demineralized water
- 5 min eosin solution
- rinsed with menineralized water

5.3.1.4 Masson's trichrome

Masson's trichrome is a three-colour staining procedure used in histology. This method is well suited for distinguishing cells from surrounding connective tissue. The fixed sample is immersed into Weigert's iron haematoxylin, and then three different solutions, labelled A, B, and C:

- Weigert's haematoxylin is a sequence of three solutions: ferric chloride in diluted hydrochloric acid, haematoxylin in 95% ethanol, and potassium ferricyanide solution alkalized by sodium borate. It is used to stain the nuclei.
- Solution A, also called plasma stain, contains acid fuchsin, Xylidine Ponceau, glacial acetic acid, and distilled water. Other red acid dyes can be used, e.g. the Biebrich scarlet in Lillie's trichrome.
- Solution B contains phosphomolybdic acid in distilled water.
- Solution C, also called fibre stain, contains Light Green SF yellowish, or alternatively Fast Green FCF. It is used to stain collagen. If blue is preferred to green, methyl blue or water blue can be substituted.

5.3.1.5 Picrosirius Red

Picrosirius Red is a simple and sensitive method, introduced by Junqueira et al. [63], that identifies fibrillar collagen networks in tissue sections. Under polarized light, this staining has been used to identify different types of collagen [64]. For example, yellow-red birefringence would be associated to collagen type I, whereas collagen type III would display a weak birefringence associated with a greenish colour. The staining procedure is the following:

- Deparaffinize and hydrate to distilled water
- Place in solution A for 2 minutes
- Rinse in distilled water
- Place in solution B for 60 minutes
- Place in solution C for 2 minutes
- 70% Ethanol for 45 seconds
- Dehydrate, clear and mount

Where:

- Solution A is Phosphomolybdic Acid
- Solution B is Picrosirius Red F3BA Stain
- Solution C is 0.1 N Hydrochloride Acid

5.3.1.6 Final preparation prior microscopy

In order to fix the slides in a way that they can be imaged by microscopy and that they also can get stored, a few additional steps are needed after the respective staining was performed.

- briefly rinse with destilled water
- briefly put in 60% Ethanol
- briefly put in 70% Ethanol
- 5 min in 90% Ethanol
- 5 min Isopropanol
- 2x 5 min Xylol
- sealing with water-free permanent deck solution under a cover slip

5.3.2 Results: Staining protocols

The usage of H&E allowed me to distinguish between healthy and fibrotic lungs, but without showing the deposition of connective tissue, such as collagen. The characterization in H&E is solely based on the apparent structural modifications of the lung tissue in the fibrotic animals. Figure 5.6a is an example of a fibrotic lung, where it is easy to identify the fibrotic regions as they appear more dense and darker.
The lack of the H&E for the connective tissue labelling was the reason behind the Masson's trichrome staining (MTS) application. MTS is more suited to highlight the regions comprising collagen. Figure 5.6b clearly shows that the perivascular regions, which are rich in collagen, are labelled in blue. This allowed a first identification of areas that showed an accumulation of connective tissue as a consequence of fibrosis. Nevertheless, this was still insufficient, as in the lungs both collagen I and collagen III are present, and the Masson's trichrome staining is not capable of labelling them differently. Therefore, we decided to use the Picrosirius Red staining, which allows identifying fibrillar collagen networks in the tissue sections. Figure 5.6c shows a histology of a lung, where the collagen deposition regions are labelled in red. This staining alone is not so different from the Masson's trichrome staining, but when coupled with a polarization filter, collagen I and collagen III are coloured in yellow and green, respectively, and thus are distinguishable (figure 5.6d).

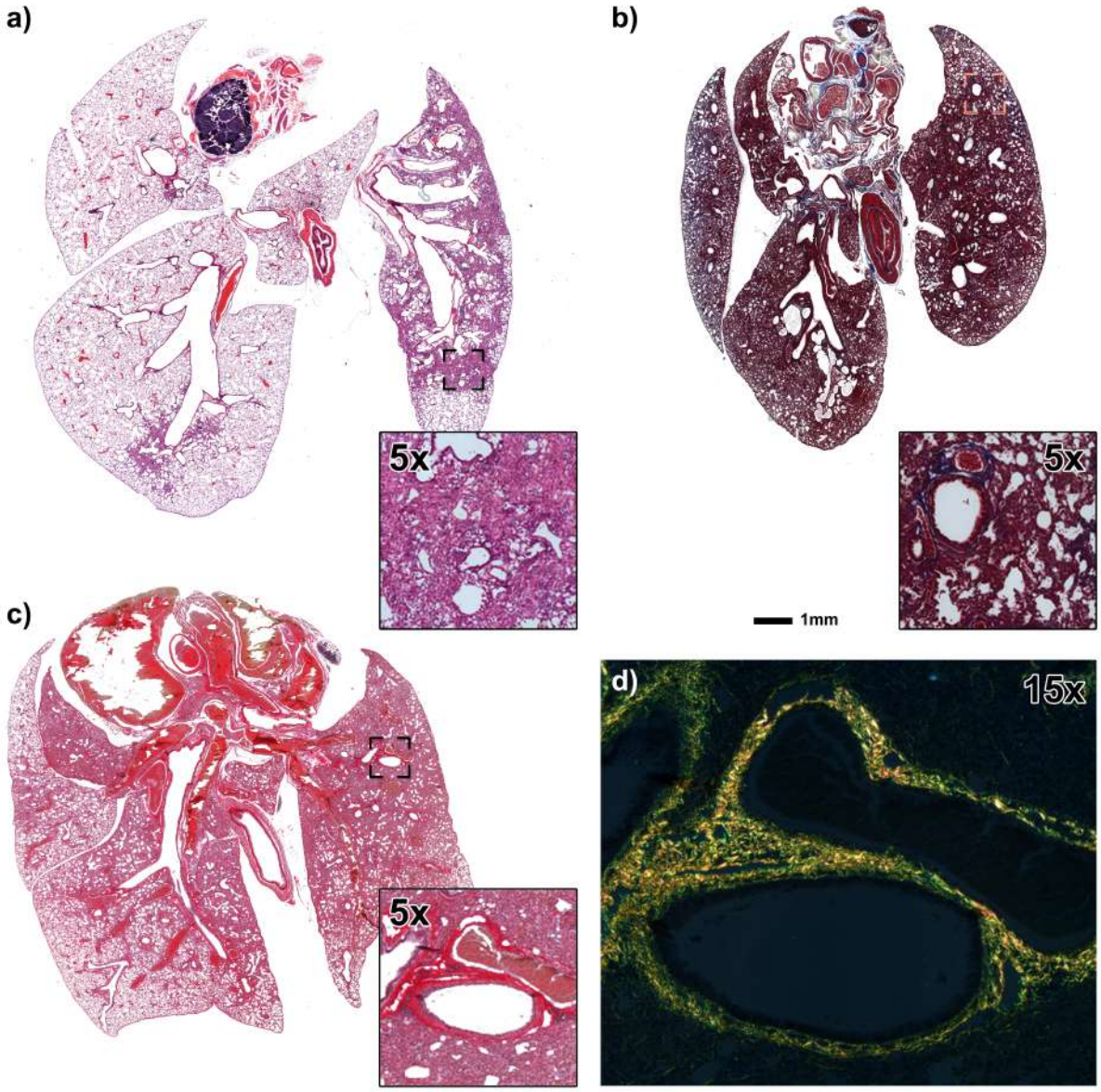

Figure 5.6: Examples of different histological stainings. a)Haematoxylin and eosin (H&E) staining. The magnified region shows an example of tissue consolidation. b)Masson's trichrome staining. In the magnification, the collagen around the blood vessel is coloured in blue, whereas the lung tissue results in more brownish red. c)Picrosirius Red staining. The collagen deposition in the perivascular regions results coloured in red. d)Picrosirius Red staining coupled with a polarization filter. The pairing of these allows the identification of different types of collagen, in particular collagen I result yellow whereas the collagen III is green.

Chapter 6

Fourier-Transform Infrared Spectroscopy (FTIR)

In this chapter, the Fourier-Transform Infrared Spectroscopy (FTIR) measurements and analysis is presented.

6.1 FTIR setup at SISSI Beamline

The SISSI (Synchrotron Infrared Source for Spectroscopy and Imaging) beamline collects the light from bending magnet 9.1 at the Elettra Synchrotron facility. It is divided into three endstations (figure 6.1a), SISSI Biochemical and Life Sciences (SISSI-Bio) managed by Elettra Sincrotrone Trieste, SISSI Material Sciences (SISSI-Mat) operated by IOM-CNR, and SISSI-Nano, co-managed.

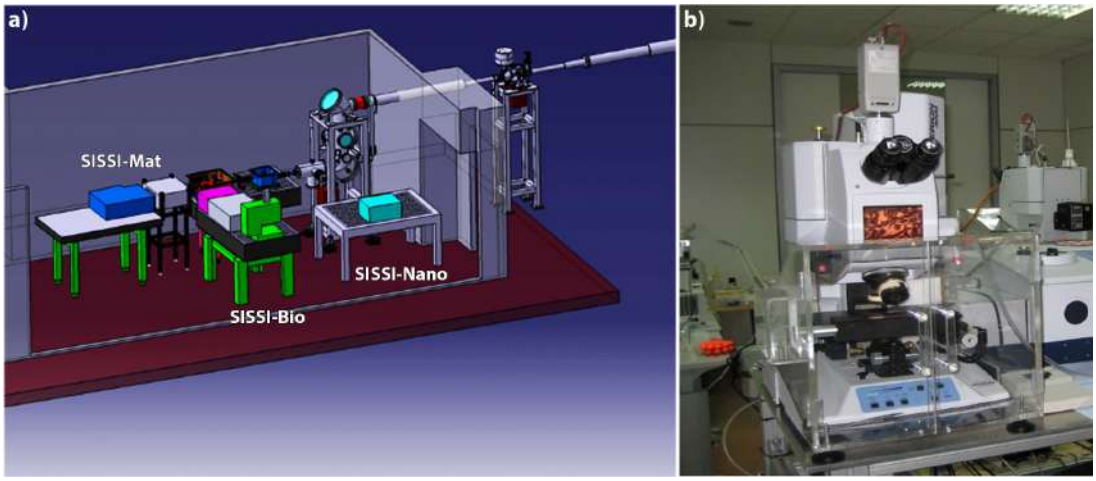

Figure 6.1: SISSI (Synchrotron Infrared Source for Spectroscopy and Imaging) beamline. a) Schematic representation of the three endstations: SISSI Biochemical and Life Sciences (SISSI-Bio), SISSI Material Sciences (SISSI-Mat), and SISSI-Nano. b) Set-up of SISSI-Bio endstations which comprises a Bruker Hyperion 3000 VIS/IR microscope, coupled to a VERTEX 70V in vacuum interferometer and equipped with both single point MCT (mercury cadmium telluride) detector for spectroscopy and a 64x64 pixel FPA (Focal Plane Array) detector full field for hyperspectral imaging.

The experiments for this PhD thesis were performed at the SISSI-Bio branchline, using a Bruker Hyperion 3000 VIS/IR microscope, coupled to a VERTEX 70V in vacuum interferometer and equipped with both single point MCT (mercury cadmium telluride) detector for spectroscopy and a 64 x 64 pixel FPA (Focal Plane Array) detector full field for hyperspectral imaging, figure 6.1b. The microscope optics are a pair of 15X cassegrain objective/condenser to allow for transmission experiments. The selected objective grants a detector projected pixel size of 2.6 µm x 2.6 µm. FTIR imaging was selected because it allows collecting large areas in few hours at high resolution. On the contrary mapping the sample by raster scanning, even with a brilliant source as synchrotron, would have taken days.

6.2 Material and Method

6.2.1 FTIR

A preliminary pilot test was performed to optimize cutting thickness of the FFPE lungs and support material. At first, the impact of the cutting thickness on the measurement was evaluated. The aim was to use the thinnest section possible while still achieving a reasonable S/N. To this end, 5 µm and 10 µm slices deposited on a Silica substrate were then tested. The measurements were performed in reflection mode, since Si is not transparent to IR. Figure 6.2 depicts the results. A dashed line was used to highlight the absorbance at the Amide I peak (1650 cm^{-1}). The spectra, for both thicknesses, showed clear defined peaks, in the whole spectral range (4000-800 cm^{-1}) can be seen without a huge contribution of background noise. Therefore, to keep the tissue section as thin as possible, 5 µm was chosen as the cutting thickness.

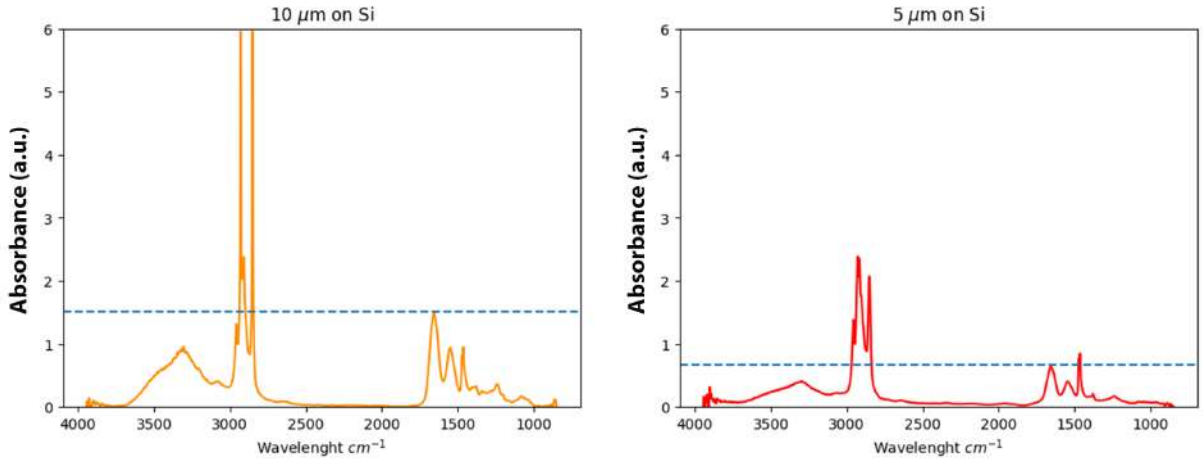

Figure 6.2: Example of two spectra acquired at the SISSI beamline in reflection mode for two lung sections with a thickness of 10 µ (left) and 5 µm (right) deposited on a substrate of Silica. In both plots, a blue dashed line is used to measure the absorbance of the Amide I peak (1650 cm^{-1}).

Subsequently, different substrates, such as Silica, glass coated with Indium Tin Oxide (ITO), and Calcium Fluoride (CaF_2) were tested. The measurements using Silica were performed in reflection and resulted, as shown in figure 6.2, in smooth spectra in which all the peaks are clearly defined. However, since the multitechnique pipeline was meant to measure the same

portion of tissue, Silica was not suited for this purpose. Indeed, the next technique of the multimodal approach was AFM, which requires as substrate a material that is transparent to visible light. This is due to the fact that the AFM is placed above the sample, which is visualized in parallel using an inverted optical microscope below. The second substrate tested was a glass coated with 100 nm layer of Indium Tin Oxide (ITO). Glass, as Silica, is not transparent to IR light, thus also here the operation mode for the FTIR was reflection. However, since the layer of ITO was very thin, the glass was still transparent to visible light, and thus suitable for the next AFM measurements. Unfortunately, as shown in figure 6.3, the identification of the peaks of the spectra was not possible due to a superimposition of fringes over the IR signal. Fringes are a non-chemical interference pattern that can be the result of reflections inside the sample or the sample holder, or between the sample and the sample holder. The last substrate

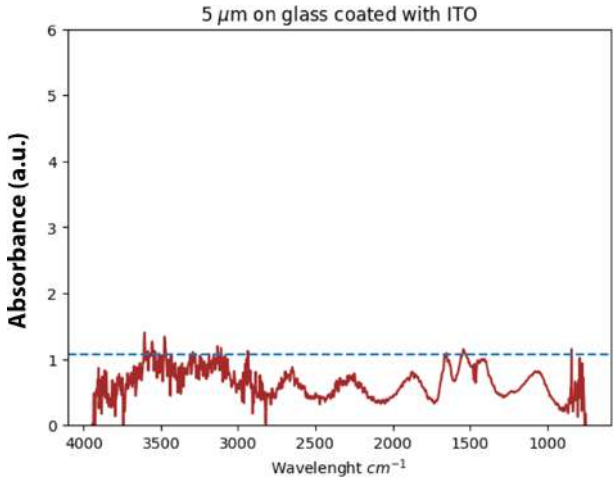

Figure 6.3: Example of a spectrum acquired at the SISSI beamline in reflection mode for a lung section with a thickness of 5µm deposited over a glass coated with Indium Tin Oxide (ITO). It can be seen that in the spectrum there is a superimposition of fringes, which makes impossible to detect the peaks in the spectral range (4000-800 cm^{-1}).

tested was Calcium Fluoride (CaF_2), which is a material transparent to both IR and visible light. The operation mode for the FTIR measurement was transmission. Figure 6.4 shows the comparison of the spectra between two slices with a thickness of 5 µm, deposited on Silica and CaF_2, respectively. It can be seen that in both the measurements there is only slight contribution of background noise, resulting in a clear identification of all the peaks within the spectral range (4000-800 cm^{-1}). To compare if there were any differences in terms of absorption, between the two modalities, the absorption at the Amide I peak was selected as a comparison metric. As shown in figure 6.4 by means of the blue dashed line, in both the measurements (reflection and transmission), the absorbance at the Amide I was equal. Therefore, the substrate of CaF_2 was chosen, allowing to measure the same portion of tissue with both FTIR and AFM instrumentation.

6.2.2 Identification of collagen subtypes

The histological slice, taken 5 µm above the one measured with FTIR, was used as reference map for the identification of the perivascular region (areas around the blood vessels where the

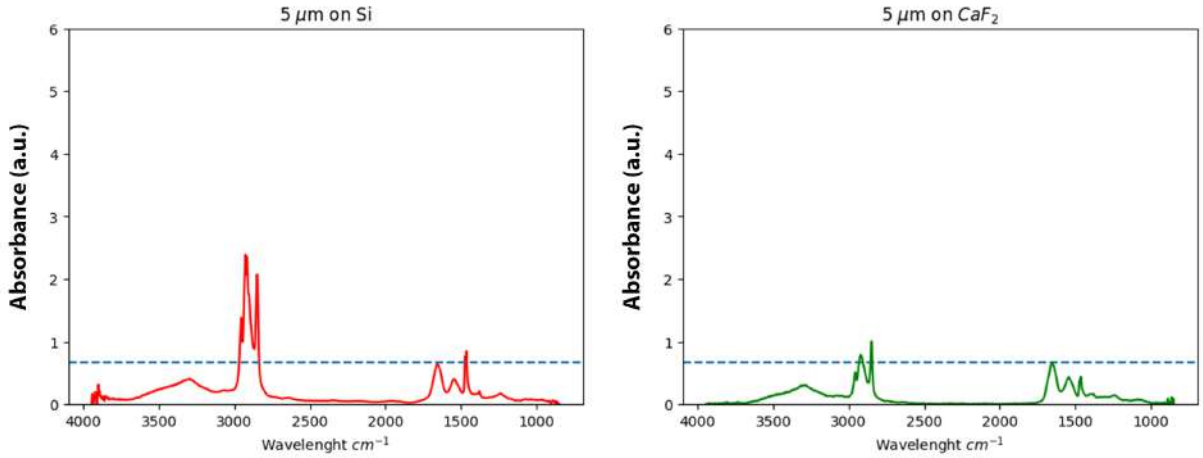

Figure 6.4: Comparison of the IR signal acquired at the SISSI beamline. On the left, the spectrum of a 5 µm thickness lung slice deposited over Silica, acquired in reflection mode. On the right, the spectrum of a lung slice of the same thickness, deposited on Calcium Fluoride, and measured in transmission mode. A blue dashed line is used to indicate the absorption at the Amide I peak (1650 cm^{-1}). The absorbance at this wavelength is used to detect differences between the two modalities.

collagen deposition occurs). After the acquisition, all the spectra underwent a pre-processing protocol:

1 Rubber-band baseline correction.

2 Clipping to spectral range between 1800-800 cm^{-1}.

3 Separation between lung tissue and background (paraffin) applying a thresholding at the Amide I peak.

4 The second derivative of the spectra was calculated applying a SavitzkyGolay filter, with a window width of 21, polynomial order of 3, and derivative order of 2.

5 Perform a zero mean normalization of the second derivative obtained at the step 4.

Furthermore, the spectra of pure collagen I and III, as well as mixtures with different ratios between them (1:1,1:2,1:3,2:1,3:1) were measured. These spectra underwent the same preprocessing, excluding step 3. Principal Component Analysis (PCA) was run on all collagen spectra. PCA transforms the data into a new orthogonal coordinate system, in which the axes, called Principal Components (PC) axes, represent the directions with the highest variation of the data. Principal Component 1 (PC1) represents the highest variation of the data along one dimension. The new PC axes are based on the linear combination of the spectral components, which are called loadings of the axes. Figure 6.5 shows the collagen I, collagen III, and their mixture along PC1. It can be seen that pure collagen I and collagen III showed the lowest and highest values, respectively, along the PC1, while their solution 1:1 was in the middle between these two values. Furthermore, the other different solution are, as the amount of one collagen gets predominant to the other, closer to the pure predominant one.

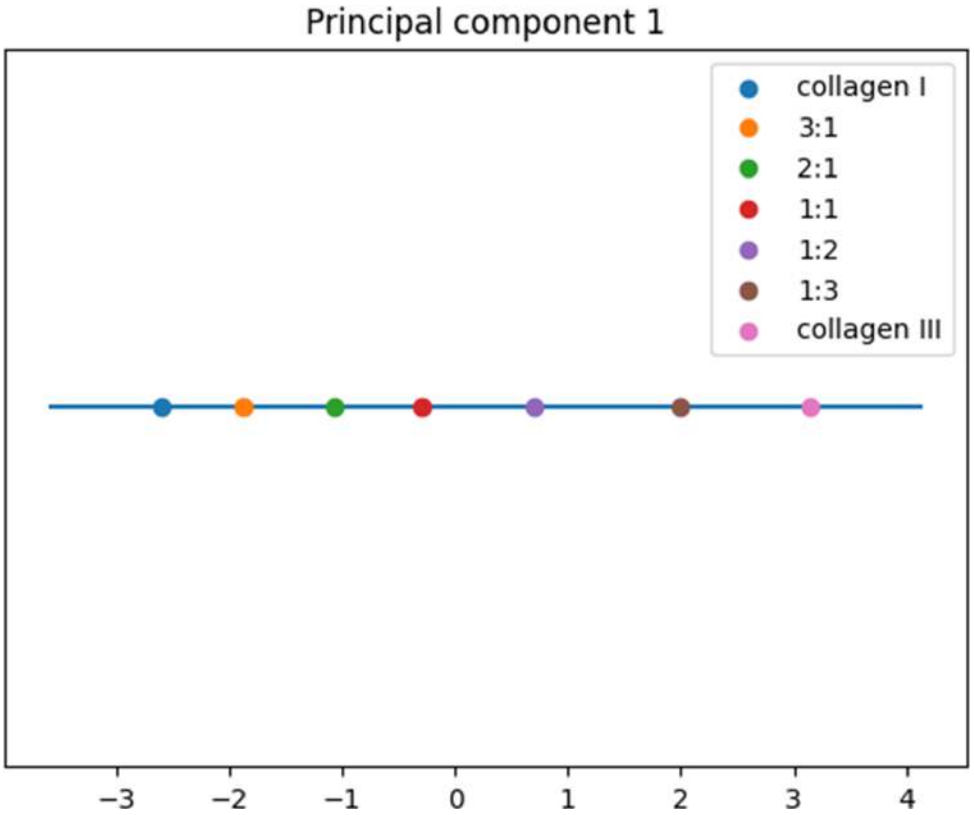

Figure 6.5: Distribution of the pure collagen I, pure collagen III, and solutions with different amount of them (1:1,1:2,1:3,2:1,3:1), along PC1. The pure collagen I and III show the lowest and highest value along PC1, respectively. The solution 1:1 is in the middle, while the other different solution are, as one type of collagen becomes predominant, closer to the pure predominant one.

The next step was to perform a feature selection on the loading of PC1. From the plot of the loadings, only the wavelengths of the ones with an absolute loading value above 0.1 were selected. The magnitude of a peak can be thought as indicative of the degree to which that particular infrared absorption influenced the spread of the scores plot: the largest peaks/troughs caused the most variance [65]. Therefore, these wavelengths are those that vary the most between collagen I and III. This allowed reducing the dimensionality of the spectra from 453 to 31 components (wavelengths), figure 6.6.

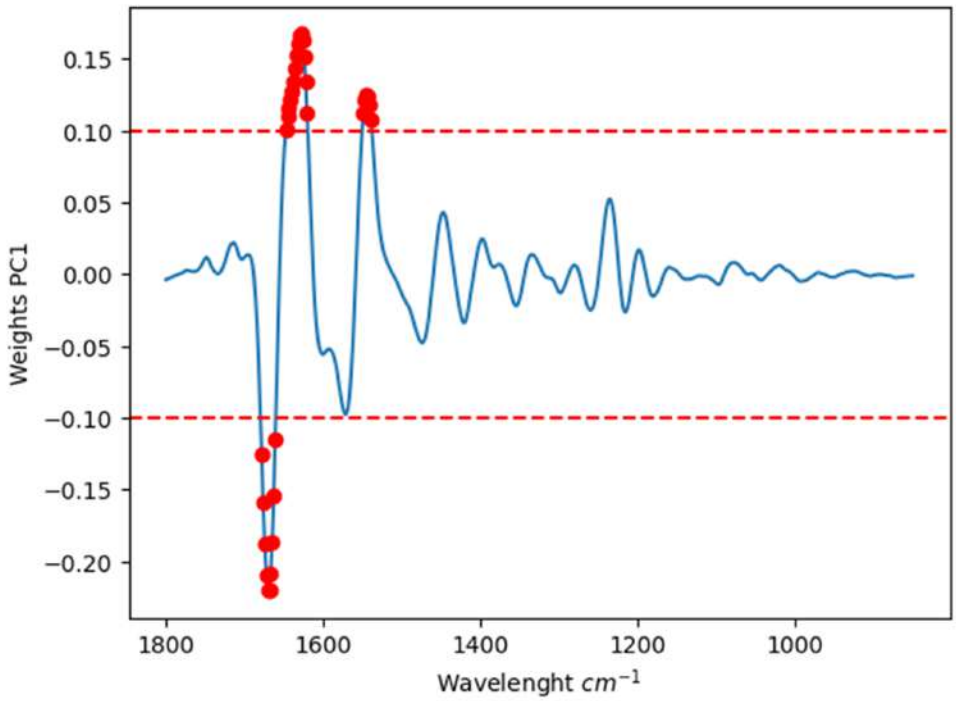

Figure 6.6: Plot of the weights of PC1 of the principal component analysis used to split the pure collagen I, pure collagen III, and solutions with different amount of them (1:1,1:2,1:3,2:1,3:1). The red dashed lines indicate the threshold above which the weight was considered, and the red scatters represent the weights selected.

A K-Means clustering was then run to measure the collagen I and III content in the perivascular regions of the lungs. In the algorithm two clusters, equal to the number of collagen types, were selected, and the centroids were initialized with the values of the two pure collagen measurements. Figure 6.7a and b show the results of the K-Means clustering for a PF_{ble} and an CN, respectively, in which the pixels representing collagen I and collagen III are labelled in yellow and green, respectively. For a visual validation of the clustering results, the histological slice used as reference map for the FTIR was imaged coupling a light microscopy with a polarization filter. Figure 6.7c depicts the result. The orange structures point to a higher accumulation of collagen I whereas the green structure indicates a predominance of collagen III. An overlap between the K-Means clustering and the histology imaged with a polarization filter was performed for a visual validation of the clustering approach. Figure 6.7d depicts the results, showing a high degree of correlation between the two images.

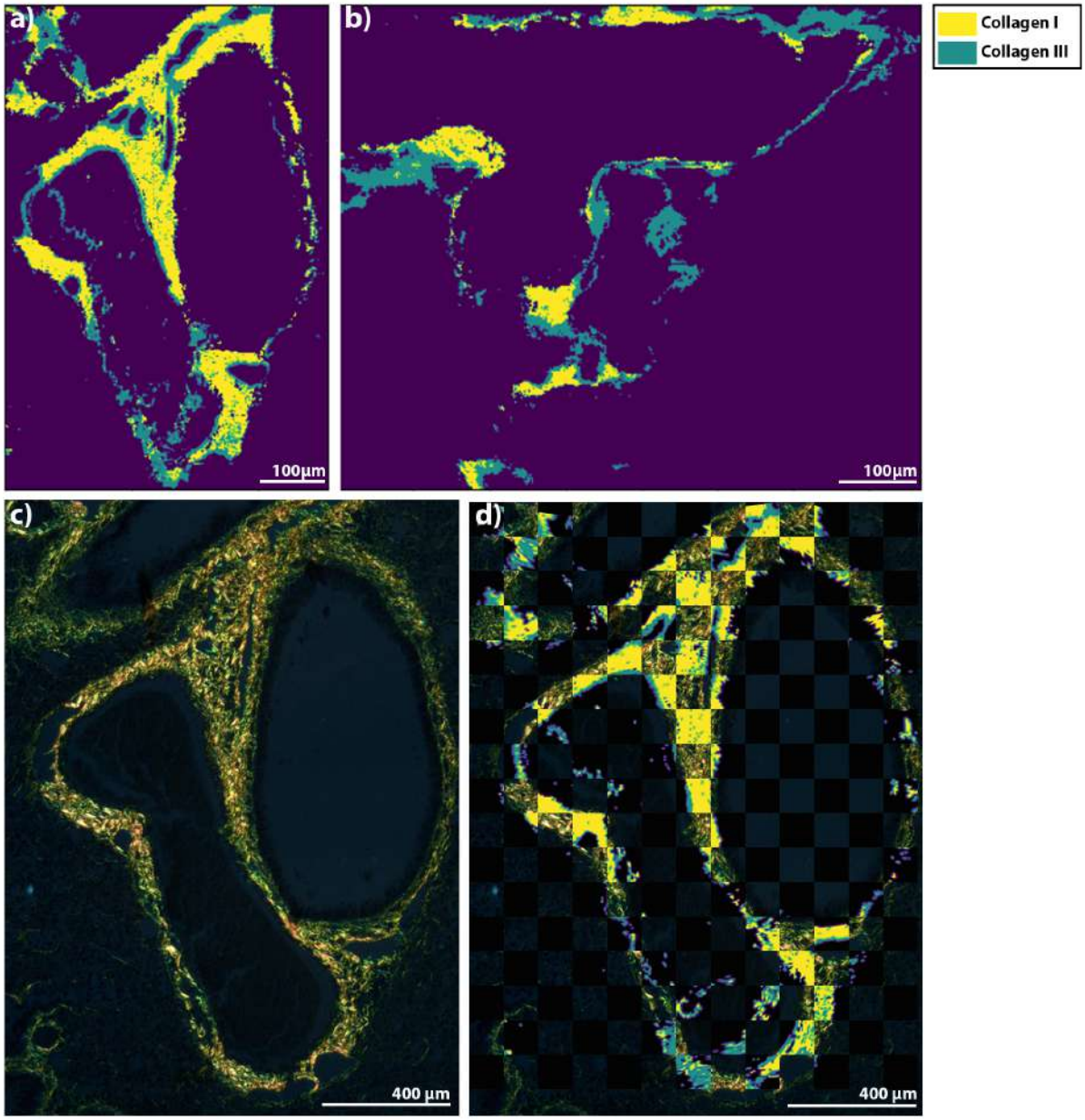

Figure 6.7: Quantification of collagen I and III content. a)-b) K-Means clustering results of the collagen content in a PF_{ble} and in a CN_{ble}, respectively. c) Picrosirus stained lung sections imaged with polarized light of the same PF_{ble} shown in a). d) Overlap of the Picrosirus stained lung sections imaged with polarized light and the K-Means clustering map for collagen I and III.

6.3 Results: Collagen content in the perivascular regions of fibrotic lungs, revealed by K-Means clustering

A total of 27 lungs, 3 CN_{ble}, 8 PF_{ble}, 4 CN_{gen}, and 12 PF_{gen}, underwent the K-Means clustering analysis for the quantification of collagen I and III in the perivascular regions. Figure 6.7a and b show the results for a PF_{ble} and a CN_{ble}, respectively. It can be seen that there are differences in the collagen I and III content in the two examples. In particularly, the healthy control showed a predominance of collagen III, in respect to collagen I, while in the fibrotic mice collagen

I content was higher. The metric extracted from the FTIR measurements was the relative collagen I content, which was calculated dividing the amount of pixels labelled as collagen I, from the K-Means analysis, and the sum of the pixels classified as collagen I plus collagen III. Box plot representation was used, as shown in figure 6.8, to represent the results of the analysis. It can be seen that there are statistically significant differences between PF_{ble} and PF_{gen}. It can be noticed that the CN_{ble} showed lower value for the relative collagen I content, compared to the CN_{gen}, meaning the both the experimental groups (controls + fibrotic mice) are different. It appears that such differences, shown in 6.8, are more likely due to the mice themselves, e.g. age of the mice, quality of the lung, rather than the fibrosis. Nevertheless, even if it is not statistically significant, it can be noticed that the median relative collagen I content between the CN_{ble} and PF_{ble} was more similar than in the case of CN_{gen} and PF_{gen}.

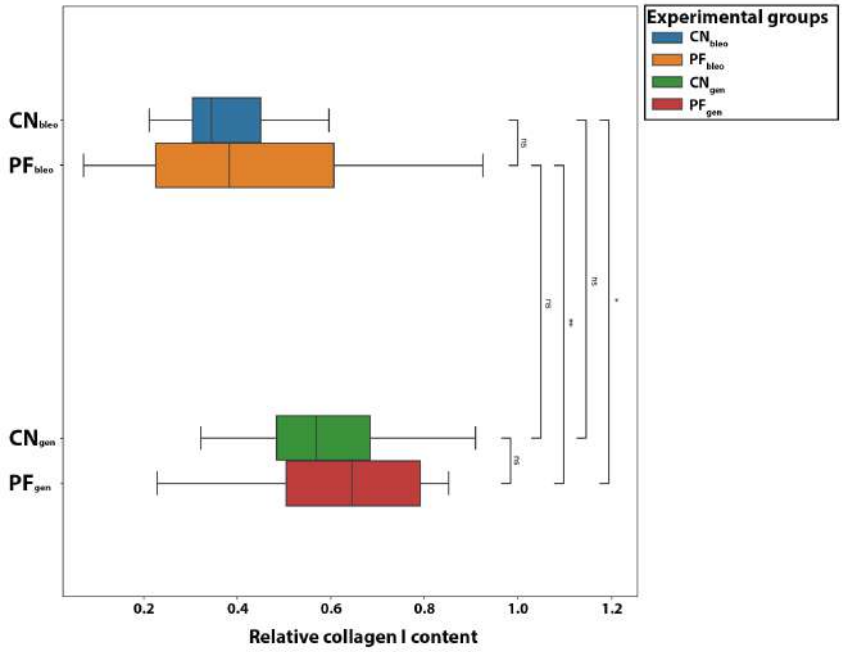

Figure 6.8: Results of the collagen I and III analysis in the perivascular regions of mouse lung tissue. For each model 3, 8, 4,12 numbers of animals for CN_{bleo} , PF_{ble}, CN_{gen}, PF_{gen}, respectively, were measured. Statistically significant differences were determined using the Mann-Whitney test with Bonferroni correction for multi-comparison: ns p $\leq$ 1.00, *p <= 0.05, **p <= 0.01, ***p <= 0.001, ****p <= 0.0001.

Chapter 7

Atomic Force Microscopy

In this chapter, the set-up, the sample preparation, and the analysis of the Atomic Force Microscopy (AFM) are presented.

7.1 Sample Preparation

For all the FFPE lung tissue, a targeted slice with a thickness of 5 µm was cut subsequently to the one used for the histology and deposited on a Calcium Fluoride (CaF_2) substrate. To perform the biomechanical characterization of the lungs, the embedding medium needed to be removed and the tissue re-hydrated. The following protocol was applied: 1 hour in the oven at 65, 15 minutes in Xylol, a rinse in fresh Xylol, 10 minutes in Ethanol 99%, 10 minutes in Ethanol 96%, 5 minutes in Ethanol 50%, and finally transferred to water for the measurement.

7.2 Material and Methods

7.2.1 AFM set-up

The AFM measurements were carried out at Georg-August-University Göttingen, Institute for X-Ray Physics with Nanowizard 4 (JPK, Bruker Nano GmbH, Berlin, Germany), on an inverted light microscope (IX73; Olympus, Tokyo, Japan) with a 20x Objective (LUCPlanFLN, NA=0.45, Olympus) in force spectroscopy mode, with a set point of 10 nN, Z speed of 2 µm/s using a pre-calibrated cantilever (SiO_2) with a spring constant of 0.062 N/m and a bead of 2.5 µm diameter (Novascan Technologies, US). All measurements were performed in water. JPK Data Preprocessing software (version 7.0.165, Bruker Nano GmbH, Berlin, Germany) was used to retrieve the Young's moduli. For all the force curves, a baseline subtraction and contact point determination were applied before performing the elasticity fit of the curve.

7.2.2 Software

The pre-processing of all force curves as well as the Young's moduli calculation was performed using JPK Data Preprocessing software (version 7.0.165, Bruker Nano GmbH, Berlin, Germany). A Python script was used to overlap the position of the force curves and the online acquired microscopic images.

7.2.3 Biomechanical characterization of de-paraffinized and re-hydrated paraffin embedded lung tissue sections

A histological lung section, stained with picrosirius red, taken 5 µm above the one measured with the AFM, was used as a reference map for the identification of the ROIs in the tissue. For this analysis, three areas, per sample of PF_{gen} and PF_{ble} were selected: perivascular regions (collagen deposition), lung parenchyma, and areas of tissue consolidations; whereas for CN mice only the first two ROIs were measured, since no tissue consolidation was present. The same ROIs identified in the histological slice were easily detectable in the section of tissue measured with the AFM, since the distance between them was only 5 µm. For each selected area within the lung, at least 35 force curves were measured. All the data underwent a pre-processing using JPK Data Preprocessing software (version 7.0.165, Bruker Nano GmbH, Berlin, Germany) consisting of a baseline subtraction and contact point determination. Subsequently, an elasticity fit, which applies the Hertz fit (see chapter 2) to the force curves, was performed and the Young's moduli were retrieved.

7.3 Results

Figure 7.1a and b depicts the positioning of the force curves collected with the AFM on the online acquired microscopic images of the lung. Figure 7.1 a) and b) shows a region of parenchymal tissue and a perivascular fibre deposition for a lung of the control group, respectively. To provide a visual representation of the stiffness of the lungs, the Young's moduli were represented in a 3D bar plot, figure 7.1c). Figure 7.1d) demonstrates that there is a stiffening of the tissue in the fibrotic lungs. Furthermore, among the two mouse model, the PF_{gen} one showed the highest value for the Young's moduli. Interestingly, all the regions measured with the AFM demonstrated elevated stiffness, for both PF_{gen} and PF_{ble}. The controls of the two mouse models (CN_{gen} and CN_{ble}) were condensed into one single group, as they showed pretty low variation. Based on the similarity of the Young's moduli in the control groups, it is unlikely that the increment in stiffness in the fibrotic mice was a consequence of differences in the sample preparation rather than related to the presence of fibrosis. It can be seen that the increment in the Young's moduli is not local, e.g. just in the perivascular region, but that it occurred in the whole lung.

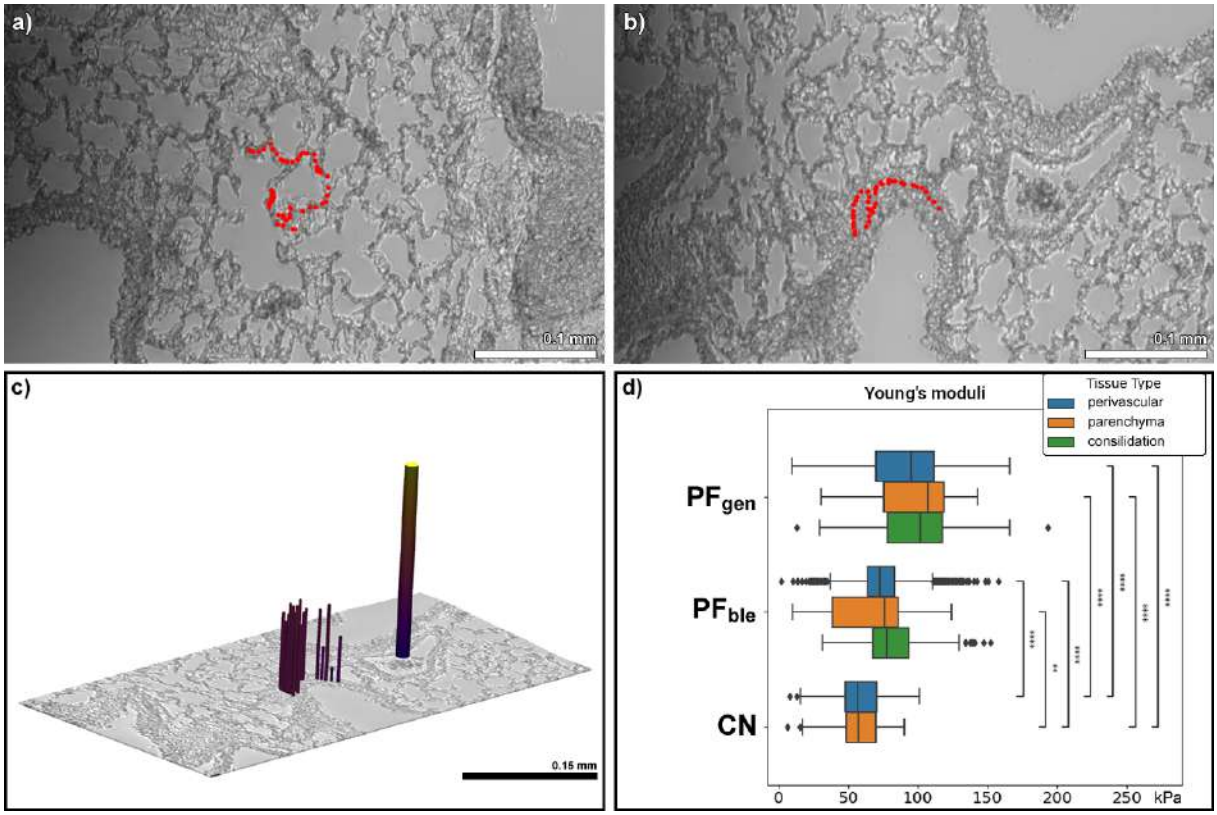

Figure 7.1: AFM measurements. a) and b) show two example position of the force curves (red dots) for lung parenchyma and an area of perivascular fibre deposition in a CN lung, respectively. c) shows the obtained Young's moduli were then mapped into 3D bar plots to allow rendering it into the 3D context of the CT data. d) shows the results of the force curve measurements. The controls of the two mouse models (CN_{gen} and CN_{ble}) were condensed into one single group. For each model 3, 5, 8 numbers of animals for PF_{gen}, PF_{ble} and CN respectively, were measured. Statistically significant differences were determined using the Mann-Whitney test with Bonferroni correction for multi-comparison: ns p $\leq$ 1.00, *p <= 0.05, **p <= 0.01, ***p <= 0.001, ****p <= 0.0001. Note: since no consolidated area was present in CN group, no value was included for that particular ROI. Clearly, PF_{gen} shows the highest Young's modulus, followed by PF_{ble}. Interestingly, an elevated stiffness can be found in all three ROI's without major differences.

Chapter 8

SAXS

In this chapter, the set-up, the sample preparation, and the analysis of the small-angle X-Rays scattering (SAXS) data for two mice of the two fibrotic models are presented.

8.1 Sample preparation

For all the paraffin embedded lung tissue specimens, a slice of 5 µm was cut adjacent to the one measured with FTIR and AFM, stained with picrosirius red and used as a reference for the SAXS measurements. A 100 µm thick slice was cut subsequently and deposited over a piece of Kapton tape. A specific holder was designed and 3D printed to store the sample, figure 8.1b.

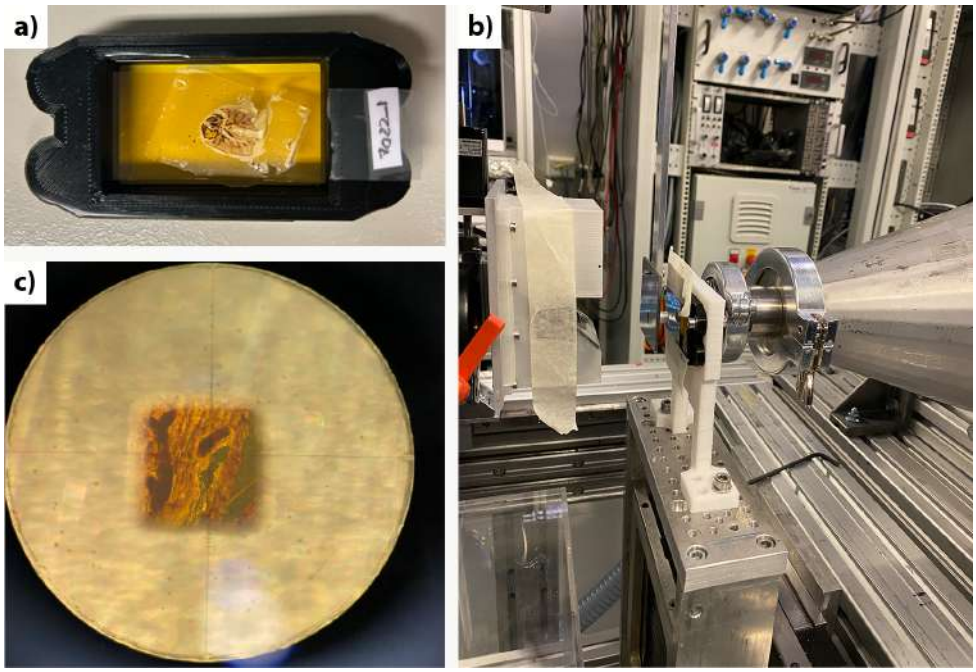

Figure 8.1: Set-up for imaging of FFPE lung at the Austrian SAXS beamline of Elettra. a) 3D printed sample holder for FFPE deposited on Kapton. b) Example of a ROI selection for the SAXS measurements. c) Set-up of SAXS measurements for FFPE lung tissue

8.2 Material and methods

All the SAXS measurements were carried out at the Austrian SAXS beamline at Elettra, Trieste [66], using a Pilatus 3 1M detector (DECT RIS Ltd. Taefernweg 1, 5405 Baden-Daettwil Switzerland) with a sample-to-detector distance of 1.4 meters and a beam energy of 8 keV. Figure 8.1b depicts the experimental set-up. Before each measurement, a metal plate with a window (2x2 mm^2) was placed over the sample to mark the ROI. An image was acquired using a light microscope Zeiss Stemi SV6 Stereo, figure 8.1c, to be used as a reference map during the scans. A preliminary fast transmission scan over the metal was performed to identify the ROI. Afterwards, a raster scan, with a scanning increment of 100 µm, and typically 300s exposure time (per raster point) was performed on the ROI. The integrated intensity (I(q)) and the correlation length (l_c) were calculated for all the specimens. However, it has to be pointed out that since in the measurements only a limited **q** range (q_{min} and q_{max})is available and the tissue is a hierarchical material[1], the calculation of I(q) and l_c were evaluated over a selected q-regime ($q_{min} = 0.1\ nm^{-1}$ and $q_{max} = 2.5\ nm^{-1}$).
Integrated intensity and correlation length act as very sensitive scattering image quantifiers, providing complementary contrast at the nanoscale compared to the transmission signal. Generally, and simplified, I(q) is proportional to the volume fraction, the square of the scattering contrast and the dimension of the scatterers in the media, while l_c is related to the shape and dimension of the scatterer in the media only.

8.3 Results

Figure 8.2a and b depicts an example of a whole histological slice used as reference for the SAXS measurements and the ROI (blue square) selected. Figure 8.2c shows, with the help of the symbols *, § , $, that the same region selected in the histology (figure 8.2b) can be found in the 100 um slice measured with SAXS. Figure 8.2d and e depict the integration and correlation length maps, respectively. Figure 8.3a and b show the ROI measured with SAXS for the PF_{bleo}, while Figure 8.4a and b the ROI for the PF_{gen}. These four images prove that the areas selected in the histology can be found in the 100 µm slice measured with SAXS. The integrated intensity contains information about the electron density of the scatter in the media (the higher the intensity, the higher the electron density). This can be clearly seen in figure 8.3c, in which * points to a vessel full of blood (high value for I(q)), while $ shows an empty vase (low value of the intensity). Figure 8.3c and 8.4c depict the integrated intensity for PF_{bleo} and PF_{gen}, respectively, showing that the consolidation regions in both models do not differ significantly from the electron density point of view. The correlation length provides information about the shape and the dimension of the scatter in the media, independently of the mass. Figure 8.3d and 8.4 depict the l_c maps for PF_{bleo} and PF_{gen}, respectively, showing that the composition of the consolidation regions is different in terms of dimension and shape of the scattering media. More precisely, PF_{bleo} showed a composition made of bigger particles compared to PF_{gen}. This was a pilot experiment, to test if lung tissue as well as the sample preparation was suitable for these measurements. Furthermore, it was also attempted to detect the collagen I signal.

[1]This does not allow to unanimously approximating by the scattering pattern to $q_{min} = 0$ and $q_{max} = \infty$

Unfortunately, the signal-to-noise ratio was too low. To measure the collagen I signal longer measurements, higher intensity and brilliant beam would have been required, and to date the Austrian SAXS beamline set-up cannot provide these requirements.

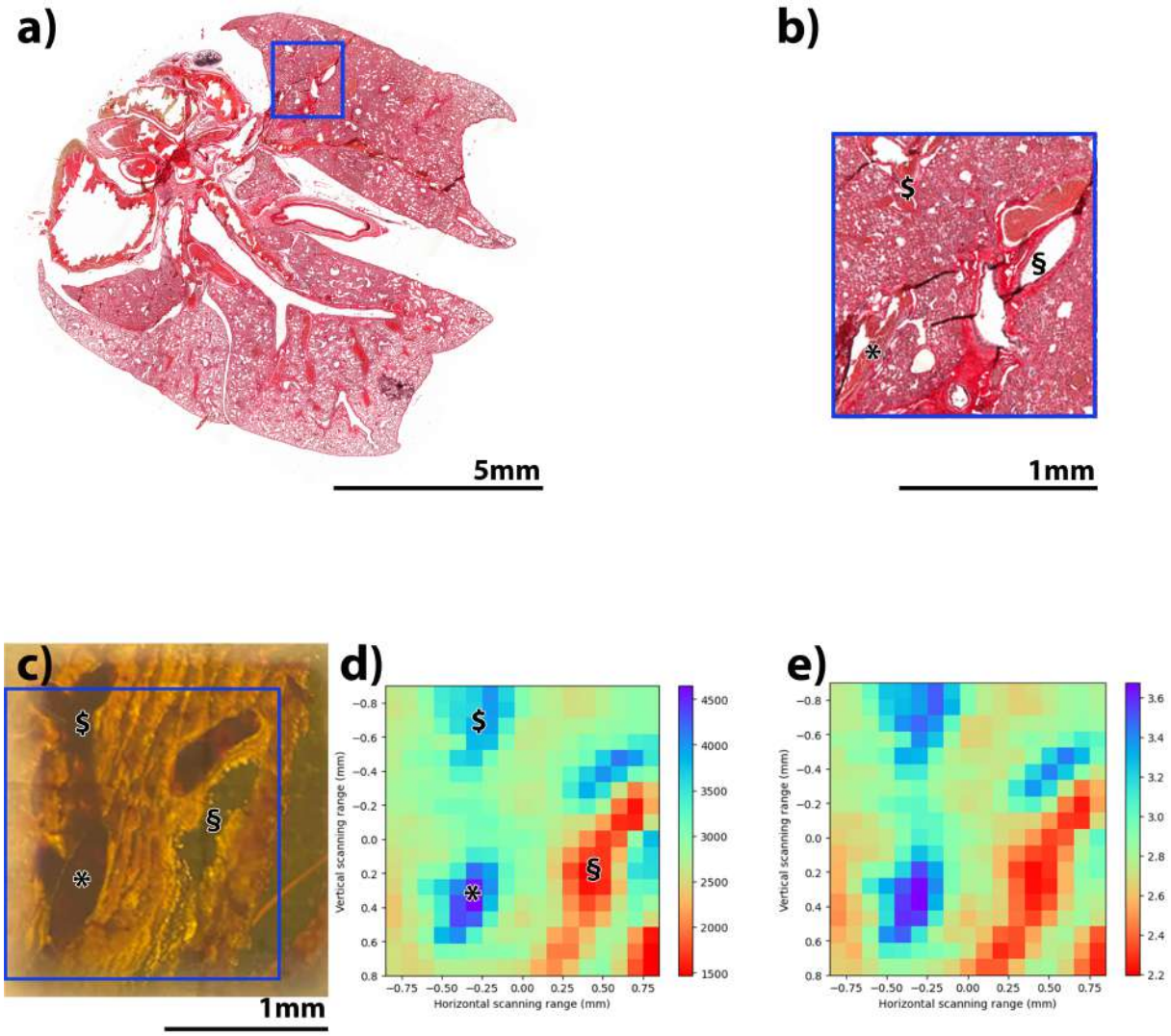

Figure 8.2: Example of the approach exploited for the SAXS measurements. a) Picrosirius red staining histology used to identify the ROI (blue square). b) Magnification of the selected ROI. c) Optical image of the 100 µm slice deposited over Kapton tape. The blue square depicts the ROI measured. d) Integrated intensity map of the ROI. e) Correlation length map of the ROI. Note: *,$, and § were used to indicate the same structures in the different imaging modalities.

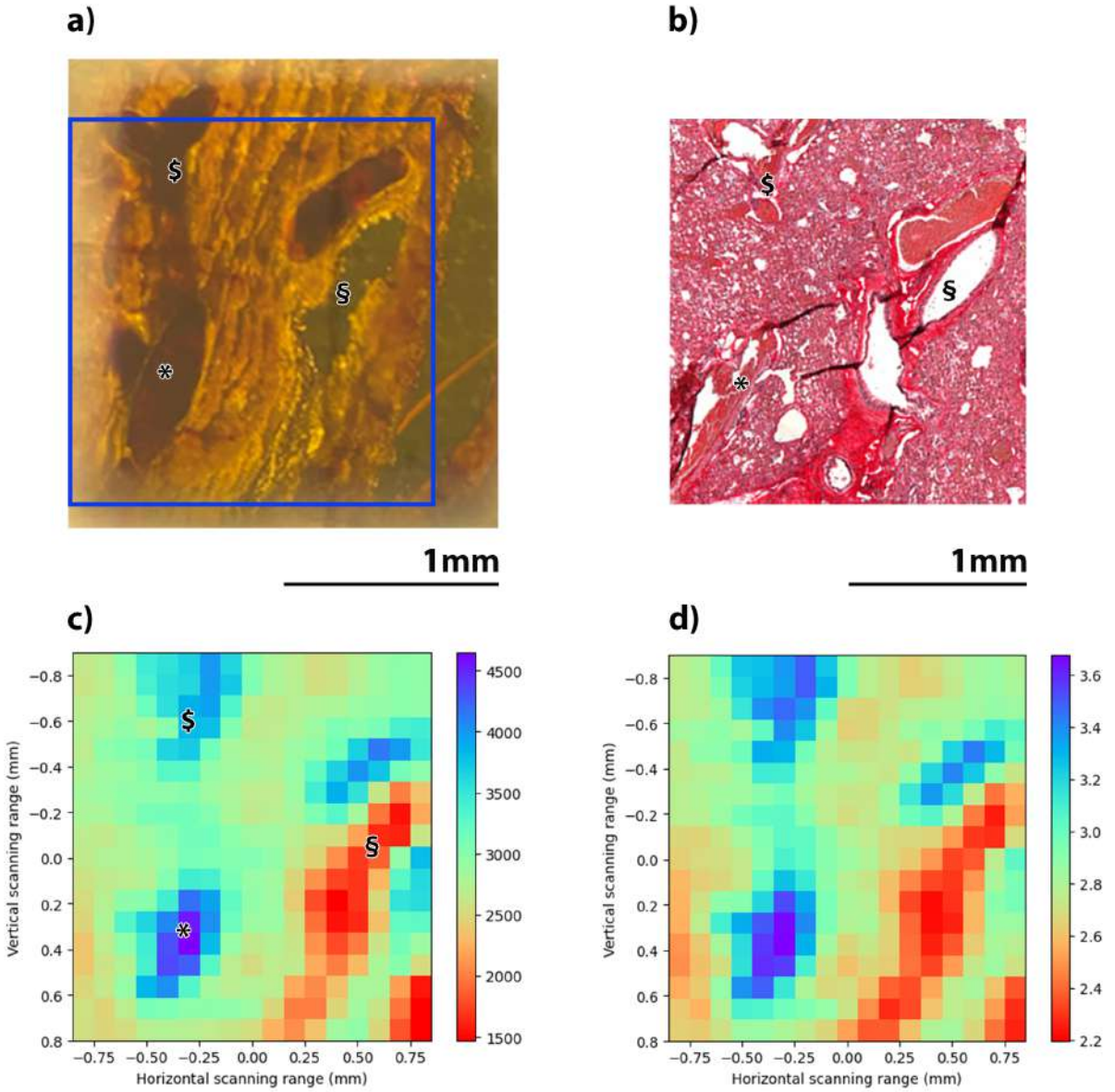

Figure 8.3: Results of the SAXS measurements for a PF_{bleo} mice. a) Optical image of the 100 µm tissue deposited on Kapton tape (The blue square represents the ROI measured with SAXS). b) ROI of the histological slice, which matches the ROI measured with SAXS. c) Integrated Intensity map. d) Correlation length map. Note: the symbols *,$,§ are used in the different images to show the correspondence of the structures.

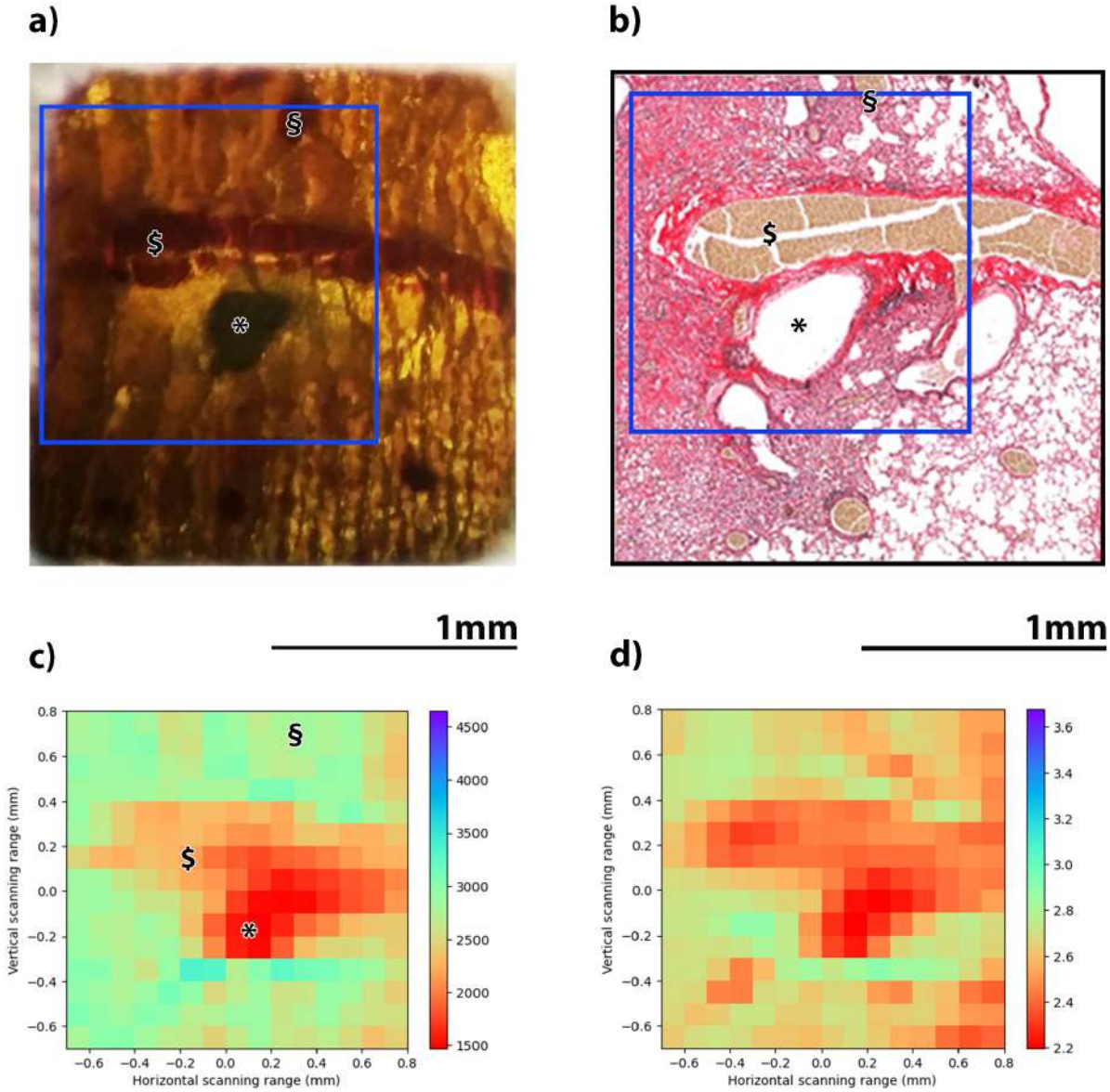

Figure 8.4: Results of the SAXS measurements for a PF_{gen} mice. a) Optical image of the 100 µm tissue deposited on Kapton tape (The blue square represents the ROI measured with SAXS). b) ROI of the histological slice, which matches the ROI measured with SAXS. c) Integrated Intensity map. d) Correlation length map. Note: the symbols *,$,§ are used in the different images to show the correspondence of the structures.

Chapter 9

Elastic Registration

In this chapter, the elastic registration performed to fuse the data acquired by micro-CT, histology, AFM and FTIR is presented.

9.1 Material and Method

All the data generated with the different techniques of the pipeline was elastic registered using Fuxlastix [48], which is a frontend of Elastix [67]. Fuxlastix performs elastic registration using b-spline interpolation and mutual information as optimization criteria. Table 9.1 shows the data dimension, type, and the information for each technique of the pipeline.

Technique	Dimension	Data type	Information
PBI	3D	grey scale images	3D volume of the lung
Histology (picrosirius)	2D	colour image	5 µm slice of lung tissue
Histology + polarization filter	2D	colour image	Collagen I and III deposition
FTIR	2D	colour image	K-Means clustering
AFM	3D	colour images	3D representation of Young's moduli

Table 9.1: Summary of the data collected with the multitechnique pipeline.

9.2 Result

Figure 9.1 depicts the results of the 3D integration of the all the techniques of the pipeline: Propagation-based imaging micro-CT, histology, Fourier Transform Infrared Spectroscopy, and Atomic Force Microscopy. The 3D micro-CT data set depicts the whole paraffin block prior to the cutting and was therefore considered showing the real shape of the lung tissue. Elastic registration was performed to fuse the data provided by histology, FTIR, and AFM since they were collected on tissue slices that were non-uniform deformed during the cutting. The integration of all the data was the result of multiple elastic registration processes that were performed in a precise order. In some cases, the output of one registration was used as input for the following one (see below).

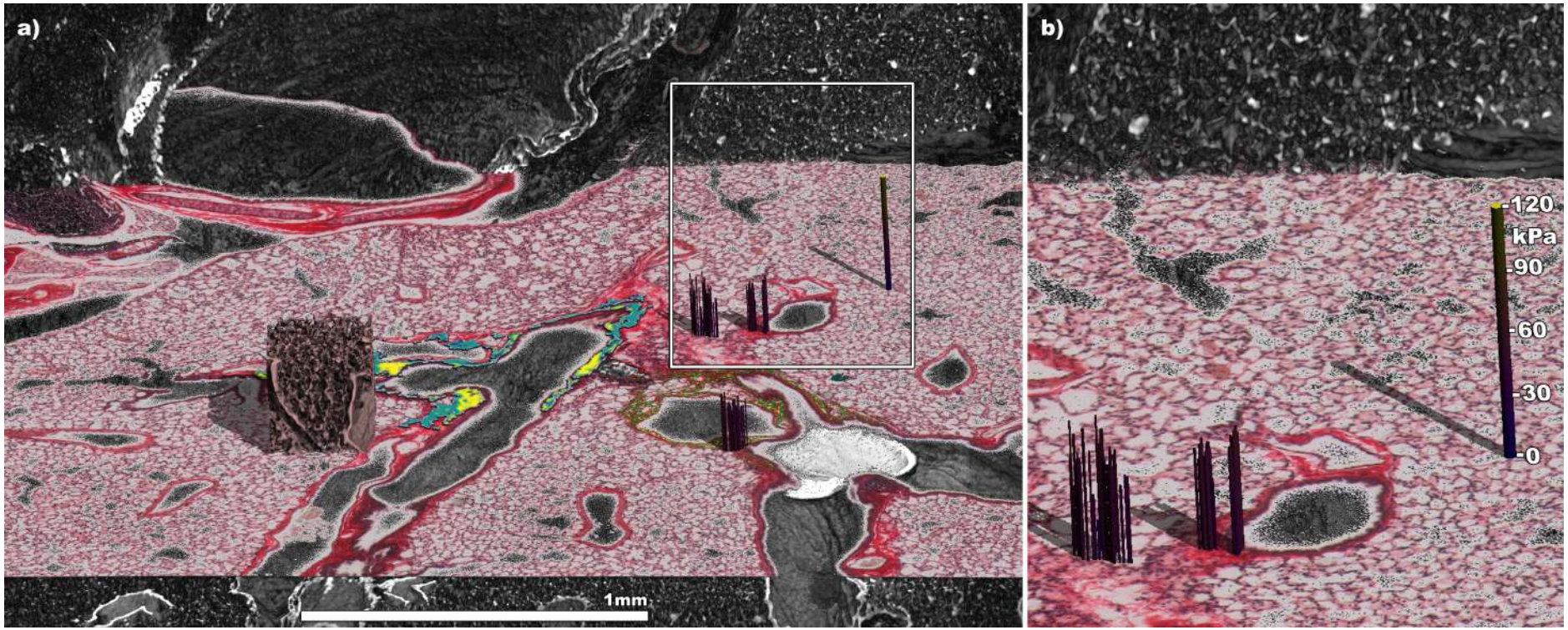

Figure 9.1: 3D integration of PBI, histology, FTIR and AFM. a) A cube is presented to demonstrate an example of the region covered in the structural analysis. On top of the picrosirius stained slice, both the result of the collagen I and III mapping obtained with FTIR (close to the cube) as well as an image of the histology acquired with a polarization filter are shown. Moreover, the locations of the AFM measurements are depicted as well as including a scale bar. b) a close-up of one of the AFM measurements.

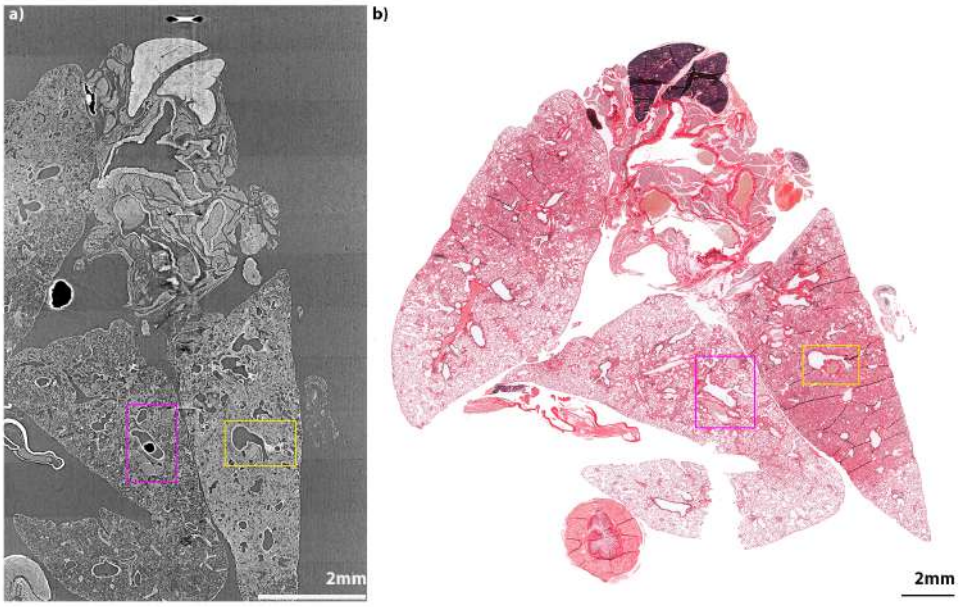

Figure 9.2: Evaluation of the histological position inside the 3D micro-CT dataset. a) 2D slice of the micro-CT data set. b) 2D image of histology. The yellow rectangle shows features, in both a) and b) that are very similar. These two features were used as references during the process of finding the position of the histology inside the micro-CT dataset. The two purple rectangles highlights two regions which are not the same for the a) and b) indicating that the orientation of the microtome blade was not the same as the virtual cutting plane used to slice the 3D volume.

At first, the histological slice was registered to the PBI data. To this end, a virtual cut through the 3D volume was performed to find the position at which the histology was taken, figure 9.2. Then the cutting plane was manually rotated until the 2D micro-CT slice and the histology showed mostly the same orientation. Figure 9.3 depicts an example of such a pair of 2D micro-CT slice (a) and corresponding rotation corrected histological slice (b). Subsequently, the CT data was set as "fixed" image while the histology was used as "moving" image.

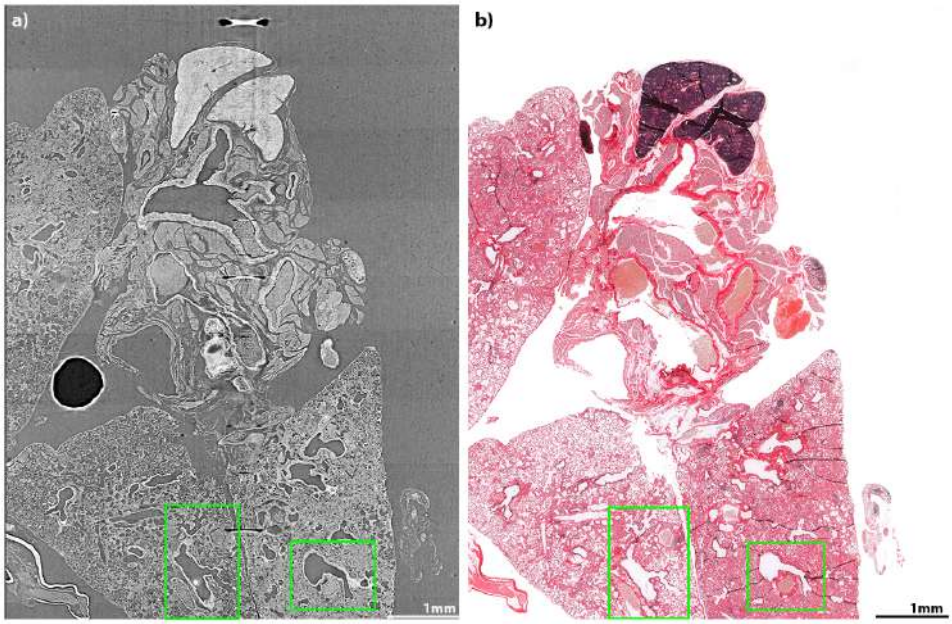

Figure 9.3: Example of the input for the elastic registration. a) 2D slice of the micro-CT data set, b) 2D image of histology. The orientation of the virtual cutting plane is adjusted until a) and b) match. The green rectangles show matching regions after the orientation adjustment.

The deformation corrected histological slice was then used as reference for the registration of the histological slice imaged with a polarization filter and the 3D bar plots of the Young's moduli. The fusion with the 3D micro-CT data of the K-Means clustering was more challenging and its registration was performed on the already deformed image of the histology combined with the polarization filter, due to the fact that it showed similar image content. Figure 9.4a)-b) depict the "fixed" image and "moving" image used for the elastic registration of the AFM over the histology. Figure 9.4c) shows the output of the registration. In particular, a grid representation depicts the deformation applied to match the "fixed" image with the "moving" one. Figure 9.4 shows, by means of a checker board view, that after the deformation the optical image matches perfectly the histology.

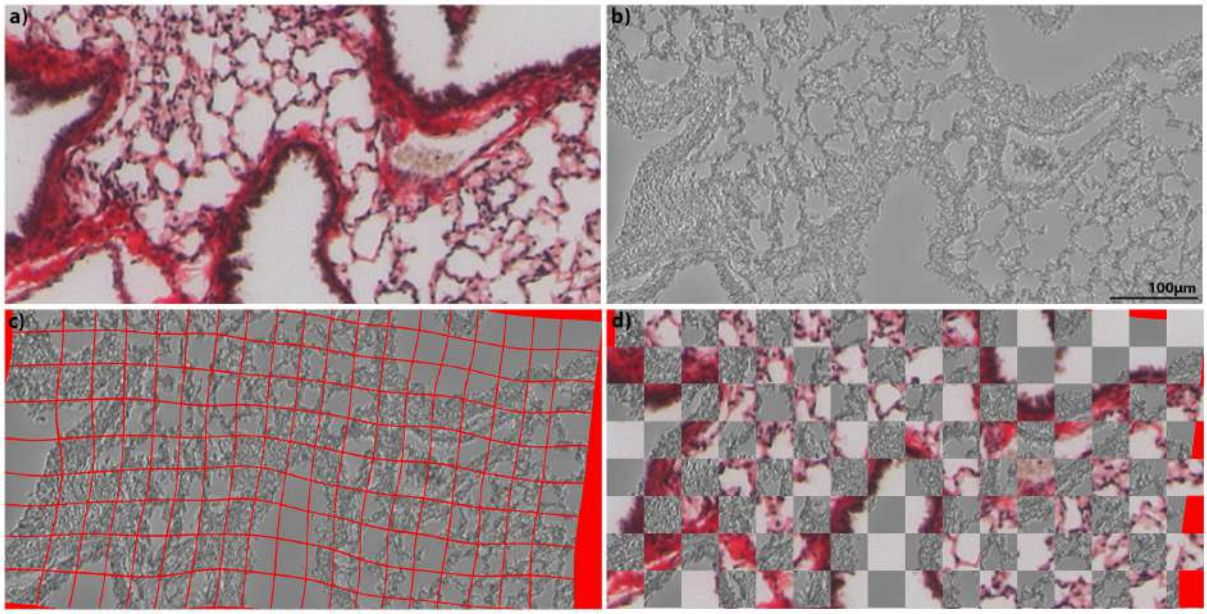

Figure 9.4: Input and output of the elastic registration between AFM and histology. a) Histology cropped ("fixed" image). b) ROI in which AFM measurements were performed ("moving" image). c) Elastic deformation of the "moving" image, represented by a grid (the red borders indicate the degree of deformation calculated by the registration pipeline). d) Checker board view of the optical image and the histology.

In this case, the only manual cropping and resizing of the histology to match the ROI measured with the force spectroscopy technique was required as pre-processing. The same pre-processing was performed to register the polarize histology and the histology. Figure 9.5a) shows the cropped and resized histology used as "fixed" image, while figure 9.5b) represents the same region imaged with a polarization filter, used as "moving" image. Figure 9.5c) depicts the deformations applied (light blue) to match the two histological images, while figure 9.5d) demonstrated the perfect matching, exploiting a checker boarder view. Figure 9.5e) depicts the deformed histology coupled with the polarization filter, that was set as "fixed" image for the next elastic registration process. Figure 9.5f) shows the K-means clustering, which was used as "moving" image. Figure 9.5g) displays the deformations (light blue) applied on the FTIR data, while figure 9.5h) demonstrates a perfect match between the histology coupled with the polarization filter and the K-means, exploiting a checker board representation.

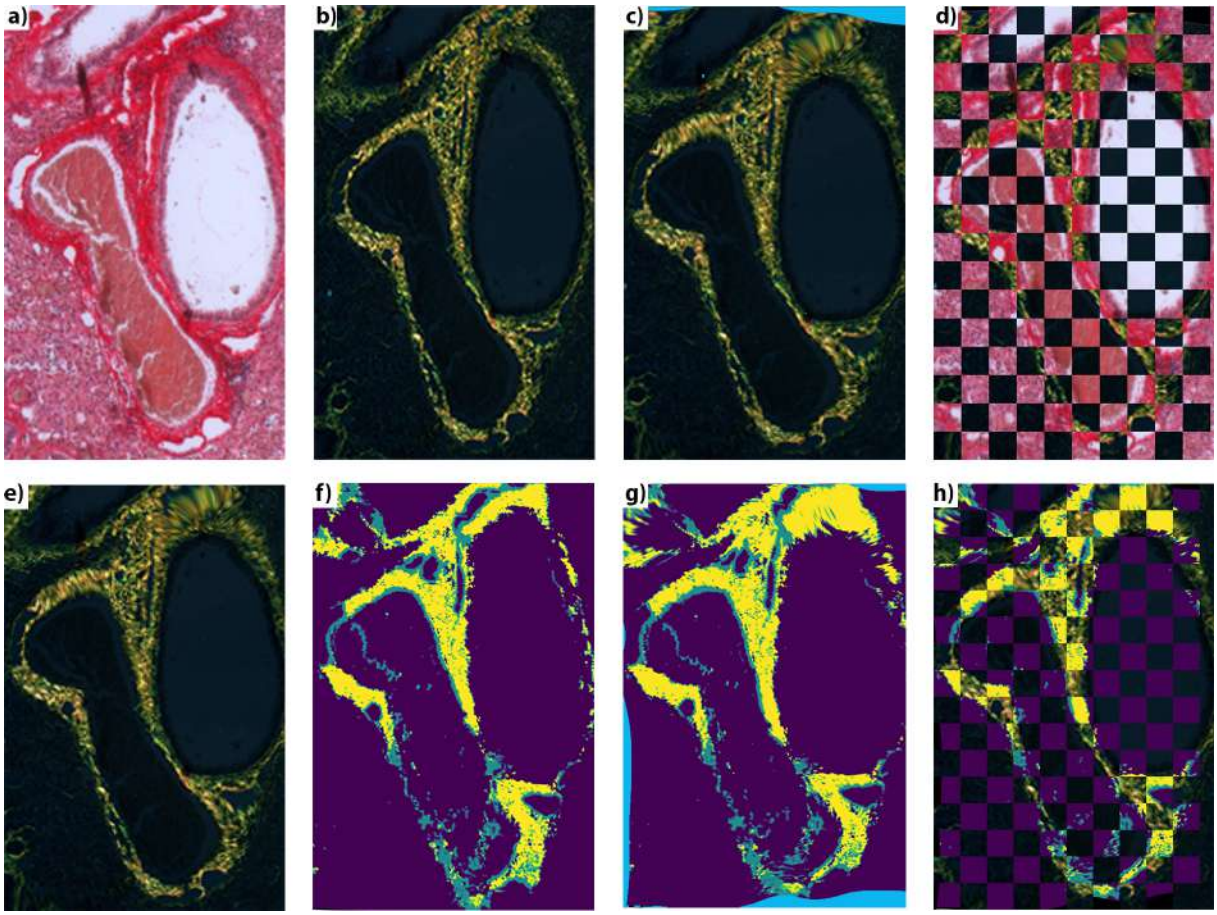

Figure 9.5: Elastic registration of the FTIR data with histology.a) Picrosirius red staining used as “fixed” image. b) Picrosirius red staining coupled with a polarization filter used as “moving” image. c) Result of the elastic registration, in light blue the deformed areas. d) Checker board image of the overlap between “fixed” and “moving” image, showing a perfect match. e) Output of the first registration used as “fixed” image for the second elastic registration. f) K-means cluster map of collagen I and III used as “moving” image. g) Result of the elastic registration, in light blue the deformed areas. h)Checker board image of the overlap between “fixed” and “moving” image, showing a perfect match.

Chapter 10

Correlation

In this chapter, the benefit of the combined information for the characterization of PF is shown.

10.1 Background: Classical evaluation of lung fibrosis

Due to the limited resolution (roughly 40 µm pixel size) in in-vivo imaging, especially in small animal models, lung fibrosis is typically characterized by histology. To this end, the Ashcroft score [60] is commonly employed. This methodology was applied in the thesis to label the severity of all the lungs used in the experiment. It ranges from 0 = healthy to 8 = severe fibrosis. The score is computed on multiple local regions within the histological slices, aiming for a representative value for the entire lung. This score relies just on the severity of the fibrosis, therefore it is not sensitive enough to reveal differences between the two PF models. Figure 10.1 depicts two lobes: one (left) from the Nedd4-2 KO model and one (right) from the bleomycin model. These two lungs have the same Ashcroft score, and it is impossible to differentiate them. This is an example of how classical histology is not sensitive enough to discriminate between the conditional Nedd4-2 KO and bleomycin induced PF models.

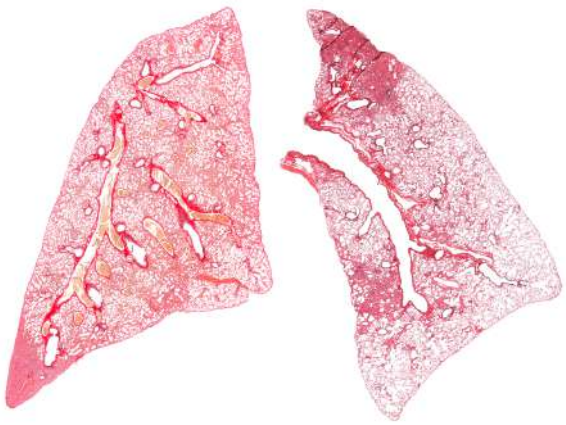

Figure 10.1: Example of two lungs' lobes with the same Ashcroft score. On the left Nedd4-2 KO model, on the right the bleomycin-induced model.

10.2 Material and method

10.2.1 Agglomerative Clustering

For a more comprehensive analysis, the information acquired by different modalities: micro-CT, FTIR, and AFM, was combined. Thus, each specimen/mice can be thought of as a high dimensional vector, containing all the parameters measured with the above-mentioned techniques. In order to evaluate if all these features can allow a more comprehensive characterization of the different models, an agglomerative clustering analysis was performed. This is an iterative method, where, at the beginning, each point is treated as an independent class. At each iteration, each point is compared with the others, and if they are similar they are joined in one group. This joining process continues until one large group remains. The step at which certain points or subgroups have joined is typically displayed as a dendrogram, which converts similarities of the data in the high dimensional feature space into a 2D graph. In order to perform agglomerative clustering, the metric to calculate the similarity and the method of joining needs to be defined. Here, cosine similarity based on z-scores of the features was used. Simplistically, all different features are scaled to the same dynamic range to give them equal importance and the angle between two data points can be calculated based on the scalar product. The rationale behind this is the idea that feature vectors pointing in the exact same direction in the feature space represent very similar objects, resulting in an angle of 0 and therefore in a cosine of 1. Different directions in the feature space are therefore representing more different objects, resulting in lower cosine similarity. Therefore, in that metric similarity is based on the difference of the angle and not of the distance between two feature vectors, Thus, cosine-similarity performs a rather relative than absolute comparison of the individual vector dimension, and it is more suited for high-dimensional sparse data, such as in the case of the here presented PhD thesis. As linkage criteria the "complete" criteria was used. This utilizes the maximum distance between all observations of the two sets. In the same way, not only the objects/mice can be grouped, but also the individual features based on their correlation. This combined approach is called cluster map and was employed here.

10.3 Results: Agglomerative Clustering

Agglomerative clustering analysis was subsequently performed, adding the features of the additional methods. Figure 10.2 depicts the 3 clustering analyses performed. The same metric, normalization, and linkage were exploited, in all the agglomerative measurements. In figure 10.2a only the results of the morphological analysis performed on the micro-CT data was used. Looking at the horizontal dendrogram, it is clear that the features exploited in this first attempt were not enough to lead to a good classification. Indeed, there is no clear separation between the groups (CN, PF_{gen}, PF_{bleo}). Figure 10.2b shows that using a combination of the information gained with micro-CT and AFM, leads to a better grouping. Indeed, in this case, looking at the horizontal dendrogram, it is clearer that 3 groups are present. In the upper part, all the controls and the treated mice are clustered in one group. Furthermore, the two controls are grouped together with the CN_{bleo} (lines 1 to 4 of the cluster map), and only later they join

the CN_{gen} (lines 5 to 8). Then the two fibrotic models PF_{gen} and PF_{bleo} are separated in two different clusters. In figure 10.2b, if a line is drawn at a certain depth of the dendrogram, either four groups, CN_{bleo}+PF_{bleo}+TREAT, CN_{gen}, PF_{gen}, and PF_{bleo},(green line), or 3 groups, CN + PF_{bleo}+TREAT, PF_{gen}, and PF_{bleo}, (red line), can be obtained.

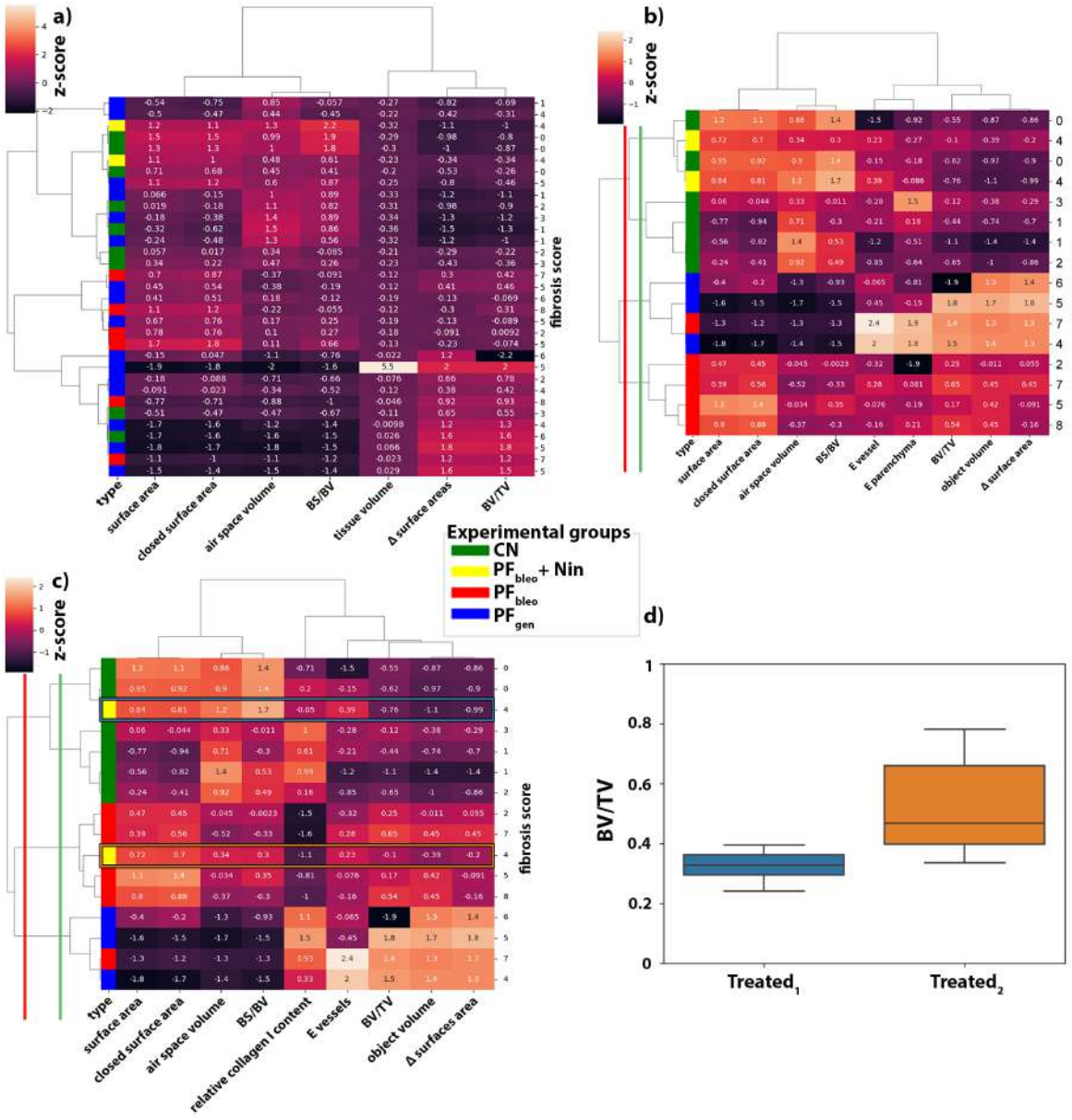

Figure 10.2: Clustering maps at different steps of the pipeline. a) Cluster map of the morphological features. b) Cluster map of the combination of morphological and biomechanical features.c) Cluster map of the combination of morphological, biomechanical, and percentage of collagen features. d) Percentage of tissue for the PF_{bleo}+TREAT showing that the sample 7347 is correctly cluster in c) with the PF_{bleo} since the amount of consolidation tissue is higher.

Then, also the FTIR features were added for clustering approach, figure 10.2c. In this case, the algorithm was able to get 3 or 4 groups, depending on which depth of the dendrogram was considered, red line or green line, respectively. However, the introduction of the relative collagen I content, allowed to cluster one PF_{bleo}+TREAT with PF_{bleo}. This is also confirmed by figure 10.2d, which shows higher percentage of tissue for the mice that is then clustered with the PF_{bleo}

group.

Chapter 11

Discussion

In the here presented thesis, I was able to establish a general analysis pipeline for FFPE tissue specimen combining PBI micro-CT, classical histology, AFM, FTIR, and SAXS. I demonstrated that most of the data could even be spatially correlated on a nearly cellular level using elastic registration. In addition, the application of this pipeline on specimens of two different lung fibrosis mouse models revealed for the first time differences in the fibrotic regions, which were not known before and could not be detected by classical histology only.

microCT as alternative to histology

Histology can be considered as the gold-standard of tissue analysis on a cellular level. A large variety of staining protocols allows highlighting specific cell or tissue types. Especially in combination with immunohistochemistry - the use of labelled antibodies - targeting cell specific surface proteins, for instance cancer, can be identified effectively. However, histology has some known limitations such as the need for physical sectioning of the specimen, which not only destroys it in the process but also requires embedding it in a ridged matrix, most commonly paraffin.

Micro-CT has already been established as a 3D non-destructive alternative to classical histology - often called virtual histology. In terms of soft-tissue, the approach is hindered by the low contrast, which in turn requires the use of heavy ion based staining procedures such as described by Metscher et al. [68]. There are few reported attempts to scan FFPE-tissue without additional staining using classical micro-CT. Handschuh et al. [69] published an approach to scan horse embryos embedded in paraffin without additional staining. However, multiple (5) filtering steps are required to achieve a meaningful contrast-to-noise ratio and more importantly, the embryo was sculptured out of the block. This approach defeats the purpose of scanning FFPE-tissue as it does not allow for subsequent histological sectioning of the tissue without re-embedding, which in turn would destroy the geometrical relationship between both measurements. Phase contrast computed tomography, especially propagation based imaging, is characterized by strongly elevated soft-tissue contrast [70]. Thus, PBI is an ideal tool for imaging unstained tissue such as FFPE blocks, an approach often called label free virtual histology. The non-destructive 3D representation of the tissue is particularly helpful to target the sectioning process to sites of interest, as described by Albers et al. [71]. However, in this publication, this was still achieved in combination with staining protocols. To overcome the non-specific nature of PBI based

label-free histology, correlative imaging with classical histology is the logical choice. In various applications such as by Sengle et al. [72] such an approach is pursued. However, the sectioning process introduces non-uniform deformations of the tissue, which need to be addressed to allow a perfect overlay of the data. Sengle et al. [72] for instance tackled this by manual manipulation of the data in Photoshop™. Many others such as Eckermann et al. [73] simply show a side-by-side comparison of the two modalities without attempting a direct overlay. I followed the approach of Albers et al.[48] using elastic registration between the histological sections and a manually adjusted virtual cut through the CT data sets. This well established workflow does not only yield a nearly perfect match of histology and CT, it also enables the use of histology as a bridge to spatially register even more 2D techniques to the corresponding CT data set, as I showed for the AFM and FTIR data. Furthermore, PBI micro-CT has been extensively used for the quantitative assessment of pulmonary microanatomy, in the context of a wide range of lung diseases [74], [75]. In the present work, cube shaped sub-volumes were extracted from the 3D lung data sets, and several metrics, presented in chapter 4, were analysed to gain information about the structural changes due to fibrosis. Nevertheless, exploiting only these morphological parameters was not sufficient for a discrimination between the two fibrotic models. However, a high positive correlation between the histological scoring and the tissue volume was found, in agreement to the data shown by Tanabe et al. [76].

FTIR - a label free technique for characterizing lung fibrosis

FTIR is a label-free and non-destructive technique that has been exploited in the last decades to gain information concerning the molecular composition and structure of biological tissue. The combination of IR spectroscopy (chemical analysis) with optical microscopy allows coupling spatial information with spectral data. Protocols for the application of FTIR are well established for both frozen and FFPE specimens [33], [77]. In the case of FFPE specimens, it is compatible with the standard clinical workflow of histological tissue analysis. FTIR microspectroscopy can be used as a diagnostic tool for many pathologies, in which changes in the molecular composition occur. For instance, Yano et al. [78] showed that FTIR is sensitive enough to depict an increase in the glycogen content and a decrement in the cholesterol content, in cancerous tissue, and thus allows distinguishing between cancerous and non-cancerous tissue. In the past, IR investigation of tissue samples was usually focused on cancer and other disease affecting epithelia and parenchyma, while nowadays the research has focused towards the characterization of for instance the surrounding regions of stroma and fibrotic regions [79]. These regions have been studied both as pathologically significant areas in their own right and as interdependent partners in complex disease processes [79]. The areas of stroma and fibrosis share a common feature, which is a high collagen content. As demonstrated by Belbachir et al. [37] several different types of this protein can be identified by means of IR spectra. Therefore, differences in the collagen type and composition, which corresponds to changes in the IR spectra, allow unravelling pathological differences between areas of stroma and fibrosis [80], [81].

I used FTIR as a tool for the quantification of collagen I and collagen III, which are the most predominant fibre types in lung tissue [82]. Suryadevara et al. [83] performed IR spectroscopy on the same bleomycin-induced pulmonary fibrosis mouse model used in the here presented PhD

thesis, showing patterns similar to the fibrotic features detectable in classical histology.

In the presented PhD thesis, I followed a similar approach [83] for the quantification of collagen I and III content. I applied K-Means clustering on the IR image, using only the most relevant wavelengths identified by PCA. The usage of this approach provided additional quantitative information about the fibre content that was not accessible by classical histology. However, it has to be pointed out that all the lung tissue slices were not dewaxed and the areas measured were considered to be composed by a mixture of collagen I and III only. The paraffin was not removed in order to preserve the tissue, for the subsequent AFM analysis.

AFM measurements for biomechanical characterization of fibrotic regions

AFM is a type of scanning probe microscopy (SPM) that can be exploited both for topographic and biomechanical measurements. This tool has been used for the characterization of structural and mechanical properties in a wide range of biological tissues, such as liver [44], brain [46], and lungs [45]. Since the elasticity of the lung is linked to the concentration of two fibre types: collagen and elastin [84], lung fibrosis which is characterized by deposition of collagen will in turn change the compliance of the lung. Therefore, AFM is well suited to further investigate this process. A combination of FTIR and AFM was already presented by Blat et al. [85], for the validation of biochemical parameters of the thrombi in acute ischaemic stroke. Blat et al. performed topographic measurements on frozen tissue, exploiting AFM, while I used this technique to retrieve the local stiffness on dewaxed lung tissue slices previously measured with FTIR. The embedding media as well as the sample thickness and holder were chosen to allow to spatially correlate these measurements with the other techniques. All the lung tissue slices were deparaffinized and rehydrated following the protocol presented in chapter 7, and measured in water. A potential limitation of this approach arises from the required formalin fixation, which alters the mechanical properties of the tissue. Calo et al. [86] performed force spectroscopy AFM on biological tissue prepared with different fixations and protocols, showing that FFPE led to the smallest difference between the studied collagen rich and collagen low content regions in liver specimens of humans and mice. My AFM measurement results (chapter 7) are in agreement with the findings of Calo et al.: the median values of the Young's moduli for the perivascular regions (high collagen content), parenchyma regions (low collagen content), and consolidation regions (low collagen content), were found to be very similar independent of the region of the lung. However, I found that the stiffness in the genetically modified mouse model was significantly increased compared to the bleomycin mouse model. This is not likely to be a result of differences in the sample preparation, because the controls of both the groups expressed roughly the same Young's modulus.

SAXS a potential tool for fibres composition in lung fibrosis

None of the so far discussed methods have the ability to address the structural dimension of collagen fibres. Therefore, I applied Small Angle X-Rays Scattering (SAXS). SAXS is an analytical method that can be exploited to determine the structure (at the nano scale) of systems in terms of average particle size and shape. Furthermore, the diffraction peaks obtained with this technique allow gaining information on the packing of structures inside a material. SAXS was

successfully applied in a very broad range of fields, including biological materials [87], colloids [88], and fuel cells [89]. Biological tissues have a hierarchical organization, optimized at all levels to provide specific mechanical functions, such as compliance in lungs. Mohd Sobri et al.[90] showed that synchrotron radiation small-angle X-rays scattering (SR-SAXS) can be exploited to distinguish between benign tumour, malignant tumour, and non-lesional tumour tissue. This was accomplished observing the intensity of scattering peaks, which revealed that malignant tumours have higher triglyceride content compared to the non-lesional tissue. Furthermore, Mohd Sobri et al. [90] and Tsolaki et al. [91], showed that SR-SAXS can be used to measure the scattering peaks of collagen in breast tissue and bioprosthetic heart valves, respectively. The collagen signal was used in both studies to discriminate between cancerous and non-cancerous breast tissue [90], and between calcified and non-calcified tissue [91], respectively. Moreover, Tsolaki et al. [91] investigated bioprosthetic heart valves not only with SR-SAXS, but also with micro-CT, histology, scanning electron microscopy (SEM), confocal and two-photon microscopy, demonstrating that SR-SAXS can successfully be used in a multimodal tissue analysis pipeline. In the here presented PhD thesis, a pilot study on FFPE lung tissue was performed to evaluate the structural difference between two fibrotic mouse models at the nanoscale. In this study, two metrics (presented in chapter 8) were measured: integrated intensity and correlation length. In particular, the integrated intensity is correlated to the mass of the scatter media, while the correlation length provides information regarding the shapes and the dimensions of the scatter media. I was not able to extract the specific scattering peaks of collagen due to certain boundary conditions such as the thickness of the sample and the set-up of the Austrian SAXS beamline of the Italian synchrotron Elettra. In contrast, Mohd Sobri et al. [90] were able to identify the collagen peaks as they used 10 times thicker tissue slices, resulting in a higher S/N ratio. Furthermore, the approach presented by Mohd Sobri et al. [90] placing the extracted tissue in an Eppendorf tube, would not allow the spatial correlation with here presented techniques. Therefore, sample preparation proposed by Mohd Sobri et al. was not suited for the multimodal pipeline presented in this PhD thesis, for two main reasons: a) all paraffin blocks were cut with a microtome in which a cutting thickness bigger than 100 µm can only hardly be achieved, and b) the lung tissue is less homogenous than the breast tissue studied by Mohd Sobri et al. [90]. Tsolaki et al. [91] used SR-SAXS, in a multitechnique study, as in the here presented thesis. However, it has to be pointed out that in the work of Tsolaki et al. [91], who measured bioprosthetic heart valves, the specimens were much larger than here. Moreover, the samples analysed by SR-SAXS were not the same studied with the other techniques of the pipeline. To measure the collagen signal in the here presented only 100 µm thick lung tissue slices, would have required a much longer exposure time as well as higher energy and brilliance of the beam. These condition could not have been fulfilled at the Austrian SAXS beamline of Elettra. However, the upcoming upgrade of Elettra will make the study with such tissue's thickness feasible. Based on the preliminary results, the correlation length seems to be promising for the discrimination between the two fibrotic models, showing that PF_{gen} have the consolidation region made by particles with smaller dimensions compared to PF_{bleo}.

Spatial correlation of the imaging modalities

I was able to spatially correlate all the above-mentioned techniques, except for the SAXS, as shown in chapter 9. The decision of excluding the integrated intensity and correlation length maps from the spatial registration was based on the fact that the spatial resolution of 100 µm was much lower than of all the other techniques. Furthermore, this technique was excluded also from the clustering analysis (chapter 10) because it was difficult to condense the SAXS results into single values for each mouse.
The spatial correlation of micro-CT, FTIR, AFM and histology, is one of the main achievements of the presented work, as it is in no way limited to mouse lung tissue. Since general FFPE-tissue samples were used, the work flow can be applied without further modification to other tissue types, such as archived human material. Currently, multi-modal readouts such as the application of genomics [92], proteomic [93], transcriptomics [94] on tissue samples are pursued. Also in these cases, it has been established that the results are vastly dependent on the position within the tissue, due to the strong heterogeneity of diseases. Therefore, it is imperative to perform spatially resolved measurements [95]. Any spatially resolved data could be integrated in the presented pipeline (if FFPE specimens can be used and the method is not affected by X-ray dose effects in the specimen) which would not only allow to supplement the information of one method by the other but also to assign different features to the same tissue region or even to the same cell.

Limitations and future improvements

Despite the fact that FFPE tissue is the most commonly applied preparation method for soft-tissue in clinical routine as well as in biomedical research, the condition of such tissue is challenging for some of the used techniques. The rather severe processes of formalin fixation and chemicall drying change protein structures and mechanical properties dramatically. Thus, AFM shows less sensitive results - as mentioned above. Nevertheless, a stiff matrix for the unavoidable sectioning process in histology needs to be provided. Alternatives to paraffin could be agarose, resin or cryo-sectioning in OCT. Agarose, due to the high water content, is challenging for PBI as the high X-ray dose rate can cause bubble formation. Moreover, cutting is performed with a vibratome that does not allow for very thin sections, lowering the quality of standard histology. In addition, still formalin fixation is applied, which would lower the quality of AFM. Resin does also not present an alternative to the here presented pipeline. It provides better results than paraffin for PBI. However, it seems to penetrate deeper into the tissue and thus generates a lower gradient in the refractive index between tissue penetrated by resin and surrounding resin in comparison to tissue in paraffin. Our experiments show that PBI is less effective, and resin embedded tissue without additional staining is virtually impossible to image. Cryo-conservation of tissue might work. Imaging frozen lung tissue has for instance successfully been performed by Reichmann et al. [96] but without a matrix. Such an approach does not integrate in the here presented pipeline as it does not permit subsequent sectioning. Therefore, it still needs to be demonstrated if cryo-preserved lung tissue embedded in OCT generates enough contrast in PBI. If so, this would require to perform PBI using a cryo-jet to cool the specimen during the scan, which however has already been performed by for instance Maes et al.[97] on stained tissues.

Thus, this would be an interesting future development of the here presented approach.
I successfully applied the developed pipeline on two different mouse lung fibrosis models, which based on the commonly applied Ashcroft score [60] are indistinguishable in histology. Since the Ashcroft score is characterizing structural changes, it showed a high correlation with the structural parameter obtained by CT. Only by adding additional features obtained by AFM characterizing mechanical properties, a successful clustering of the two models including the wildtype controls was achieved. This might present a first indication of underlying differences in the composition of the fibrotic regions, which however would need extensive follow-up studies until reliable conclusion can be drawn - especially raising the numbers of analysed specimens. Moreover, as shown in chapter 10, with the progressive addition of the parameters retrieved from the modalities presented in this work, the quality of the agglomerative clustering improved, after every addition. In particular, when only micro-CT was used a clear separation between the experimental group was impossible. Adding the data from the AFM allowed me to clearly separate the different experimental groups into 3 clusters (controls and PF_{bleo} + Nin, PF_{gen}, PF_{bleo}). Finally, adding the FTIR results also allowed to demonstrate that Nintendanib treatment was not successful in one mouse, as confirmed by comparing the tissue volume of the PF_{bleo} + Nin. In the future, I plan to apply this method on lung tissue specimens from patients that passed away due to COVID in the first wave of the pandemic. PBI scans have already been performed, and first AFM tests showed differences between patients that got ventilated and others that did not. In this particular case of human lung tissue, the large degree of comorbidities makes the analysis very challenging. Thus, I believe a spatially correlated approach as provided by the developed pipeline would be of the utmost importance, to allow the analysis to be focused to sites which does not clearly show features of other lung disease.

Author's Publications

List of Author's publications produced within the PhD program.

- Buccino, F., Bagherifard, S., **D'Amico, L.**, Zagra, L., Banfi, G., Tromba, G., Vergani, L.M., 2022. Assessing the intimate mechanobiological link between human bone microscale trabecular architecture and micro-damages. Engineering Fracture Mechanics 270, 108582. https://doi.org/10.1016/j.engfracmech.2022.108582

- Buccino, F., Zagra, L., Longo, E., **D'Amico, L.**, Banfi, G., Berto, F., Tromba, G., Vergani, L.M., 2023. Osteoporosis and Covid-19: Detected similarities in bone lacunar-level alterations via combined AI and advanced synchrotron testing. Materials Design 231, 112087. https://doi.org/10.1016/j.matdes.2023.112087

- **D'Amico, L.**, Svetlove, A., Longo, E., Meyer, R., Senigagliesi, B., Saccomano, G., Nolte, P., Wagner, L., Mall, M.A., Casalis, L., Köster, S., Alves, F., Tromba, G., Dullin, C., Characterization of lung fibrosis by spatially correlated phase contrast microCT, classical histolpathology and atomic force microscopy. (Under revision)

- DAndrea, L., Gastaldi, D., Baino, F., Vern, E., Saccomano, G., **D'Amico, L.**, Longo, E., Schwentenwein, M., Vena, P., 2022. Mechanical Characterization of Miniaturized 3D-Printed Hydroxyapatite Parts Obtained Through Vat Photopolymerization: An Experimental Study. SSRN Electronic Journal. https://doi.org/10.2139/ssrn.4149296

- De Martino, E., Medeot, C., **D'Amico, L.**, Stanta, G., Bonin, S., 2022. Impact of standardization in tissue processing: the performance of different fixatives. New Biotechnology 71, 3036. https://doi.org/10.1016/j.nbt.2022.07.001

- Dullin, C., **D'Amico, L.**, Saccomano, G., Longo, E., Wagner, W.L., Reiser, J., Svetlove, A., Albers, J., Contillo, A., Abrami, A., Sturari, L., Tromba, G., Sodini, N., Dreossi, D., 2023. Novel setup for rapid phase contrast CT imaging of heavy and bulky specimens. J Synchrotron Rad 30, 650654. https://doi.org/10.1107/S1600577523001649

- Hickman-Lewis, K., Cavalazzi, B., Giannoukos, K., **D'Amico, L.**, Vrbaski, S., Saccomano, G., Dreossi, D., Tromba, G., Foucher, F., Brownscombe, W., Smith, C.L., Westall, F., 2023. Advanced two- and three-dimensional insights into Earths oldest stromatolites (ca. 3.5 Ga): Prospects for the search for life on Mars. Geology 51, 3338. https://doi.org/10.1130/G50390.1

- Levin, V., Petronyuk, Y., Artyukov, I., Bukreeva, I., Malykhin, A., Longo, E., **D'Amico, L.**, Giannoukos, K., Tromba, G., 2023. Three-Dimensional Study of Polymer Composite Destruction in the Early Stages. Polymers 15, 276. https://doi.org/10.3390/polym15020276

- Palermo, F., Pieroni, N., Sanna, A., Parodi, B., Venturi, C., Begani Provinciali, G., Massimi, L., Maugeri, L., Marra, G.P., Longo, E.,**D'Amico, L.**, Saccomano, G., Perrin, J., Tromba, G., Bukreeva, I., Fratini, M., Gigli, G., Kerlero de Rosbo, N., Cedola, A., 2022. Multilevel X-ray imaging approach to assess the sequential evolution of multi-organ damage in multiple sclerosis. Commun Phys 5, 112. https://doi.org/10.1038/s42005-022-01070-3

- Petruzzellis, F., Di Bonaventura, A., Tordoni, E., Tomasella, M., Natale, S., Trifil, P., Tromba, G., Di Lillo, F., **D'Amico, L.**, Bacaro, G., Nardini, A., 2023. The optical method based on gas injection overestimates leaf vulnerability to xylem embolism in three woody species. Tree Physiology tpad088. https://doi.org/10.1093/treephys/tpad088

- Suman, A., Vulpio, A., Casari, N., Pinelli, M., di Lillo, F., **D'Amico, L.**, 2021. Analysis of soil and soot deposits by X-ray computed microtomography. Powder Technology 394, 608621. https://doi.org/10.1016/j.powtec.2021.08.072

- Suman, A., Vulpio, A., Pinelli, M., **D'Amico, L.**, 2022. Microtomography of Soil and Soot Deposits: Analysis of Three-Dimensional Structures and Surface Morphology. Journal of Engineering for Gas Turbines and Power 144. https://doi.org/10.1115/1.4055217

- Svetlove, A., Griebel, T., Albers, J., **D'Amico, L.**, L., Nolte, P., Tromba, G., Bohnenberger, H., Dullin, C., n.d. X-ray phase contrast 3D virtual histology characterises complex tissue architecture in colorectal cancer.

- Tomasella, M., Natale, S., Petruzzellis, F., Di Bert, S., **D'Amico, L.**, Tromba, G., Nardini, A., 2022. No Evidence for Light-Induced Embolism Repair in Cut Stems of Drought-Resistant Mediterranean Species under Soaking. Plants 11, 307. https://doi.org/10.3390/plants11030307

References

[1] The Lancet, GBD 2017: a fragile world, The Lancet 392 (2018) 1683.

[2] GBD Chronic Respiratory Disease Collaborators, Prevalence and attributable health burden of chronic respiratory diseases, 1990-2017: a systematic analysis for the Global Burden of Disease Study 2017, The Lancet. Respiratory Medicine 8 (2020) 585–596.

[3] E. Vasarmidi, M. Ghanem, B. Crestani, Interstitial lung disease following coronavirus disease 2019, Current Opinion in Pulmonary Medicine 28 (2022) 399–406.

[4] S. Conti, S. Harari, A. Caminati, A. Zanobetti, J. Schwartz, P. A. Bertazzi, G. Cesana, F. Madotto, The association between air pollution and the incidence of idiopathic pulmonary fibrosis in Northern Italy, European Respiratory Journal 51 (2018) 1700397.

[5] C. M. Magro, W. J. Waldman, D. A. Knight, J. N. Allen, T. Nadasdy, G. E. Frambach, P. Ross, C. B. Marsh, Idiopathic Pulmonary Fibrosis Related to Endothelial Injury and Antiendothelial Cell Antibodies, Human Immunology 67 (2006) 284–297.

[6] F. Li, J. Deng, Y. Song, C. Wu, B. Yu, G. Wang, J. Li, Y. Zhong, F. Liang, Pulmonary fibrosis in patients with COVID-19: A retrospective study, Frontiers in Cellular and Infection Microbiology 12 (2022).

[7] S. D. Nathan, O. A. Shlobin, N. Weir, S. Ahmad, J. M. Kaldjob, E. Battle, M. J. Sheridan, R. M. d. Bois, Long-term Course and Prognosis of Idiopathic Pulmonary Fibrosis in the New Millennium, CHEST 140 (2011) 221–229. Publisher: Elsevier.

[8] Y. N. Lamb, Nintedanib: A Review in Fibrotic Interstitial Lung Diseases, Drugs 81 (2021) 575–586.

[9] A. Aimo, G. Spitaleri, D. Nieri, L. M. Tavanti, C. Meschi, G. Panichella, J. Lupn, F. Pistelli, L. Carrozzi, A. Bayes-Genis, M. Emdin, Pirfenidone for Idiopathic Pulmonary Fibrosis and Beyond, Cardiac Failure Review 8 (2022) e12.

[10] T. Pitre, R. Husnudinov, M. F. Khalid, M. C. Zhang, S. Cui, J. Tran, J. Mah, W. Helmeczi, J. Su, A. Jones, D. Zeraatkar, Nintedanib, Pirfenidone and Pirfenidone Versus Nintedanib: A Systematic Review And Meta-Analysis, preprint, In Review, 2021.

[11] Anatomy of the Heart and Lungs, 2015.

[12] Idiopathic Pulmonary Fibrosis Clinical Research Network, G. Raghu, K. J. Anstrom, T. E. King, J. A. Lasky, F. J. Martinez, Prednisone, azathioprine, and N-acetylcysteine for pulmonary fibrosis, The New England Journal of Medicine 366 (2012) 1968–1977.

[13] S. Saito, A. Alkhatib, J. K. Kolls, Y. Kondoh, J. A. Lasky, Pharmacotherapy and adjunctive treatment for idiopathic pulmonary fibrosis (IPF), Journal of Thoracic Disease 11 (2019) S1740–S1754.

[14] L. Wollin, E. Wex, A. Pautsch, G. Schnapp, K. E. Hostettler, S. Stowasser, M. Kolb, Mode of action of nintedanib in the treatment of idiopathic pulmonary fibrosis, The European Respiratory Journal 45 (2015) 1434–1445.

[15] E. Bargagli, C. Piccioli, E. Rosi, E. Torricelli, L. Turi, E. Piccioli, M. Pistolesi, K. Ferrari, L. Voltolini, Pirfenidone and Nintedanib in idiopathic pulmonary fibrosis: Real-life experience in an Italian referral centre, Pulmonology 25 (2019) 149–153.

[16] T. M. Dempsey, S. Payne, L. Sangaralingham, X. Yao, N. D. Shah, A. H. Limper, Adoption of the Antifibrotic Medications Pirfenidone and Nintedanib for Patients with Idiopathic Pulmonary Fibrosis, Annals of the American Thoracic Society 18 (2021) 1121–1128.

[17] D. M. Walters, S. R. Kleeberger, Mouse Models of Bleomycin-Induced Pulmonary Fibrosis, Current Protocols in Pharmacology 40 (2008) 5.46.1–5.46.17. _eprint: https://onlinelibrary.wiley.com/doi/pdf/10.1002/0471141755.ph0546s40.

[18] J. Duerr, D. H. W. Leitz, M. Szczygiel, D. Dvornikov, S. G. Fraumann, C. Kreutz, P. K. Zadora, A. Seyhan Agircan, P. Konietzke, T. A. Engelmann, J. Hegermann, S. Mulugeta, H. Kawabe, L. Knudsen, M. Ochs, D. Rotin, T. Muley, M. Kreuter, F. J. F. Herth, M. O. Wielptz, M. F. Beers, U. Klingmller, M. A. Mall, Conditional deletion of Nedd4-2 in lung epithelial cells causes progressive pulmonary fibrosis in adult mice, Nature Communications 11 (2020) 2012. Number: 1 Publisher: Nature Publishing Group.

[19] D. B. Chandler, Possible Mechanisms of Bleomycin-Induced Fibrosis, Clinics in Chest Medicine 11 (1990) 21–30.

[20] P. Mukherjee, S. Roy, D. Ghosh, S. K. Nandi, Role of animal models in biomedical research: a review, Laboratory Animal Research 38 (2022) 18.

[21] N. L. H. Phillips, T. L. Roth, Animal Models and Their Contribution to Our Understanding of the Relationship Between Environments, Epigenetic Modifications, and Behavior, Genes 10 (2019) 47.

[22] A. Monteiro, R. Smith, Bronchial tree Architecture in Mammals of Diverse Body Mass, International Journal of Morphology 32 (2014) 312–316.

[23] J. Thiesse, E. Namati, J. C. Sieren, A. R. Smith, J. M. Reinhardt, E. A. Hoffman, G. McLennan, Lung structure phenotype variation in inbred mouse strains revealed through in vivo micro-CT imaging, Journal of Applied Physiology 109 (2010) 1960–1968. Publisher: American Physiological Society.

[24] R. Lattouf, R. Younes, D. Lutomski, N. Naaman, G. Godeau, K. Senni, S. Changotade, Picrosirius Red Staining: A Useful Tool to Appraise Collagen Networks in Normal and Pathological Tissues, Journal of Histochemistry & Cytochemistry 62 (2014) 751–758.

[25] S.-A. Zhou, A. Brahme, Development of phase-contrast X-ray imaging techniques and potential medical applications, Physica Medica 24 (2008) 129–148.

[26] Infrared Basics - IR Heating Equipment and Infrared Ovens by PROTHERM, LLC, 2014.

[27] Interactive 3D Chemistry Animations, 2015.

[28] Michelson interferometer, 2022. Page Version ID: 1117788054.

[29] Fourier-transform infrared spectroscopy, 2023. Page Version ID: 1173451893.

[30] S. C. Chua, F. K. Chong, M. R. U. Musta, S. R. M. Kutty, M. A. Malek, P. L. Show, Y. Chia, OPEN Microwave radiation-induced (2014).

[31] E. Benedetti, E. Bramanti, F. Papineschi, I. Rossi, E. Benedetti, Determination of the Relative Amount of Nucleic Acids and Proteins in Leukemic and Normal Lymphocytes by Means of Fourier Transform Infrared Microspectroscopy, Applied Spectroscopy 51 (1997) 792–797. Publisher: SAGE Publications Ltd STM.

[32] A. C. S. Talari, M. A. G. Martinez, Z. Movasaghi, S. Rehman, I. U. Rehman, Advances in Fourier transform infrared (FTIR) spectroscopy of biological tissues, Applied Spectroscopy Reviews 52 (2017) 456–506. Publisher: Taylor & Francis _eprint: https://doi.org/10.1080/05704928.2016.1230863.

[33] M. J. Baker, J. Trevisan, P. Bassan, R. Bhargava, H. J. Butler, K. M. Dorling, P. R. Fielden, S. W. Fogarty, N. J. Fullwood, K. A. Heys, C. Hughes, P. Lasch, P. L. Martin-Hirsch, B. Obinaju, G. D. Sockalingum, J. Sul-Suso, R. J. Strong, M. J. Walsh, B. R. Wood, P. Gardner, F. L. Martin, Using Fourier transform IR spectroscopy to analyze biological materials, Nature Protocols 9 (2014) 1771–1791. Number: 8 Publisher: Nature Publishing Group.

[34] J. Kong, S. Yu, Fourier Transform Infrared Spectroscopic Analysis of Protein Secondary Structures, Acta Biochimica et Biophysica Sinica 39 (2007) 549–559.

[35] S. Tsukada, C. J. Parsons, R. A. Rippe, Mechanisms of liver fibrosis, Clinica Chimica Acta 364 (2006) 33–60.

[36] J. A. Last, A. D. Siefkin, K. M. Reiser, Type I collagen content is increased in lungs of patients with adult respiratory distress syndrome., Thorax 38 (1983) 364–368.

[37] K. Belbachir, R. Noreen, G. Gouspillou, C. Petibois, Collagen types analysis and differentiation by FTIR spectroscopy, Analytical and Bioanalytical Chemistry 395 (2009) 829–837.

[38] H.-J. Butt, B. Cappella, M. Kappl, Force measurements with the atomic force microscope: Technique, interpretation and applications, Surface Science Reports 59 (2005) 1–152.

[39] F. Bano, L. Fruk, B. Sanavio, M. Glettenberg, L. Casalis, C. M. Niemeyer, G. Scoles, Toward Multiprotein Nanoarrays Using Nanografting and DNA Directed Immobilization of Proteins, Nano Letters 9 (2009) 2614–2618. Publisher: American Chemical Society.

[40] N. Ishida, V. Craig, Direct Measurement of Interaction Forces between Surfaces in Liquids Using Atomic Force Microscopy, KONA Powder and Particle Journal 36 (2019).

[41] P. Eaton, Atomic Force MicroscopyAFM, in: Kirk-Othmer Encyclopedia of Chemical Technology, John Wiley & Sons, Ltd, 2011, 2011, pp. 1–19. _eprint: https://onlinelibrary.wiley.com/doi/pdf/10.1002/0471238961.0120151319011809.a01.pub2.

[42] A Practical Guide to AFM Force Spectroscopy and Data Analysis, 2012.

[43] Measuring and Analyzing Force-Distance Curves with AFM, 2012.

[44] S. Ojha, J. Pribyl, S. Klimovic, D. Hadraba, M. Jirouskova, M. Gregor, Measurement of Liver Stiffness using Atomic Force Microscopy Coupled with Polarization Microscopy, Journal of Visualized Experiments: JoVE (2022).

[45] F. Liu, D. J. Tschumperlin, Micro-Mechanical Characterization of Lung Tissue Using Atomic Force Microscopy, Journal of Visualized Experiments : JoVE (2011) 2911.

[46] P. K. Viji Babu, M. Radmacher, Mechanics of Brain Tissues Studied by Atomic Force Microscopy: A Perspective, Frontiers in Neuroscience 13 (2019) 600.

[47] O. Glatter, Chapter 1 - interference, rayleighdebyegans theory, in: O. Glatter (Ed.), Scattering Methods and their Application in Colloid and Interface Science, Elsevier, 2018, 2018, pp. 1–18.

[48] J. Albers, A. Svetlove, J. Alves, A. Kraupner, F. di Lillo, M. A. Markus, G. Tromba, F. Alves, C. Dullin, Elastic transformation of histological slices allows precise co-registration with microCT data sets for a refined virtual histology approach, Scientific Reports 11 (2021) 10846.

[49] J. Tashiro, G. A. Rubio, A. H. Limper, K. Williams, S. J. Elliot, I. Ninou, V. Aidinis, A. Tzouvelekis, M. K. Glassberg, Exploring animal models that resemble idiopathic pulmonary fibrosis, Frontiers in medicine 4 (2017) 118.

[50] C. Dullin, M. A. Markus, E. Larsson, G. Tromba, S. Hlsmann, F. Alves, X-Ray based Lung Function measurementa sensitive technique to quantify lung function in allergic airway inflammation mouse models, Scientific Reports 6 (2016) 36297.

[51] A. Svetlove, J. Albers, S. Hlsmann, M. A. Markus, J. Zschntzsch, F. Alves, C. Dullin, Non-Invasive Optical Motion Tracking Allows Monitoring of Respiratory Dynamics in Dystrophin-Deficient Mice, Cells 11 (2022) 918.

[52] R. G. Jenkins, B. B. Moore, R. C. Chambers, O. Eickelberg, M. Knigshoff, M. Kolb, G. J. Laurent, C. B. Nanthakumar, M. A. Olman, A. Pardo, M. Selman, D. Sheppard, P. J. Sime, A. M. Tager, A. L. Tatler, V. J. Thannickal, E. S. White, An Official American

Thoracic Society Workshop Report: Use of Animal Models for the Preclinical Assessment of Potential Therapies for Pulmonary Fibrosis, American Journal of Respiratory Cell and Molecular Biology 56 (2017) 667–679.

[53] A. Khan, M. A. Markus, A. Svetlove, S. Hlsmann, F. Alves, C. Dullin, Longitudinal x-ray based lung function measurement for monitoring Nintedanib treatment response in a mouse model of lung fibrosis, Scientific Reports 13 (2023) 18637.

[54] D. H. W. Leitz, P. Konietzke, W. Wagner, M. Mertiny, C. Benke, T. Schneider, W. Stiller, H.-U. Kauczor, M. A. Mall, J. Duerr, M. O. Wielptz, Longitudinal Micro-Computed Tomography Detects Onset and Progression of Pulmonary Fibrosis in Conditional Nedd4-2 Deficient Mice, 2023. Pages: 2023.08.31.555725 Section: New Results.

[55] F. Brun, S. Pacil, A. Accardo, G. Kourousias, D. Dreossi, L. Mancini, G. Tromba, R. Pugliese, Enhanced and Flexible Software Tools for X-ray Computed Tomography at the Italian Synchrotron Radiation Facility Elettra, Fundamenta Informaticae 141 (2015) 233–243. Publisher: IOS Press.

[56] D. Paganin, S. C. Mayo, T. E. Gureyev, P. R. Miller, S. W. Wilkins, Simultaneous phase and amplitude extraction from a single defocused image of a homogeneous object, Journal of Microscopy 206 (2002) 33–40. _eprint: https://onlinelibrary.wiley.com/doi/pdf/10.1046/j.1365-2818.2002.01010.x.

[57] F. Charlier, M. Weber, D. Izak, E. Harkin, M. Magnus, J. Lalli, L. Fresnais, M. Chan, N. Markov, O. Amsalem, S. Proost, A. Krasoulis, getzze, S. Repplinger, Statannotations, 2022.

[58] P. Virtanen, R. Gommers, T. E. Oliphant, M. Haberland, T. Reddy, D. Cournapeau, E. Burovski, P. Peterson, W. Weckesser, J. Bright, S. J. van der Walt, M. Brett, J. Wilson, K. J. Millman, N. Mayorov, A. R. J. Nelson, E. Jones, R. Kern, E. Larson, C. J. Carey, İ. Polat, Y. Feng, E. W. Moore, J. VanderPlas, D. Laxalde, J. Perktold, R. Cimrman, I. Henriksen, E. A. Quintero, C. R. Harris, A. M. Archibald, A. H. Ribeiro, F. Pedregosa, P. van Mulbregt, SciPy 1.0 Contributors, SciPy 1.0: Fundamental Algorithms for Scientific Computing in Python, Nature Methods 17 (2020) 261–272.

[59] M. L. Waskom, seaborn: statistical data visualization, Journal of Open Source Software 6 (2021) 3021.

[60] T. Ashcroft, J. M. Simpson, V. Timbrell, Simple method of estimating severity of pulmonary fibrosis on a numerical scale., Journal of Clinical Pathology 41 (1988) 467–470.

[61] M. Titford, The long history of hematoxylin, Biotechnic & Histochemistry 80 (2005) 73–78. Publisher: Taylor & Francis _eprint: https://doi.org/10.1080/10520290500138372.

[62] J. K. C. Chan, The Wonderful Colors of the HematoxylinEosin Stain in Diagnostic Surgical Pathology, International Journal of Surgical Pathology 22 (2014) 12–32. Publisher: SAGE Publications Inc.

[63] L. C. Junqueira, G. Bignolas, R. R. Brentani, Picrosirius staining plus polarization microscopy, a specific method for collagen detection in tissue sections, The Histochemical Journal 11 (1979) 447–455.

[64] J. A. Cavallo, A. A. Roma, M. S. Jasielec, J. Ousley, J. Creamer, M. D. Pichert, S. Baalman, M. M. Frisella, B. D. Matthews, C. R. Deeken, Remodeling characteristics and collagen distribution in synthetic mesh materials explanted from human subjects after abdominal wall reconstruction: an analysis of remodeling characteristics by patient risk factors and surgical site classifications, Surgical Endoscopy 28 (2014) 1852–1865.

[65] D. R. Whelan, K. R. Bambery, P. Heraud, M. J. Tobin, M. Diem, D. McNaughton, B. R. Wood, Monitoring the reversible B to A-like transition of DNA in eukaryotic cells using Fourier transform infrared spectroscopy, Nucleic Acids Research 39 (2011) 5439–5448.

[66] H. Amenitsch, M. Rappolt, M. Kriechbaum, H. Mio, P. Laggner, S. Bernstorff, First performance assessment of the small-angle X-ray scattering beamline at ELETTRA, Journal of Synchrotron Radiation 5 (1998) 506–508.

[67] S. Klein, M. Staring, K. Murphy, M. A. Viergever, J. P. W. Pluim, elastix: a toolbox for intensity-based medical image registration, IEEE transactions on medical imaging 29 (2010) 196–205.

[68] B. D. Metscher, Microct for comparative morphology: simple staining methods allow high-contrast 3d imaging of diverse non-mineralized animal tissues, BMC physiology 9 (2009) 1–14.

[69] S. Handschuh, C. T. C. Okada, I. Walter, C. Aurich, M. Glsmann, An optimized workflow for microCT imaging of formalinfixed and paraffinembedded (FFPE) early equine embryos, Anatomia, Histologia, Embryologia 51 (2022) 611–623.

[70] M. J. Kitchen, G. A. Buckley, T. E. Gureyev, M. J. Wallace, N. Andres-Thio, K. Uesugi, N. Yagi, S. B. Hooper, Ct dose reduction factors in the thousands using x-ray phase contrast, Scientific reports 7 (2017) 15953.

[71] J. Albers, M. A. Markus, F. Alves, C. Dullin, X-ray based virtual histology allows guided sectioning of heavy ion stained murine lungs for histological analysis, Scientific reports 8 (2018) 7712.

[72] G. Sengle, S. F. Tufa, L. Y. Sakai, M. A. Zulliger, D. R. Keene, A Correlative Method for Imaging Identical Regions of Samples by Micro-CT, Light Microscopy, and Electron Microscopy: Imaging Adipose Tissue in a Model System, Journal of Histochemistry & Cytochemistry 61 (2013) 263–271.

[73] M. Eckermann, B. Schmitzer, F. Van Der Meer, J. Franz, O. Hansen, C. Stadelmann, T. Salditt, Three-dimensional virtual histology of the human hippocampus based on phase-contrast computed tomography, Proceedings of the National Academy of Sciences 118 (2021) e2113835118.

[74] N. Tanabe, D. M. Vasilescu, J. E. McDonough, D. Kinose, M. Suzuki, J. D. Cooper, P. D. Par, J. C. Hogg, MicroComputed Tomography Comparison of Preterminal Bronchioles in Centrilobular and Panlobular Emphysema, American Journal of Respiratory and Critical Care Medicine 195 (2017) 630–638.

[75] S. Nakamura, K. Mori, S. Iwano, K. Kawaguchi, T. Fukui, S. Hakiri, N. Ozeki, M. Oda, K. Yokoi, Micro-computed tomography images of lung adenocarcinoma: detection of lepidic growth patterns, Nagoya Journal of Medical Science 82 (2020) 25–31.

[76] N. Tanabe, J. E. McDonough, D. M. Vasilescu, K. Ikezoe, S. E. Verleden, F. Xu, W. A. Wuyts, B. M. Vanaudenaerde, T. V. Colby, J. C. Hogg, Pathology of Idiopathic Pulmonary Fibrosis Assessed by a Combination of Microcomputed Tomography, Histology, and Immunohistochemistry, The American Journal of Pathology 190 (2020) 2427–2435.

[77] D. C. Fernandez, R. Bhargava, S. M. Hewitt, I. W. Levin, Infrared spectroscopic imaging for histopathologic recognition, Nature Biotechnology 23 (2005) 469–474.

[78] K. Yano, S. Ohoshima, Y. Gotou, K. Kumaido, T. Moriguchi, H. Katayama, Direct measurement of human lung cancerous and noncancerous tissues by fourier transform infrared microscopy: can an infrared microscope be used as a clinical tool?, Analytical Biochemistry 287 (2000) 218–225.

[79] S. S. Nazeer, H. Sreedhar, V. K. Varma, D. Martinez-Marin, C. Massie, M. J. Walsh, Infrared Spectroscopic Imaging: Label-Free Biochemical Analysis of Stroma and Tissue Fibrosis, The international journal of biochemistry & cell biology 92 (2017) 14–17.

[80] B. Bird, J. Rowlette, A protocol for rapid, label-free histochemical imaging of fibrotic liver, Analyst 142 (2017) 1179–1184. Publisher: The Royal Society of Chemistry.

[81] S. Tiwari, J. Raman, V. Reddy, A. Ghetler, R. P. Tella, Y. Han, C. R. Moon, C. D. Hoke, R. Bhargava, Towards Translation of Discrete Frequency Infrared Spectroscopic Imaging for Digital Histopathology of Clinical Biopsy Samples, Analytical Chemistry 88 (2016) 10183–10190.

[82] J. M. Seyer, E. T. Hutcheson, A. H. Kang, Collagen polymorphism in idiopathic chronic pulmonary fibrosis, The Journal of Clinical Investigation 57 (1976) 1498–1507.

[83] V. Suryadevara, S. S. Nazeer, H. Sreedhar, O. Adelaja, A. Kajdacsy-Balla, V. Natarajan, M. J. Walsh, Infrared spectral microscopy as a tool to monitor lung fibrosis development in a model system, Biomedical Optics Express 11 (2020) 3996.

[84] J. P. Desai, F. Moustarah, Pulmonary Compliance, in: StatPearls, StatPearls Publishing, Treasure Island (FL), 2023, 2023.

[85] A. Blat, J. Dybas, K. Chrabaszcz, K. Bulat, A. Jasztal, M. Kaczmarska, R. Pulyk, T. Popiela, A. Slowik, K. Malek, M. G. Adamski, K. M. Marzec, FTIR, Raman and AFM characterization of the clinically valid biochemical parameters of the thrombi in acute ischemic stroke, Scientific Reports 9 (2019) 15475. Number: 1 Publisher: Nature Publishing Group.

[86] A. Cal, Y. Romin, R. Srouji, C. P. Zambirinis, N. Fan, A. Santella, E. Feng, S. Fujisawa, M. Turkekul, S. Huang, A. L. Simpson, M. DAngelica, W. R. Jarnagin, K. Manova-Todorova, Spatial mapping of the collagen distribution in human and mouse tissues by force volume atomic force microscopy, Scientific Reports 10 (2020) 15664.

[87] P. Fratzl, N. Fratzl-Zelman, K. Klaushofer, G. Vogl, K. Koller, Nucleation and growth of mineral crystals in bone studied by small-angle X-ray scattering, Calcified Tissue International 48 (1991) 407–413.

[88] B. Abcassis, F. Testard, O. Spalla, P. Barboux, Probing in situ the Nucleation and Growth of Gold Nanoparticles by Small-Angle X-ray Scattering, Nano Letters 7 (2007) 1723–1727. Publisher: American Chemical Society.

[89] G. O. Park, J. Yoon, E. Park, S. B. Park, H. Kim, K. H. Kim, X. Jin, T. J. Shin, H. Kim, W.-S. Yoon, J. M. Kim, In Operando Monitoring of the Pore Dynamics in Ordered Mesoporous Electrode Materials by Small Angle X-ray Scattering, ACS Nano 9 (2015) 5470–5477. Publisher: American Chemical Society.

[90] S. N. Mohd Sobri, S. F. Abdul Sani, S. N. Sabtu, L. M. Looi, S. F. Chiew, D. Pathmanathan, S. Chio-Srichan, D. A. Bradley, Structural Studies of Epithelial Mesenchymal Transition Breast Tissues, Scientific Reports 10 (2020) 1997. Number: 1 Publisher: Nature Publishing Group.

[91] E. Tsolaki, P. Corso, R. Zboray, J. Avaro, C. Appel, M. Liebi, S. Bertazzo, P. P. Heinisch, T. Carrel, D. Obrist, I. K. Herrmann, Multiscale multimodal characterization and simulation of structural alterations in failed bioprosthetic heart valves, Acta Biomaterialia 169 (2023) 138–154.

[92] W. Mathieson, G. Thomas, Using ffpe tissue in genomic analyses: advantages, disadvantages and the role of biospecimen science, Current Pathobiology Reports 7 (2019) 35–40.

[93] F. Coscia, S. Doll, J. M. Bech, L. Schweizer, A. Mund, E. Lengyel, J. Lindebjerg, G. I. Madsen, J. M. Moreira, M. Mann, A streamlined mass spectrometry–based proteomics workflow for large-scale ffpe tissue analysis, The Journal of pathology 251 (2020) 100–112.

[94] A. K. Miller, C. L. Brosnahan, A. Pande, C. F. Baker, J. L. Geoghegan, J. Kitson, N. J. Gemmell, E. J. Dowle, Formalin-fixed paraffin-embedded (ffpe) samples help to investigate transcriptomic responses in wildlife disease, Molecular Ecology Resources (2023).

[95] B. A. Bouwman, N. Crosetto, M. Bienko, The era of 3d and spatial genomics, Trends in Genetics 38 (2022) 1062–1075.

[96] J. Reichmann, S. E. Verleden, M. Kühnel, J. C. Kamp, C. Werlein, L. Neubert, J.-H. Müller, T. Q. Bui, M. Ackermann, D. Jonigk, et al., Human lung virtual histology by multi-scale x-ray phase-contrast computed tomography, Physics in Medicine & Biology 68 (2023) 115014.

[97] A. Maes, C. Pestiaux, A. Marino, T. Balcaen, L. Leyssens, S. Vangrunderbeeck, G. Pyka, W. M. De Borggraeve, L. Bertrand, C. Beauloye, et al., Cryogenic contrast-enhanced microct enables nondestructive 3d quantitative histopathology of soft biological tissues, Nature Communications 13 (2022) 6207.